Master of Science Thesis

Stereoscopic PIV on a delta wing in supersonic flow

An experimental investigation

T. Mathijssen

19 December 2008

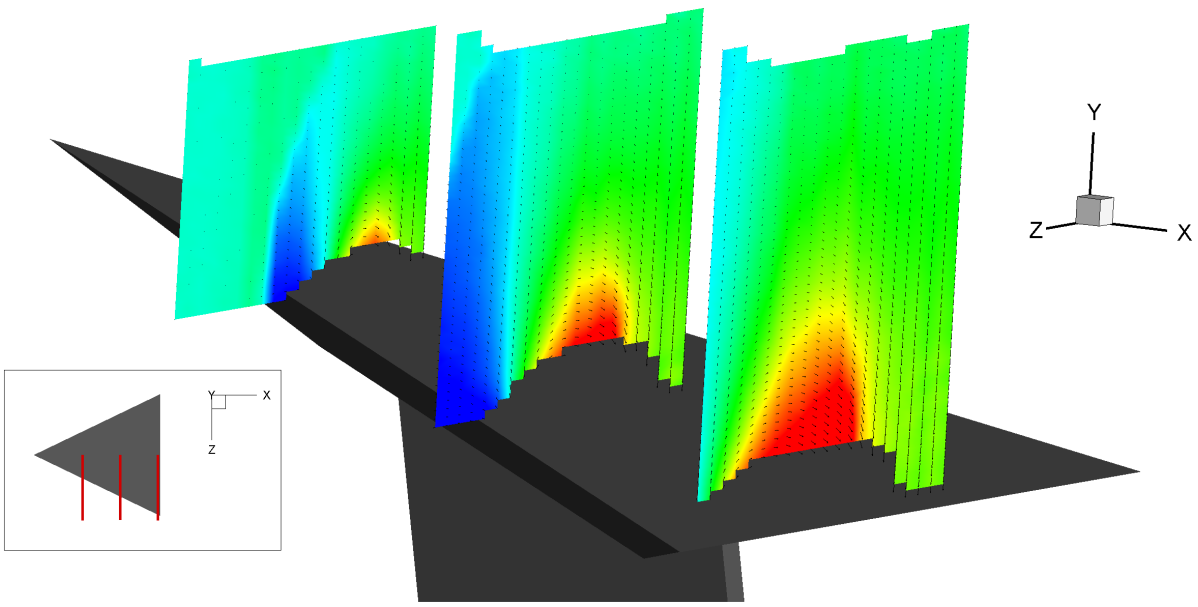

Aerodynamics

Faculty of Aerospace Engineering

TU Delft

Delft University of Technology

Stereoscopic PIV on a delta wing in supersonic flow

An experimental investigation

Master of Science Thesis

For obtaining the degree of Master of Science in Aerospace Engineering
at Delft University of Technology

T. Mathijssen

19 December 2008

Faculty of Aerospace Engineering · Delft University of Technology

Delft University of Technology

DELFT UNIVERSITY OF TECHNOLOGY
DEPARTMENT OF AERODYNAMICS

The undersigned hereby certify that they have read and recommend to the Faculty of Aerospace Engineering for acceptance the thesis entitled **"Stereoscopic PIV on a delta wing in supersonic flow"** by **T. Mathijssen** in fulfillment of the requirements for the degree of **Master of Science**.

Dated: 19 December 2008

Supervisors:

F. Scarano

W.J. Bannink

I. Philipsen

F.F.J. Schrijer

Preface

This report represents the final thesis work performed in the last stages of my study at the faculty of Aerospace Engineering at Delft University of Technology, where I have been working in the field of supersonic experimental aerodynamics. The possibility to perform measurements in the supersonic industrial facility at DNW gave me insight in the world of aerodynamics on an industrial scale, while the application of several measurement techniques showed me the possibilities and limitations in the field of aerodynamic measurements. In every way, my interest in fluid dynamics and admiration for the work from its pioneers has only risen during my thesis.

I would like to thank prof. F. Scarano for the initiation of this project, his guidance and his comments that always turned out to be correct. My gratitude also goes to ir. W. Bannink because his undisputed knowledge on delta wings has provided me insight in the flow around delta wings. Also I would like to thank ir. F.F.J. Schrijer for helping me in the final stages of my graduation and D. Ragni for providing the particle response tests. Furthermore I would like to thank Erik, Frits and Peter for the countless amount of times they operated the wind tunnel and Nico for helping me out with all of my computer problems. Also I would like to thank I. Philipsen, F. Wubben and R. van Schinkel, who made it possible to perform the measurements in DNW. Last but not least I would like to thank all the other students in the basement who were always available for a cup of coffee and sharp discussions on any topic.

Tiemo Mathijssen
Delft, December 2008

Abstract

Ever since the 1950s delta wings are being used as an efficient planform for supersonic flight. Over time extensive research on the aerodynamics of this type of wings has been performed using many different measurement techniques. Due to technical difficulties, measurements on delta wings in a supersonic flow are still scarce and often limited to qualitative data only.

The addition of PIV as a diagnostic tool in aerodynamics opened doors for new measurements. Nowadays PIV is a well-established non-intrusive measurement method that is being applied in large scale subsonic industrial facilities on a regular basis and in research facilities in all flow regimes. Stereoscopic PIV measurements on delta wings are done previously in sub- and transonic flow, and one 2C-PIV experiment has been done on a delta wing in supersonic flow at moderate angle of attack. The motivation of the current investigation is to perform stereo-PIV measurements around a sharp-edged delta wing in a supersonic flow at high angle of attack using the latest advances in PIV. Furthermore an extension is made to a similar setup in the industrial facility of DNW-SST on the EUROSUP model.

The flow around a delta wing is succesfully described at different Mach numbers and for several angles of attack. A spanwise scan using individual measurement planes in streamwise orientation has been made, which are combined to construct a mean flow field in the complete volume. The response of the tracer particles is measured by an oblique shock test, from which the slip velocity with respect to the flow and the drift from the flow path, due to their inertia, is determined. Schlieren, shadowgraphy and oil flow visualisation are applied to give additional information on the flow.

Several flow features have been measured by PIV. As expected a vortex is present on the leeward surface of the wing. Due to the large deflection of the flow on the windward surface, a detached shock is present before the leading edge extending to the expansion side of the wing. Attached to the vortex an inboard shock wave has been measured. Furthermore the flow field appeared to be conical, i.e. the flow variables are constant on rays emerging from the apex.

A similar stereo-PIV setup has been succesfully applied in the industrial supersonic facility SST at DNW using a high-repetition acquisition system including a model sliding mechanism to increase data production. However, due to the large size of the seeding particles in this campaign, the data generated in this tunnel remains questionable, and a thorough investigation on the seeding production is necessary to acquire reliable PIV data in this facility.

Table of Contents

List of Figures

List of Tables

Nomenclature

Latin Symbols

A	aspect ratio
a	attachment line
b	wing span
c	chord
c	speed of light
d	diameter
f	focal length
$f_\#$	f-stop number (D_a/f)
I	light intensity
K	Gladstone-Dale constant ($2 \cdot 10^{-4}$ for air)
Kn	Knudsen number
M	Mach number
M	Magnification factor
n	refractive index
p	pressure
R	specific gas constant
r	radius
Re	Reynolds number
s	separation line
T	temperature
t	time
u,v,w	velocity component in x,y,z direction respectively
V	velocity

Greek Symbols

α	angle of attack
γ	ratio of specific heats
Λ	leading edge sweep angle
λ	wavelength
μ	viscosity

ψ	slope of the conical streamline
ρ	density
τ	relaxation time
τ_w	wall shear stress
θ	wing bevel angle
ξ	relaxation length

Subscripts

0	stagnation
1,2	camera 1,2 respectively
a	aperture
c	conical
diff	diffraction
dw	dewarped
e	effective
f	of the fluid
N	normal to the leading edge
p	of the particle
r	in r-direction
slip	slip
t	tangential
tot	total
x,y,z	in x- y- z-direction
ϕ	in ϕ-direction
θ	in θ-direction
∞	freestream condition

Abbreviations

2C, 3C	2 component, 3 component
2D, 3D	2 dimensional, 3 dimensional
DEHS	Di-ethyl-hexyl-sebacat
DNW	Duits-Nederlandse Wind tunnels
PIV	particle image velocimetry

Vectors

D	dewarping vector
R	disparity vector

Chapter 1

Introduction

1.1 Background

For centuries it has been a dream of humans to be able to fly. Ever since the first powered flight of the Wright brothers in 1903 aviation has come a long way. People were soon able to fly for a longer time than a few seconds and much faster. The military became interested and after the first world war, it was clear that future wars were to be won with a good air force which started rapid development in military aircraft. The velocity of the fighter aircraft began to rise quickly because being able to fly faster has a big advantage on your opponent. The introduction of the jet engine introduced airplanes in the compressibility regime and soon a bounding velocity became apparent: the sound barrier. The dramatic increase in drag around the speed of sound limited the aircraft to subsonic speeds despite the advances that were made in jet power, and a search for new concepts started in order to reduce drag.

Figure 1.1: The XF-92A research aircraft which was one of the first aircraft to incorporate delta wings in its design (©NASA).

A German professor Alexander M. Lippisch foresaw the advantages of the delta wing at high speeds and started research on a delta wing glider. At the end of the second world war his glider was captured by the Americans, but Lippisch continued his research on delta wings for the U.S. Army Air Forces, the predecessor to the U.S. Air Force. Quickly after the war, the delta wing was put in practice in the Convair XF-92A supersonic interceptor which would lead to amongst other the F-102 Delta Dagger, F-106 Delta Dart and B-58 Hustler.

The delta wing has much lower drag at supersonic speeds than a normal planform because of its possibility to have its wing behind the shock cone from the nose, reducing wave drag dramatically. Another advantage is that it is easy to manufacture and can be made strong even at small thickness. The generation of vortices that separate at the leading edge and reattach more inboard of the wing, gives the delta wing a very high stall angle, which is favourable for manoeuvering capabilities and achieving high lift at supersonic speeds. Two of the most famous aircraft designs, the Concorde supersonic transport vehicle and the Space Shuttle, shown in figure 1.2, also make use of a delta wing configuration.

However, the delta wing design also has some important drawbacks. It needs a high start and landing velocity and due to its low aspect ratio is generates a lot of induced drag which is important at low speeds and it is very difficult to keep the aircraft stable at these speeds. The latter almost lead to the abolishment of the delta wing in total, but development of fly-by-wire flight control system technology prevented this. Instead, this aircraft instability together with the addition of canard wings turned the delta wing into an advantageous design increasing manoueverability and it is indicative for its success that latest fighter aircraft designs like the Eurofighter Typhoon still make use of delta wings.

(a) Space Shuttle during landing (©NASA)

(b) Concorde at take off. Notice the condensation in the vortex above the wing. (©The Global Aircraft Organisation)

Figure 1.2: Two of the most famous delta wing designs.

1.2 Motivation

From its introduction up to now, a lot of research has been performed on delta wing aerodynamics using many different measurement techniques. The focus has been mostly on su-

personic flows, but technical problems measuring this flow restricted the research mainly to qualitative techniques such as the vapour screen technique [12] and oil flow visualisation [28]. They gave valuable information, leading to a flow classification depending on the angle of attack and Mach number normal to the leading edge by Miller and Wood [16], but quantitative information came mostly from pressure measurements, e.g. by Bannink [5]. These were then compared with theoretical predictions such as in the paper from Squire [25]. With the rise of computer power, CFD was added to the set of tools to investigate both fundamental delta wings flows [13] and full configurations [17]. Still quantitative experimental data on supersonic delta wings remains scarce, and is non-existing for these flows at high angle of attack.

Since the 1980s PIV emerged as a quantitative measurement tool for fluid flows bringing new opportunities for flow measurements. The introduction of stereoscopic PIV [29] allowed also measurement of the out-of-plane component and even volumes can be measured fully 3-dimensional using Tomographic PIV [8]. Nowadays PIV is a well-established non-intrusive measurement method that is being applied in large scale subsonic industrial facilities on a regular basis and in research facilities in all flow regimes [23]. A feasability study on the application of planar 2C-PIV has also been applied in the supersonic industrial facility of DNW-SST [27].

It has also been used previously for delta wing flows in subsonic conditions by Elsayed [7] using stereo PIV and in transonic conditions by Schröder [24]. The only supersonic delta wing PIV experiment is performed by Lang [11] using planar 2C-PIV at moderate angle of attack. This study corresponds to a different region of the classification of Miller and Wood.

The motivation of the current investigation is to perform stereo-PIV measurements around a sharp-edged delta wing in a supersonic flow at high angle of attack with the latest advances in PIV. Furthermore an extension is made to apply this setup in a supersonic flow in the industrial facility of DNW-SST on the flow around a full model.

1.3 Thesis outline

First some background information is given in chapter 2 about the measurement techniques that have been important in investigation of the flow around delta wings, e.g. Schlieren and vapour screen visualisation. In this chapter also the flow topology is outlined. Then in chapter 3 the PIV measurement technique is explained in detail, starting with the basic principles of planar 2C-PIV, which is the starting point for the explanation of stereoscopic PIV. Chapter 4 deals with the experimental setup. Several different measurement techniques have been used in the current study, Schlieren and oil flow visualisation, shadowgraphy and more extensively PIV. This chapter contains the test matrix, details about the type of equipment and the experimental setup. The results of all measurement techniques are presented in chapter 5, but since PIV is the only quantitative technique this is elaborated in more detail. The data reduction in terms of a conical coordinate transformation is also given in this chapter. Chapter 6 describes the extension of the measurements to the supersonic industrial facility DNW-SST. The measurement equipment, the setup and the results of this campaign are presented in this chapter. Finally the conclusions drawn from the experiments and some recommendations for future investigations are given in chapter 7.

Chapter 2

Delta Wing flow investigation

In this chapter some background information is given on delta wing flows. Delta wings have been studied extensively for a long time. The reason that this type of flow is selected is that it is a well established topic in aerodynamics for which an abundant amount of literature is available. Some of the classical methods that have been important in the research of delta wings are described in section 2.1. Two previous PIV measurements in the compressible flow regime are outlined in section 2.2. The flow characteristics around a delta wing are given in section 2.3.

2.1 Classical measurement methods

Many different measurement techniques have been used to conduct research on delta wings. The most important ones are described in this section. The Schlieren method (section 2.1.1) and shadowgraphy (2.1.2) have in common that they are optical methods. Section 2.1.3 describes the oil flow visualisation technique which is a surface method. The vapour screen method, described in section 2.1.4, has been widely employed in delta wing research. All of these mentioned methods have the drawback that they are qualitative methods. The only quantitative method used historically is the 5-hole probe, described in section 2.1.5, but it has the disadvantage that it is intrusive. This section concludes then with section 2.1.6 on numerical techniques.

2.1.1 Schlieren visualisation

Schlieren visualisation is a non-intrusive visualisation method based on the varying velocity of electromagnetic waves in the optical medium. The speed at which these waves travel are dependent on the density according to the Gladstone-Dale relation:

$$n = \frac{c_0}{c} = 1 + K\rho \tag{2.1}$$

in which n is the refractive index, c is the local light speed, c_0 the light speed in vacuum, K is the Gladstone-Dale constant which is $2 \cdot 10^{-4} m^3/kg$ for air and ρ corresponds to the density of the fluid. This relation states that the refractive index is a function of density. A change

in refractive index causes refraction of the lightwaves according to Snell's law, see figure 2.1 and equation 2.2.

$$n_1 \sin \alpha_1 \quad = \quad n_2 \sin \alpha_2 \tag{2.2}$$

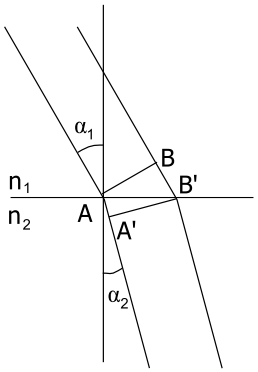

Figure 2.1: Refraction of light due to a difference in refractive index.

The Schlieren visualisation method is based on this concept of refraction. A collimated light beam, created by a light source in the focal point of a lens or parabolic mirror, is sent through the test section of the wind tunnel. The collected light is focused on a Schlieren knife that cuts half of the light intensity in the focal point after which it is imaged on a camera. Rays passing through density gradients are refracted, deviate from their path and either more rays are blocked by the Schlieren knife showing up as darker regions on the image or less rays will

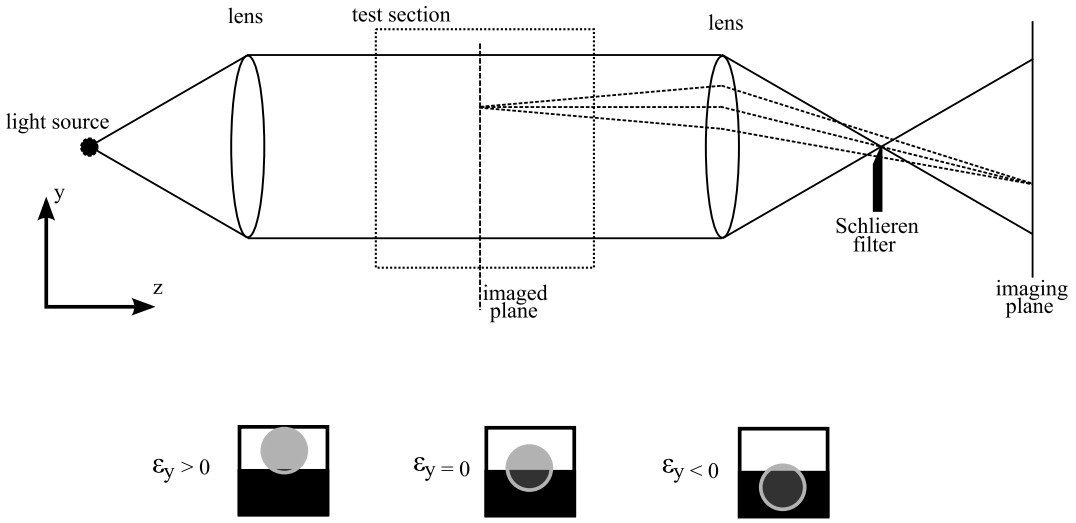

Figure 2.2: A schematic setup for Schlieren visualisation.

be blocked showing up brighter on the image. A schematic drawing of a Schlieren setup is shown in figure 2.2. The system is only capable of measuring light ray deflections normal to the Schlieren knife, making the orientation of the Schlieren knife important for what is visualised. The quantity measured is ∇n which corresponds to the density gradient $\nabla \rho$.

Although Schlieren imaging can be used quantitavely for 2D flows by measuring the light intensity from which the density gradients are retrieved, it is used only as a qualitative measurement technique for 3D flows. The vortex size and location on a delta wing and in supersonic flows shocks can be visualised with the Schlieren method.

Since it is a 2D measurement method, a side-view Schlieren setup is neither capable of measuring density gradients normal to the optical path, nor is it capable of defining the spanwise location of the measured phenomena. The surface reflective visualization technique as used by Donohoe [6] uses light rays normal to the surface of the wing, which is reflective, allowing visualisation of spanwise phenomena.

2.1.2 Shadowgraphy

Shadowgraphy is an optical method similar to Schlieren visualisation making use of the same principle of refraction of light due to density gradients. After passing the test section where the rays are deflected, the light is directly imaged on the imaging plane, instead of focusing them on a Schlieren knife, see figure 2.3. This has as an effect that the model itself is out of focus. Light rays passing a density gradient are deflected and are imaged on a different position on the imaging plane, disturbing the uniform light distribution, showing up as a dark region followed by a light region. Because the light is imaged directly on the imaging plane, the position of this plane influences the imaging position of the deflected light rays in the shadowgraph.

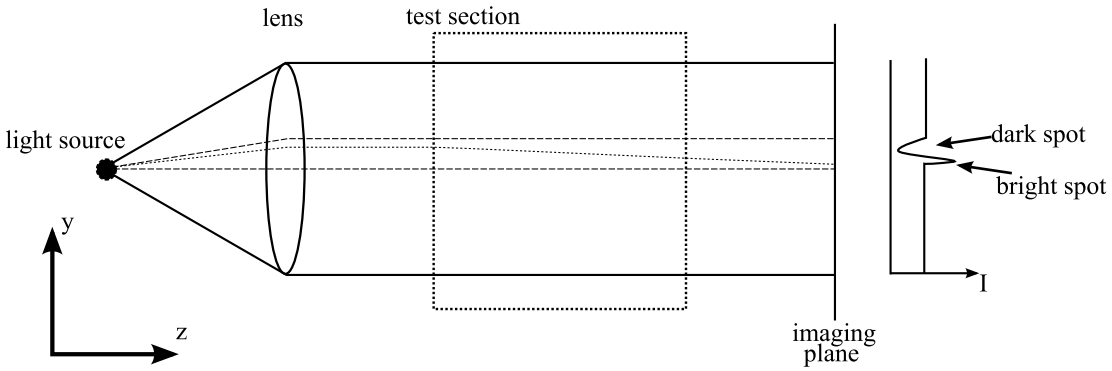

Figure 2.3: A schematic setup for Shadowgraphy.

Shadowgraphy measures $\nabla^2 n$ along the optical path, instead of ∇n which is measured with Schlieren visualisation. To quantify the density from the Shadowgraph in 2D flows, the result needs to be integrated twice, making measuring quantitatively very difficult. This is

impossible for 3D flows since it measures the integral over the optical path. Therefore it is used as qualitative method. However in general flow structures, e.g. boundary layers and shear lines are better visualised with Shadowgraphy than using Schlieren.

2.1.3 Oil flow visualisation

When the oil flow visualisation technique is used, a thin layer of oil is applied to the surface of the model having a contrasting colour. When the windtunnel is started the oil starts flowing as a result of the wall shear stress in the boundary layer and the local pressure gradient. Since the streak pattern takes some time to form, it is classified as a time-averaged method. At some time instant the oil will stop flowing because the solvent has evaporated, fixing the streaks to the surface. In general the oil pattern follows the wall shear stress which is related to the velocity gradient close to the wall by

$$\tau_w = \mu \frac{\partial u}{\partial y} \tag{2.3}$$

In some areas the oil streaks can deviate from the flow direction because the local shear stress is small and the pressure gradient is high, e.g. in separation areas. In delta wing flows the oil flow visualisation technique is very useful to find the position of flow separation lines, indicated by an accumulation of oil, and reattachment lines, indicated by a deviation from the linear path which is present at the root chord.

2.1.4 Vapour screen visualisation

The vapour screen visualisation method is a method first employed by Allen and Perkins in 1951 and has been used extensively to visualise vortices above delta wings. McGregor studied the technique in more detail [12]. The principle of the vapour screen method based on condensation of moist air. The air expands through the wind tunnel laval nozzle supersaturating the air, which consequently condensates the water into a uniform fog of tiny droplets or ice crystals of about $0.7\mu m$ in diameter. This is then illuminated by a narrow light beam, making the fog particles scatter light. The amount of light scattered depends on the amount of fog particles present. When a disturbance is present such as the delta wing, this disturbs the uniform distribution of the fog. In vortices, the fog droplets are ejected out of the core under the centrifugal forces because of their inertia, making the vortex appear darker on the images as can be seen in figure 2.4. Furthermore, the amount of particles also scale with the density of the fluid.

This method can only be used qualitatively. Furthermore, the condensation of water may have an influence on the flow conditions. Condensation is an exotherm process, increasing the total temperature of the surrounding air. Consequently the Mach number decreases and the static pressure increases. Although impossible to remove this effect entirely, it is possible to reduce this effect by using a different substance than water with a lower latent heat of evaporation, e.g. carbon tetrachloride. Another drawback of this method is that it can only be used in high velocity flows, as enough vapour and high enough particle slip has to be present. Despite its drawbacks this method has contributed significantly in the research on delta wing flows and has produced a lot of valuable qualitative information on the flows around delta wings.

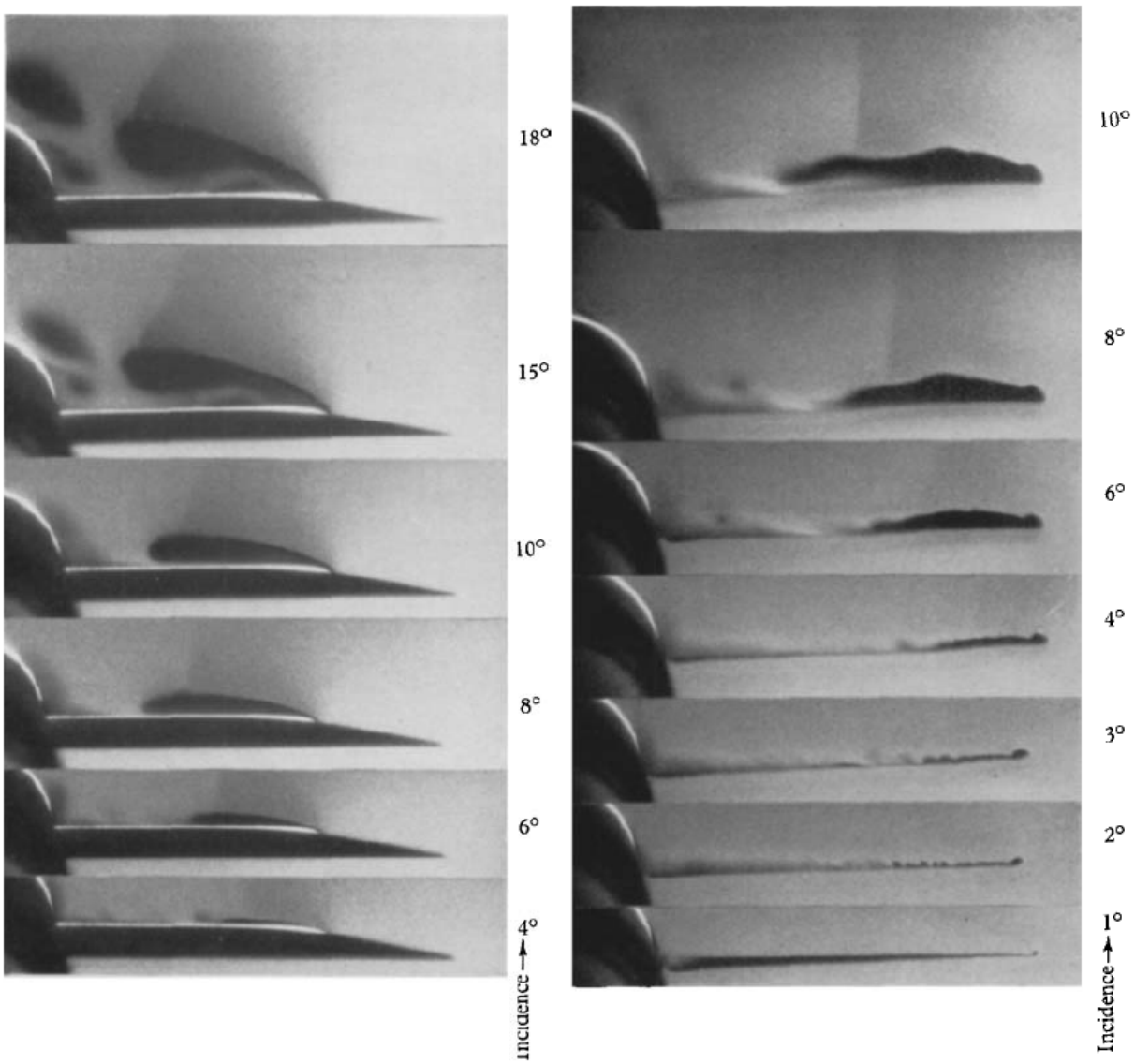

(a) Vapour screen photograph of the flow over the upper surface at $M = 1.75$ ($M_{dry} = 1.81$)

(b) Vapour screen photograph of the flow just behind the model at $M = 1.88$ ($M_{dry} = 2.00$)

Figure 2.4: Two examples of vapour screen photographs of a combination of a flat delta wing and a cylindrical fuselage at different angles of attack (from McGregor [12])

2.1.5 5-hole probe pressure measurements

One of the few quantitative measurement techniques that historically have been applied to delta wings are pressure measurements. Surface pressure measurements are easy to perform, however flowfield measurements around the wing require a 5-hole probe. This is a spherically shaped pitot tube with multiple holes in order to simultaneously measure the pressure at different locations on the probe, allowing measurement of the flow velocity and flow direction.

The 5-hole pressure probe requires a thorough calibration procedure by performing measurements in an uniform flow. Calibration functions relating the pressures from the individual holes to the roll angle Φ and pitch angle Θ as defined in figure 2.6, are calculated.

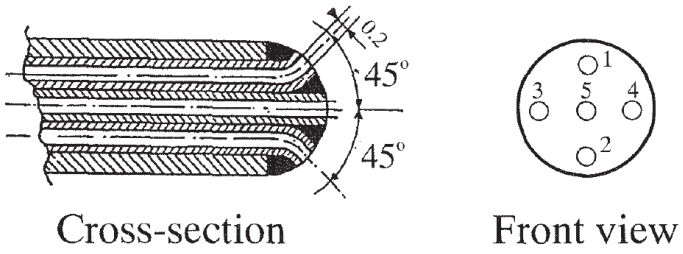

Figure 2.5: Example of the layout of a 5-hole pressure probe (from Donohoe [6])

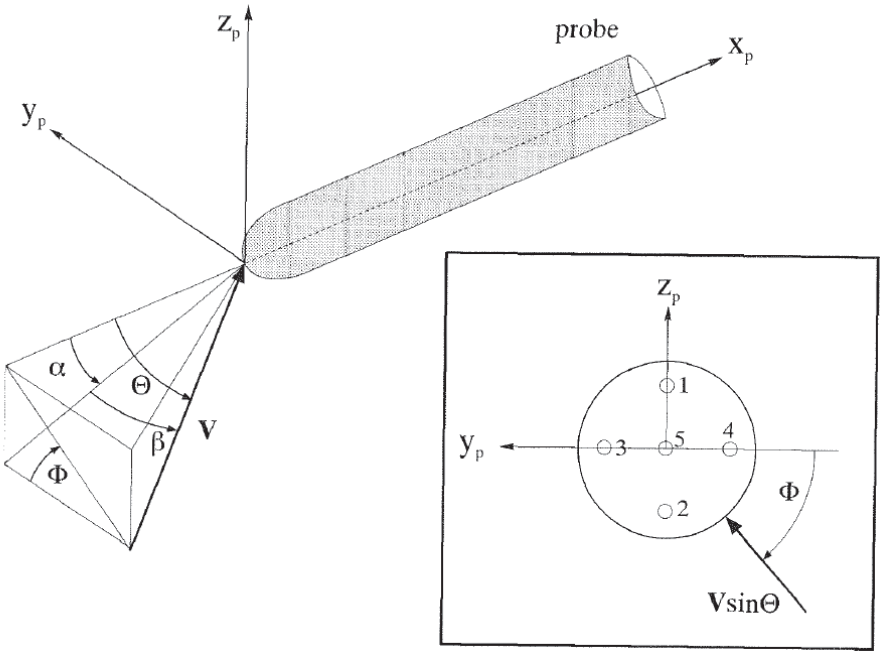

Figure 2.6: Definition of the angles of the pressure probe (from Donohoe [6]).

One of the drawbacks is that it is a point measurement device, therefore investigation of a complete volume requires many measurements. Fortunately the measurement time per datapoint can be rather small and the process can be automated, reducing wind tunnel time. E.g. Bannink [5] states that it is possible to acquire 45 data points in one wind tunnel run of $35s$.

Another drawback is the finite distance between the pressure holes, in areas with large pressure gradients, e.g. shocks, the measured flow angle is incorrect. Perhaps the most important

drawback of the 5-hole pressure probe is that it is an intrusive device. It physically has to be put into the flow, including a support, resulting in a blockage effect and a local disturbance of the flow. Especially when measuring close to the model, this can have a large effect. Donohoe [6] notes that the probe starts to shake significantly during measurements close to the wing surface and that the location of the vortex that is being measured is being obscured because of the presence of the pressure probe. It can influence the vortex core location and its stability.

The reason the 5-hole pressure probe has been so succesful in delta wing research is that it is able to measure in both low speed and in high speed (supersonic) regime and that it has been one of the few quantitative measurement techniques.

2.1.6 Numerical techniques

With the steady advance in computer power and numerical techniques, CFD has become increasingly important in delta wing research, e.g. the study of McMillin [13]. Often it has gone hand in hand with experiments, serving as a validation testcase for the numerical codes and turbulence models. Good examples are the international Vortex Flow Experiments in which a series of measurements on delta wing flows have been performed [17, 24]. These measurements were done in combination with different numerical codes and turbulence models. Apart from validating the codes also new information on delta wings became available.

The major advantage of numerical methods is that it is easy to obtain velocity and pressure results in the full domain. However, numerical diffusion has a large influence on the vortex decay and stability, posing problems for resolving delicate flow features, e.g. vortex burst.

2.2 Previous PIV experiments

Also PIV is not new in the study on delta wing flows. In the year 2000 Lang performed 2C-PIV measurements on the hypersonic transport vehicle ELAC at $M_\infty = 2.0$ [11]. The model has a sweep angle of 75° and round leading edges. Since the flow field is 3-dimensional, several planes were measured perpendicular to each other, see figure 2.7. A single frame, double exposure technique was used on photographic film to account for the small time difference between exposures. The images were analysed using the Young's fringes method [20]. Also a shocktest is performed as described by Schrijer [22] and corresponding particle drift is calculated, resulting in a estimated particle size of 1.95 μm, see figure 2.8. However, with the sweep angle of 75° and a Mach number of $M_\infty = 2.0$ and $\alpha = 10°$, the corresponding normal Mach number and angle of attack are $M_N = 0.62$ and $\alpha_N = 34°$, which corresponds to region 1 of the diagram of Miller and Wood [16], see section 2.3.

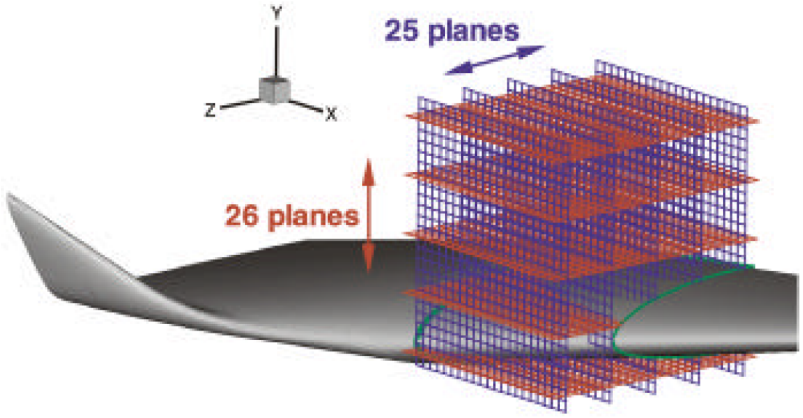

Figure 2.7: Orientation of the different planes of measurement over the leeside of the ELAC configuration (from Lang [11]).

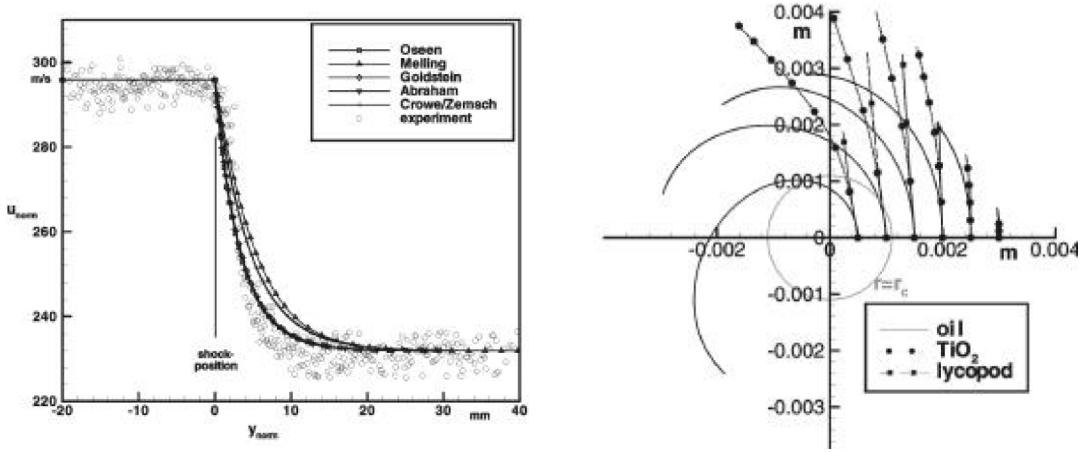

(a) velocity profile after an oblique shock (from Lang [11]).

(b) path of particles in a compressible wing vortex (from Lang [11]).

Figure 2.8: Particle response assesment from Lang [11].

A more recent PIV experiment has been performed by Schröder [24], in which stereoscopic PIV measurements are made around a delta wing with a 65° sweep angle in the transonic region as part of the International Vortex Flow Experiment 2 (VFE-2), see figure 2.9. In this study a double frame, single exposure technique is applied, which removes the amiguity in velocity direction and simplifies image evaluation significantly. The images are evaluated digitally by statistical cross-correlation. However, with a normal Mach number of $M_N = 0.46$ and maximum angle of attack $\alpha_N = 48.4°$ all flow cases are still limited to region 1 in the diagram of Miller and Wood [16]. Two different models are used: one with sharp edges and one with round leading edges, but both show some curvature at the leading edge.

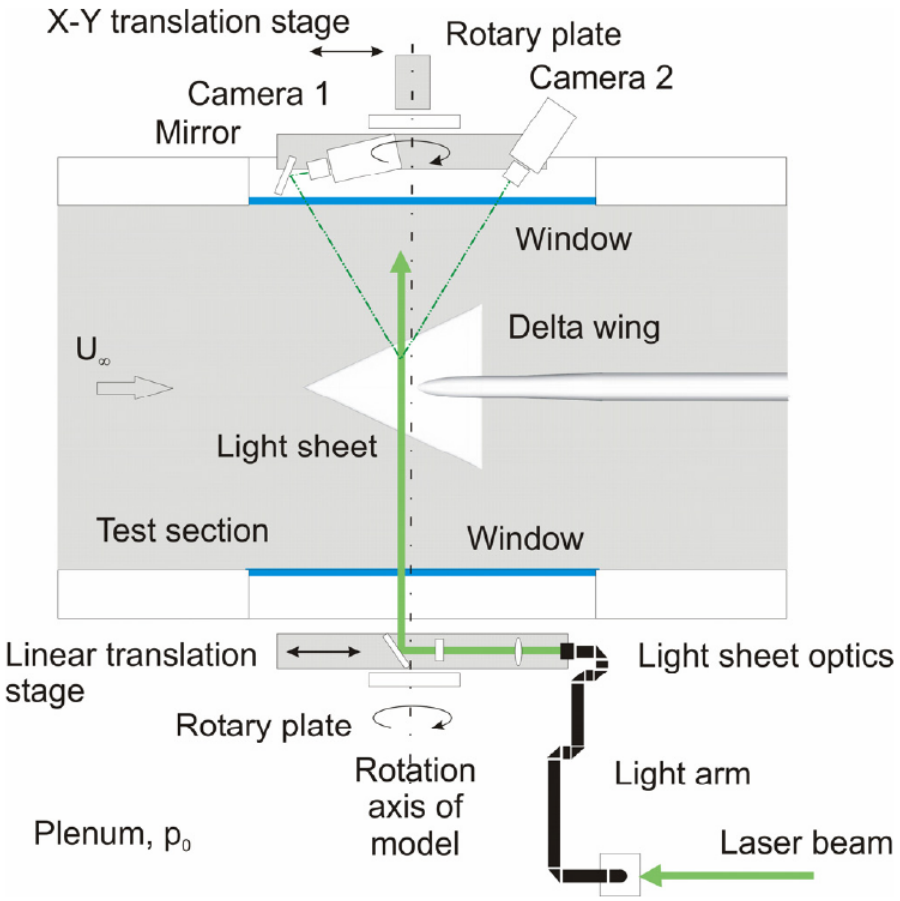

Figure 2.9: Stereoscopic PIV arrangement from Schröder [24].

2.3 Delta wing flow characteristics

The flow over the leeward surface of a delta wing at incidence is characterised by a pair of vortices in which the flow separates from the leading edge and reattaches inboard on the wing. Each vortex emerges from the apex and continues its way downstream. The vortex core follows a path with a certain sideslip angle and incidence angle with respect to the delta wing centerline. The primary vortex can induce a smaller secondary vortex resulting in a flow as depicted in figure 2.10. Even a tertiary vortex may occur.

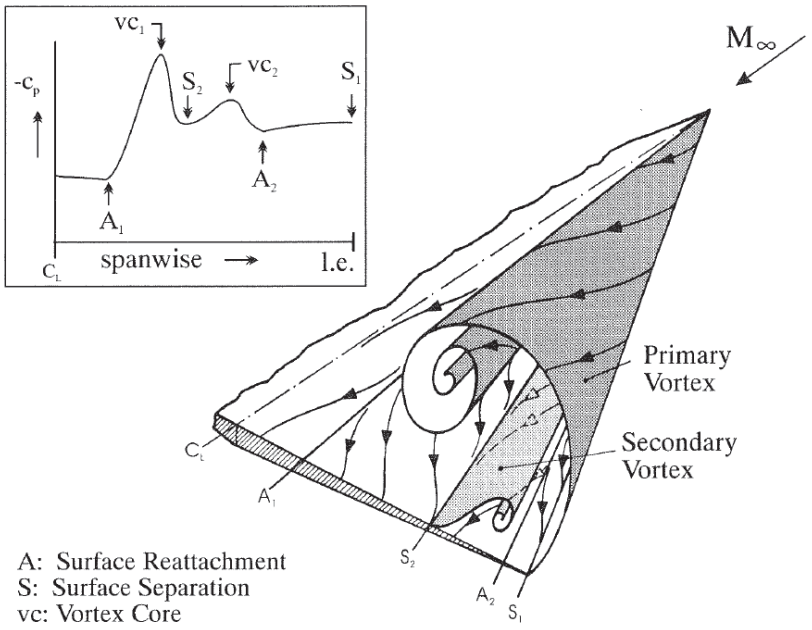

Figure 2.10: Characteristic flow over the leeward surface of a sharp leading edge delta wing with its surface pressure distribution (from Donohoe [6]).

At higher Mach numbers the possible occurrence of shocks make the flow more complicated. The type of flow that occurs depends on the normal angle of attack α_N and normal Mach number M_N, defined as

$$M_N = M_\infty \cdot \sqrt{1 - \sin^2 \Lambda \cos^2 \alpha} \tag{2.4}$$

$$\alpha_N = \tan^{-1}\left(\frac{\tan \alpha}{\cos \Lambda}\right) \tag{2.5}$$

in which Λ is the leading edge sweep angle, which is the angle between the leading edge and the plane normal to the flow direction at zero incidence, shown in figure 2.11. This led to the classification of Miller and Wood [16] depicted in figure 2.12, which distincts several regions of flow depending on the particular flow mechanisms present; e.g. the occurrence of shocks, whether they are attached or not, etc.

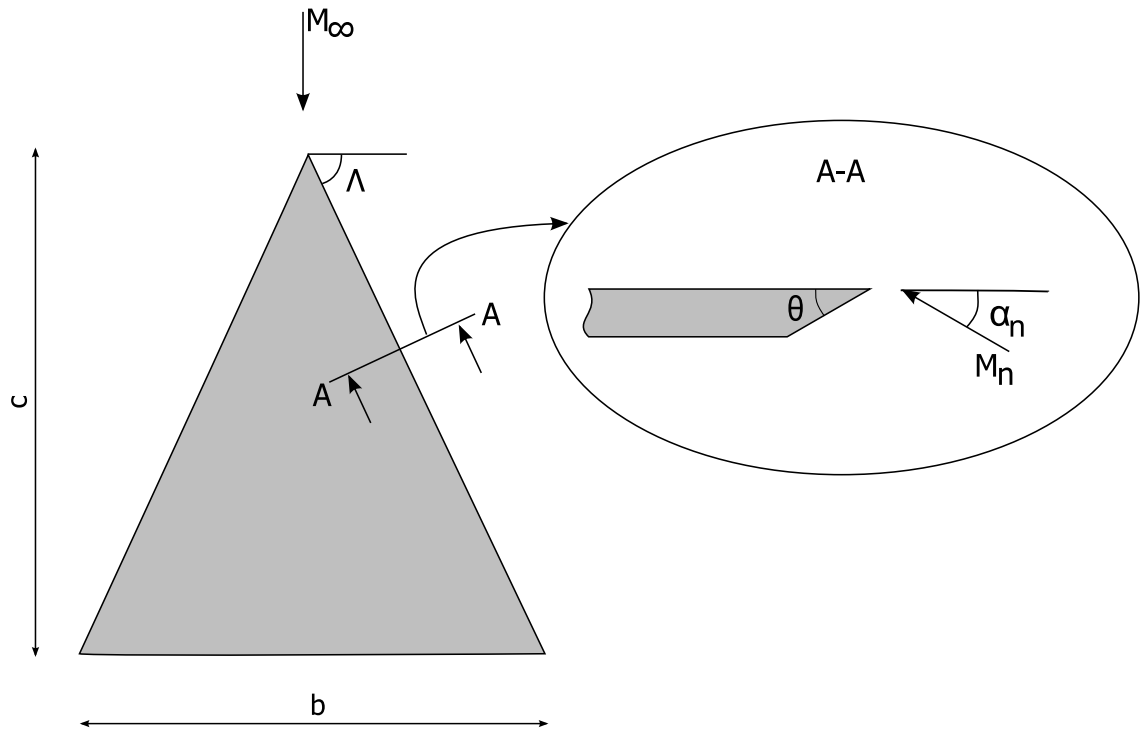

Figure 2.11: General layout of a deltawing

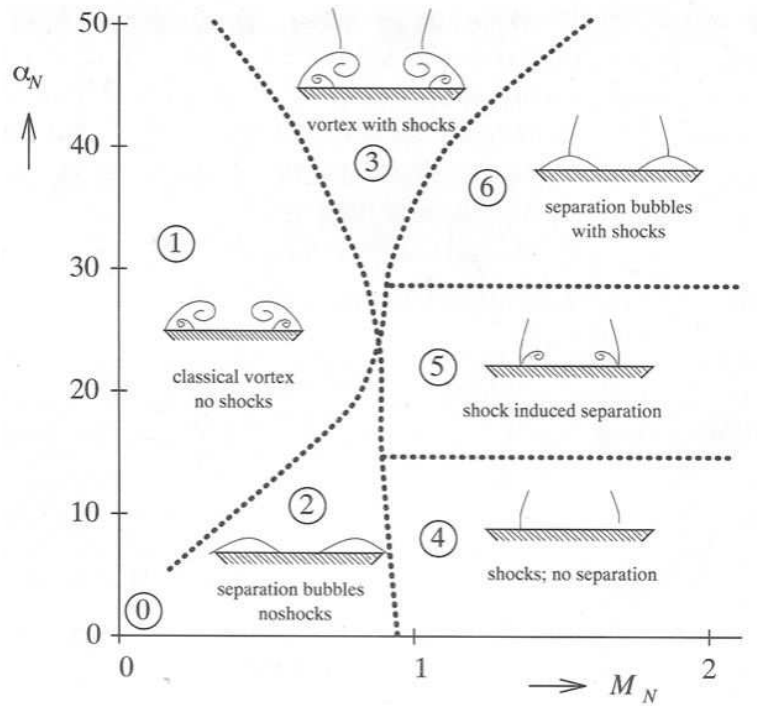

Figure 2.12: Classification of delta wing flows according to Miller and Wood [16].

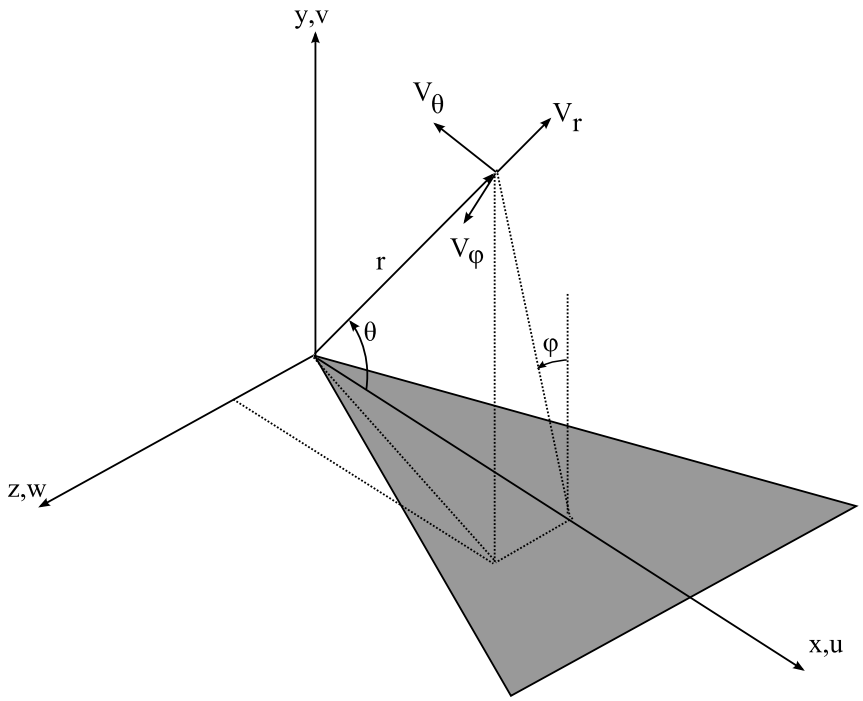

Figure 2.13: Definition of the conical coordinates

The flow is conical, meaning the flow variables are constant on rays emerging from the apex. This means the flow is quasi-2-dimensional, depending only on angles ϕ and θ as defined in figure 2.13. Transformation of the Euler flow equations into conical coordinates [4] results in

$$\frac{\partial \rho}{\partial r} = -\frac{1}{V_r}\left[\rho\frac{\partial V_r}{\partial r} + \frac{2\rho V_r}{r} + \frac{1}{r\sin\theta}\frac{\partial}{\partial\phi}\left(\rho V_\theta \sin\theta\right) + \frac{1}{r\sin\theta}\frac{\partial\left(\rho V_\phi\right)}{\partial\phi}\right] \tag{2.6}$$

$$\frac{\partial V_r}{\partial r} = -\frac{1}{V_r}\left[\frac{V_\theta}{r}\frac{\partial V_r}{\partial\theta} + \frac{V_\phi}{r\sin\theta}\frac{\partial V_r}{\partial\phi} - \frac{V_\theta^2 + V_\phi^2}{r} + \frac{1}{\rho}\frac{\partial p}{\partial r}\right] \tag{2.7}$$

$$\frac{\partial V_\theta}{\partial r} = -\frac{1}{V_r}\left[\frac{V_\theta}{r}\frac{\partial V_\theta}{\partial\theta} + \frac{V_\phi}{r\sin\theta}\frac{\partial V_\theta}{\partial\phi} + \frac{V_r V_\theta}{r} - \frac{V_\phi^2\cot\theta}{r} + \frac{1}{r\rho}\frac{\partial p}{\partial\theta}\right] \tag{2.8}$$

$$\frac{\partial V_\phi}{\partial r} = -\frac{1}{V_r}\left[\frac{V_\theta}{r}\frac{\partial V_\phi}{\partial\theta} + \frac{V_\phi}{r\sin\theta}\frac{\partial V_\phi}{\partial\phi} + \frac{V_r V_\phi}{r} - \frac{V_\theta V_\phi\cot\theta}{r} + \frac{1}{r\rho\sin\theta}\frac{\partial p}{\partial\phi}\right] \tag{2.9}$$

$$h_0 = h_\infty + \frac{V_\infty^2}{2} = h + \frac{1}{2}\left(V_r^2 + V_\theta^2 + V_\phi^2\right) \tag{2.10}$$

All derivatives with respect to r can be eliminated since the flow is independent of r. This

results in a simplified version of these equations.

$$0 = 2\rho V_r \sin\theta + \frac{\partial}{\partial\phi}\left(\rho V_\theta \sin\theta\right) + \frac{\partial\left(\rho V_\phi\right)}{\partial\phi} \tag{2.11}$$

$$0 = V_\theta \frac{\partial V_r}{\partial\theta} + \frac{V_\phi}{\sin\theta}\frac{\partial V_r}{\partial\phi} - V_\theta^2 + V_\phi^2 \tag{2.12}$$

$$0 = V_\theta \frac{\partial V_\theta}{\partial\theta} + \frac{V_\phi}{\sin\theta}\frac{\partial V_\theta}{\partial\phi} + V_r V_\theta - V_\phi^2 \cot\theta + \frac{1}{\rho}\frac{\partial p}{\partial\theta} \tag{2.13}$$

$$0 = V_\theta \frac{\partial V_\phi}{\partial\theta} + \frac{V_\phi}{\sin\theta}\frac{\partial V_\phi}{\partial\phi} + V_r V_\phi - V_\theta V_\phi \cot\theta + \frac{1}{\rho\sin\theta}\frac{\partial p}{\partial\phi} \tag{2.14}$$

$$h_0 = h_\infty + \frac{V_\infty^2}{2} = h + \frac{1}{2}\left(V_r^2 + V_\theta^2 + V_\phi^2\right) \tag{2.15}$$

The character of these equations is determined by the conical Mach number, which is determined by

$$V_{tot} = \sqrt{V_c^2 + V_r^2} \tag{2.16}$$

$$M_c = \frac{\sqrt{V_{tot}^2 - V_r^2}}{a} \tag{2.17}$$

The normal Mach number M_N is the conical Mach number M_c at the leading edge of the wing. Shocks can occur when the local conical Mach number is higher than one, on the right hand side of the vertical line near $M_N = 1$ bending towards the y-axis with increasing α_N in the diagram of Miller and Wood. This is closely related to the Stanbrook-Squire boundary [26], which distincts between flow attached to the surface and separated flow at the leading edge. This is in principle the same line but bends away from the y-axis with increasing α_N. In supersonic flows the bevel angle θ, shown in figure 2.11, is important because the flow has to be deflected over an angle of $\theta + \alpha_N$, which can result in detached shockwaves generating a lot of drag.

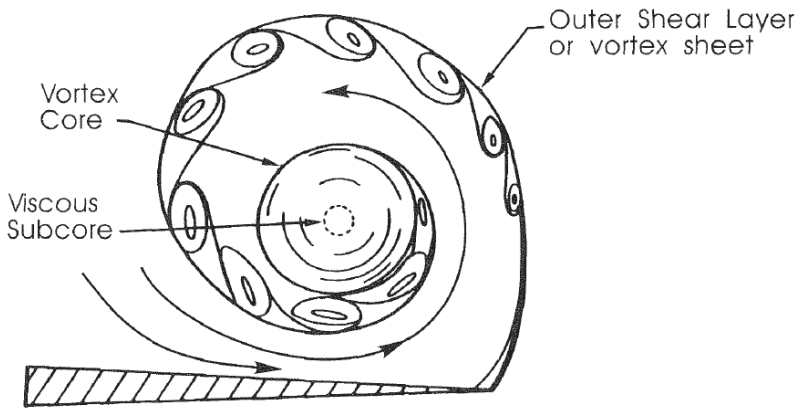

Figure 2.14: The subdivision of a vortex into the free shear layer, the vortex core and the vortex subcore (from Donohoe [6])

.

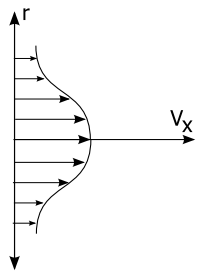

Figure 2.15: The jet-like axial velocity profile.

The primary leading edge vortex is constructed as follows: the flow separates from the leading edge forming a free shear layer. The air wraps up in a vortex core where internally viscosity starts to play an important role, defined as the viscous subcore, see figure 2.14. The vortex shows a jet-like axial velocity profile about the vortex axis like in figure 2.15.

At high normal angles of attack the vortex can lose its stability and vortex breakdown or vortex burst can occur. This results in a sudden decrease in lift together with a strong nose-up pitching moment, making it a very dangerous phenomenon, especially because these flow conditions occur at take-off and landing conditions when high lift-coefficients are necessary.

Vortex breakdown is decribed by Lambourne and Bryer [10] as "a structural change from a strong regular spiral motion to a weaker turbulent motion", see figure 2.16. It is influenced by many factors as angle of attack, Mach and Reynolds number, sweep angle, amount of swirl in the flow etc. In general vortex burst is characterised by a sudden reversal of the spiraling flow of the vortex. Nowadays a lot of research is still devoted to vortex breakdown, since there is still no fundamental understanding of this complex phenomenon.

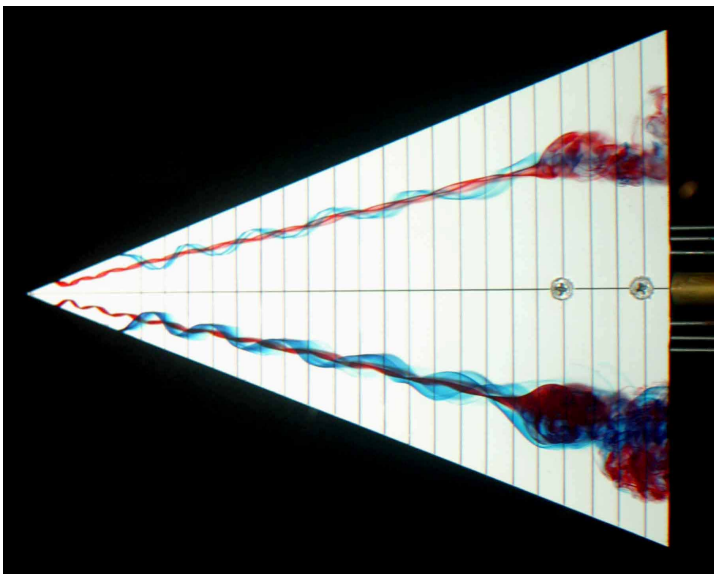

Figure 2.16: Oil streak visualisation of vortex breakdown over a delta wing (©T.T. Lim, University of Melbourne) .

Chapter 3

Particle Image Velocimetry

In this chapter the fundamentals of Particle Image Velocimetry are described. First the 2-component PIV (2C-PIV) method is described, how it works (section 3.1), the selection of the tracer particles (section 3.2), the requirements on the type of illumination and on the recording media (section 3.3) and finally the analysis of the images (section 3.4). The stereoscopic configuration is explained in section 3.5, which in turn is divided into several subsections. One on the reconstruction method, one on the Scheimpflug condition, and one on the mapping procedure before moving to the calibration and self-calibration procedure.

3.1 Introduction

Ludwig Prandtl visualised flows by suspending mica particles on the surface of water allowing him to study flows around two dimensional models like cylinders and airfoils. This principle of bringing tracer particles in the flow is also used in PIV.

While Prandtl was only able to study the behaviour qualitatively, nowadays PIV allows to study fluid flows quantitatively. This is done by illuminating the tracer particles in a planar light sheet, usually by a laser. The particles scatter light in all directions, which is captured by a lens onto a CCD-chip of a camera at two or more time instances. By determining the distance the particles have travelled within the known time-difference, the velocity can be determined. To do this, every image is divided into several interrogation windows in which the statistical cross-correlation technique is applied to obtain the distance travelled by the particle in each of these interrogation window. How this is done is explained in section 3.4. Knowing the fixed time difference between the images, the velocity can be calculated, assuming this is constant in an interrogation window. With the 2C-PIV method the projection of the vector of the local flow velocity into the plane of the light sheet is calculated, which means only two components of the velocity vector are measured. To be able to determine all three velocity components, stereoscopic PIV has to be used, which is described in section 3.5. Some important aspects of PIV are

- **a non-intrusive velocity measurement technique.** Contrary to traditional techniques like the 5-hole pressure probe measurements, no probe has to be put into the flow that disturbs the flow. Only particles are inserted in the flow, but this intrusiveness is much smaller than that of a probe.

- **an indirect measurement.** Not the flow itself is measured, but the velocity of the tracer particles is measured. This means that the particles should follow the flow, otherwise an incorrect velocity is measured. Therefore the seeding material should be selected carefully. Shocks and vortices are regions with high accelerations posing challenges for flow tracking capabilities of the particles.

- **a wholefield technique.** Unlike measurement methods as hotwire anemometry, laser doppler velocimetry and pressure probe measurements, which are point techniques, PIV measures an entire plane, meaning a high spatial resolution. Temporal resolution on the other hand is rather low compared to other techniques, although recent developments in laser and camera technology rapidly increase the temporal resolution.

3.2 Seeding

The type of seeding material needs to be selected carefully, because the velocity of the tracer particles is measured instead of the velocity of the flow itself. This means that the tracer particles should follow the flow as good as possible in order to minimize this error. Another selection criterion is that particles should scatter enough light to be recorded clearly. This conflicts with the first requirement because for flow tracking capability the particles should be small, while for light scattering purposes the particles should be large and a compromise has to be made.

3.2.1 Mechanical properties

According to Melling [15] the motion of a particle is determined by

$$\begin{aligned}\frac{\pi d_p^3}{6}\rho_p\frac{d\bar{U}_p}{dt} = -3\pi\mu d_p\bar{V} + \frac{\pi d_p^3}{6}\rho_f\frac{d\bar{U}_f}{dt} - \frac{1}{2}\frac{\pi d_p^3}{6}\rho_f\frac{d\bar{V}}{dt} \\ -\frac{3}{2}d_p^2\left(\pi\mu\rho_f\right)^{1/2}\int_{t_0}^{t}\frac{d\bar{V}}{d\xi}\frac{d\xi}{(t-\xi)^{1/2}}\end{aligned} \tag{3.1}$$

in which $\bar{V} = \bar{U}_p - \bar{U}_f$ and subscripts p and f indicate the particle and fluid respectively. In the first two terms the acceleration force and the viscous resistance are given. The pressure gradient due to the acccelaration of the fluid close to the particle induces the third term in the equation. The resistance of an inviscid fluid to the acceleration of the particle is given by the potential theory in the fourth term. The final term is called the 'Basset history integral' which is the resistance due to the unsteadiness in the flow field.

Assuming

- the particle is spherical
- the diameter is much smaller than the turbulence length scale of interest
- low particle concentration
- the particle density is much higher than the surrounding fluid density
- forces like buoyancy, added mass and Basset history integral are negligible

equation 3.1 reduces to:

$$\frac{d\bar{U}_p}{dt} = \frac{\left(\bar{U}_f - \bar{U}_p\right)}{\tau_p} \tag{3.2}$$

in which τ_p is the particle relaxation time. For low Reynolds numbers, Stokes' drag can be applied, which results in the following solution of the differential equation for τ_p:

$$\tau_p = \frac{\rho_p d_p^2}{18\mu} \tag{3.3}$$

At higher Reynolds numbers, this is not valid anymore. For a higher velocity but relatively low Mach number and Reynolds number, the drag relation from Melling [14] applies, which is

$$\tau_p = \frac{\rho_p d_p^2}{18\mu}\left(1 + 2.7Kn_d\right) \tag{3.4}$$

where Kn_d is the Knudsen number based on the particle diameter d_p and the relative motion of the particle with respect to the flow. It is defined as $Kn_d = 1.26\sqrt{\gamma}\,(M_{\Delta V}/Re_d)$ with γ the specific heat ratio. Re_d is the Reynolds number based on the diameter of the particle and $M_{\Delta V}$ is the Mach number evaluated for the maximum particle slip velocity V.

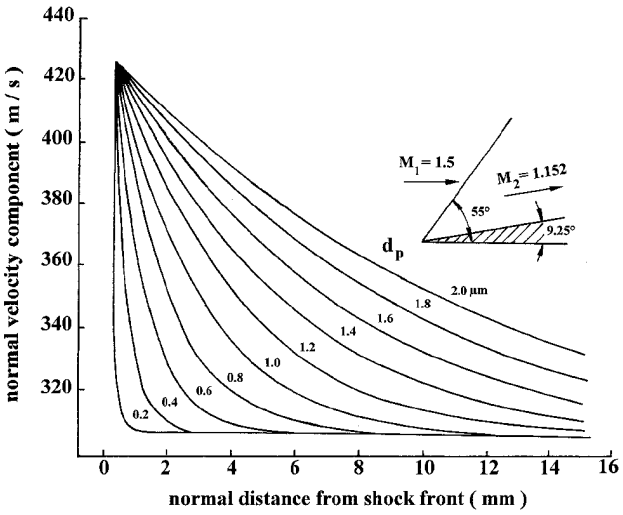

Figure 3.1: Particle response to a step input for different particle size (from Melling [15]).

The particle relaxation time is a measure to what extent the particles follow the flow and this can be determined experimentally by investigating the particle response from a step input. This is done with shock test in a supersonic flow [22]. The particles respond by an exponential deceleration as in figure 3.1 depending on its relaxation time according to

$$u^* = \frac{u_p - u_2}{u_1 - u_2} = e^{\left(\frac{-t_p}{\tau}\right)} = e^{\left(\frac{x_p}{\xi_p}\right)} \tag{3.5}$$

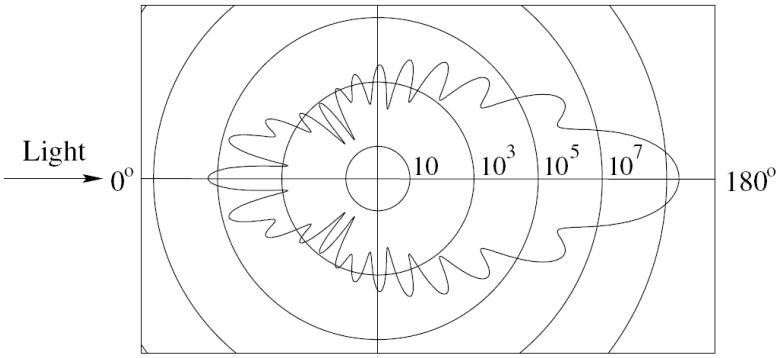

Figure 3.2: Light scattering by a 1 μm oil particle in air (from Raffel [20]).

in which u_p is the velocity of the particle, u_2 is the velocity after the shock and u_1 is the freestream velocity before the shock. t_p and x_p are the time after passing the shock and the distance from the shock respectively. ξ_p is the particle response length and is defined as

$$\xi_p = \tau_p \left(u_1 - \frac{u_1 - u_2}{e} \right) \tag{3.6}$$

Using equation 3.5, the particle relaxation length can be determined directly. With PIV the velocity of the particle is measured after the shock of known strength. This velocity is plotted on a semi-logarithmic scale and its slope is determined. This slope is defined as

$$\frac{\partial (\ln u^*)}{\partial x} = \frac{-1}{\xi_p} \tag{3.7}$$

With this information the particle relaxation length is determined and thus the particle relaxation time. The determination of the particle relaxation time is given in section 5.3.

3.2.2 Light scattering behaviour

The light scattering behaviour of the tracer particles depends on the following parameters [20]

- ratio of the refractive index of the particles and that of the surrounding medium
- particle geometry (size, shape and orientation)
- polarisation of the light
- observation angle

The refractive index is a material property of the particles. But the selection of the material is also determined by other criteria, e.g. the possibility to create the desired size and the toxicity of the material.

For spherical particles with a diameter d_p larger than the wavelength of the light λ, Mie's scattering theory is applied. The light scattering behaviour of a 1 μm oil particle in air

illuminated with laser light with a wavelength of 532 nm is displayed in figure 3.2. From this figure can be concluded that it is advantageous to record in forward scatter mode, since about 10^5 times more light is scattered in this direction. Because of perspective errors in planar 2C-PIV, this is only applicable for stereoscopic arrangements. Optical access does not always allow this and sufficient angular displacement between the cameras is necessary for a reliable measurement of the out of plane component [19].

3.3 Illumination & Imaging

3.3.1 Illumination

To illuminate the particles usually a pulsed laser is used. This is done because lasers have the ability to emit monochromatic light at high energy levels in the order of several hundreds of mJ and it is easy to bundle it into a thin light sheet. Moreover laser pulses have a very short time duration of only a few nanoseconds, necessary to freeze the particles on the images, making them appear as dots instead of streaks.

3.3.2 Small particle imaging

To succesfully record the tracer particles some imaging parameters have to be determined first. The magnification factor determined by dividing the size of the sensor by the field of view.

$$M = \frac{d_i}{d_0} = \frac{L_{sensor}}{L_{FOV}} \tag{3.8}$$

Now a combination of observation distance and focal objective can be selected according to the focus criterion. This yields

$$\frac{1}{f} = \frac{1}{d_0} + \frac{1}{d_i} \tag{3.9}$$

In order to get a good sub-pixel interpolation of the correlation peak, the illuminated area due to the particle should be cover approximately 2 pixels on the sensor, see section 3.4. The effective imaged particle size can be estimated by the following function:

$$d_e = \sqrt{(d_p M)^2 + (d_{diff})^2} \tag{3.10}$$

The first term is from imaging the particle itself, the second term is from the diffraction spot of the particle. The diffraction limited image diameter is usually the dominant term for seeding particles and it is given by

$$d_{diff} = 2.44 f_{\#} (M + 1) \lambda \tag{3.11}$$

In which $f_{\#}$ is the f-stop number, defined as the ratio of the focal length of the lens f and the aperture diameter D_a, and λ is the wavelength of the laser light.

Another requirement is that the measurement plane should be in focus, thus the depth of field δ_Z should at least be the thickness of the laser sheet. This can be estimated in the following manner:

$$\delta_Z = 2 f_{\#} d_{diff} \frac{M+1}{M^2} \tag{3.12}$$

Changing the f-stop number has an effect on three different parameters. E.g. if this is decreased, the amount of light captured by the lens is increased, but the depth of field decreases and the imaged particle diameter decreases increasing the risk of peak-locking.

3.4 Image analysis

To analyse the PIV images, the images are divided into small regions called interrogation windows. Let the light intensity distribution at time t_0 and $t_0 + \Delta t$ be $I_1(x, y)$ and $I_2(x, y)$ respectively. The average displacement of the particles in an interrogation window is determined by cross-correlation of I_1 with I_2 over an interrogation window.

$$c\left(dx, dy\right) = \frac{C\left(dx, dy\right)}{\sqrt{\sigma_1\left(dx, dy\right)}\sqrt{\sigma_2\left(dx, dy\right)}} \tag{3.13}$$

$$C\left(dx, dy\right) = \sum_{x=0, y=0}^{x<n, y<n} \left[I_1\left(x, y\right) - \bar{I}_1\right]\left[I_2\left(x + dx, y + dy\right) - \bar{I}_2\right] \tag{3.14}$$

$$\text{with } -\frac{n}{2} < dx, dy < \frac{n}{2}$$

$$\sigma_1\left(dx, dy\right) = \sum_{x=0, y=0}^{x<n, y<n} \left[I_1\left(x, y\right) - \bar{I}_1\right]^2 \tag{3.15}$$

$$\sigma_2\left(dx, dy\right) = \sum_{x=0, y=0}^{x<n, y<n} \left[I_2\left(x + dx, y + dy\right) - \bar{I}_2\right]^2 \tag{3.16}$$

in which C is the correlation function and c is the normalised correlation function for all integer displacements and n is the size of the interrogation window. The maximum displacement is in this case $\pm n/2$, otherwise the particles move out of the interrogation area and the actual displacement can not be found. A map is constructed of the correlation values, wherein the highest peak indicates the most probable particle displacement, e.g. in figure 3.3. The ratio between the highest peak and the second highest peak is the signal-to-noise ratio. The velocity can be calculated with the detected displacement and the time difference between the two frames using equation 3.17.

$$\vec{V} = \frac{\vec{d}}{\Delta t} \tag{3.17}$$

The main parameters influencing the measurement error are the amount of seeding particles contained in the interrogation window, the velocity gradient in the interrogation window and the size of the particles with respect to their discretisation. The following algorithms are used to take away the bias errors.

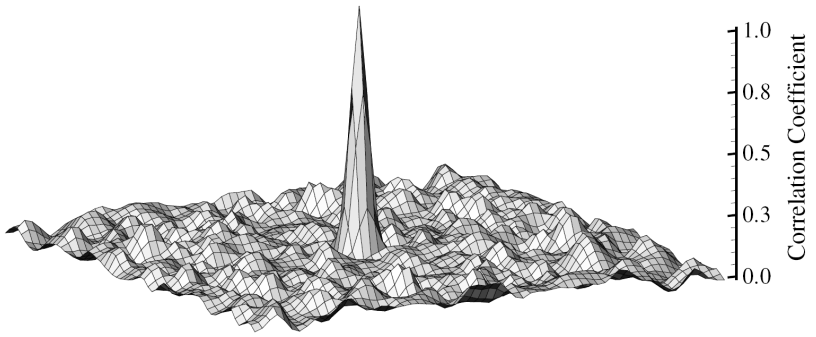

Figure 3.3: Example of a correlation map with a distinct peak (from Raffel [20]).

3.4.1 Window offset

Due to the finite size of the interrogation window, an incorrect estimation of the displacement vector can occur because of the proportional decrease in signal strength with increasing displacements. This comes from the decrease in possible particle matches with increasing displacement. By applying a multiple pass interrogation together with subtraction of the mean light intensity, this bias error can be removed. In the second pass, the interrogation window at time $t_0 + \Delta t$ is offset with the mean value calculated in the first pass. With this offset, the ratio of matched particles with unmatched particles is increased. Correspondingly the probability on a particle match is equal everywhere in the interrogation window, removing the bias.

3.4.2 Multigrid approach

The multiple-pass interrogation described in section 3.4.1 can be improved by a simultaneous implementation of a multi-grid approach. Cross-correlation starts on a grid with large interrogation windows, making the chance on loss of particles much smaller together with an increase in the signal-to-noise ratio. However, this comes at the cost of spatial resolution, since the window consists of less windows. After the first pass, the grid is refined while simultaneously applying a window offset, so both the higher probability of a particle match from the large interrogation window together with the high spatial resolution of the small interrogation window can be achieved.

3.4.3 Window deformation

In areas where large velocity gradients are present within an interrogation window, e.g. in shocks or shear layers, the correlation peak broadens and the signal-to-noise ratio drops. This can be accounted for by deforming the window according to the calculated velocity field, like in figure 3.4. Because of this deformation of the window, less particles pairs are lost and the peak found in the correlation map can be reduced in width, while increasing its height, improving the signal-to-noise ratio significantly in the high velocity gradient areas.

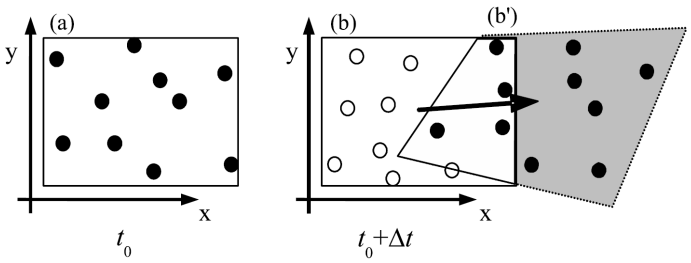

Figure 3.4: Principle of the window deformation technique (from Raffel [20]).

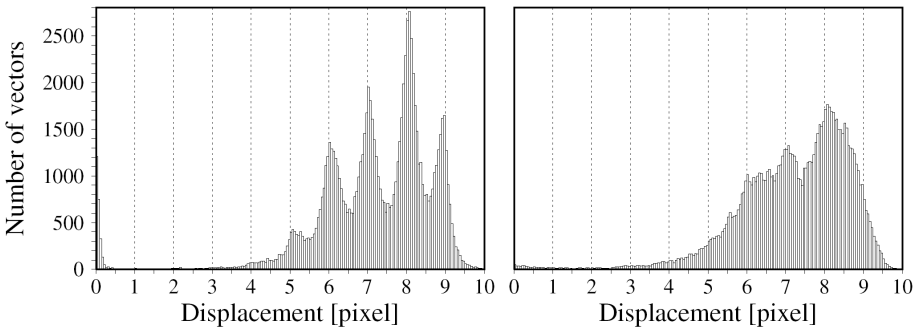

Figure 3.5: Histograms of actual PIV displacement data (from Raffel [20]). Left is the peak-locked data. Right is the non-peak-locked data.

3.4.4 Peak locking

The size of the imaged particles on the sensor has a large influence on the accuracy of the velocity data. The location of the peak on the correlation map is reconstructed with sub-pixel accuracy by means of interpolation. This can be done because the shape of the correlation peak is known, and can be approximated by a Gaussian curve. A number of points on the Gaussian curve is required to estimate the location of the peak with sub-pixel accuracy, therefore the particle should appear larger on the sensor than one pixel. Closing the lens aperture enlarges the imaged particle size meaning more samples of the Gaussian peak, improving the accuracy of the sub-pixel interpolation, but the correlation peak should not become too wide because the accuracy on the exact location of the peak is then decreased. The optimum size of the particles is about 2 pixels [20].

When the particles show up smaller than one pixel, the interpolation can no longer take place. The entire correlation peak is enclosed within the pixel and no information is available on the location of the peak within that pixel. This means the displacements tend to the integer amount of pixels and the data is called peak-locked, see figure 3.5, significantly decreasing the accuracy.

3.5 Stereoscopic PIV

In 3-dimensional flows the out-of-plane component of the velocity is also important, but this can not be measured with conventional 2C-PIV. Another drawback is that the projection of the velocity vector is measured and the out-of-plane component introduces a perspective error. With stereoscopic PIV it is possible to measure this out-of-plane component of the flow, by using two cameras pointed at the same field of view. Another set of two velocity components becomes available. Combining both sets results in an overdetermined system of all three velocity components. How this is done is decribed in subsection 3.5.1.

Two methods are available for stereoscopic placement of the cameras. One is the translational method, in which the two cameras are on the same image plane, the other is the angular displacement method, see figure 3.6. The major problem with the first is that the optical aperture of the lenses does not allow a large deviation from the optical axis and that this is also characterised with a strong decrease in the modulation transfer function toward the edges of the field of view [29]. More suitable is the angular lens displacement, allowing to have the principle lens axis in the middle of the field of view where the best modulation transfer function of the lens is present. If the depth of field is too small to fit the entire measurement plane for a camera not perpendicular to this plane, not the entire image is in focus and a Scheimpflug adapter is required. A detailed description of how this works is given in section 3.5.2. Also the magnification is not constant over the image and a calibration procedure is necessary. How this is implemented is elaborated in section 3.5.4.

3.5.1 Reconstruction method

With two cameras, in total four velocity components in two different image coordinates are available. These can be used to reconstruct the three velocity components in object space, see figure 3.7. This is done according to Willert [29] with the following equations:

$$U = \frac{U_2 \cdot \tan\alpha_1 + U_1 \cdot \tan\alpha_2}{\tan\alpha_1 + \tan\alpha_2} \tag{3.18}$$

$$V = \frac{V_2 \cdot \tan\beta_1 + V_1 \cdot \tan\beta_2}{\tan\beta_1 + \tan\beta_2} \tag{3.19}$$

$$W = \frac{U_1 - U_2}{\tan\alpha_1 + \tan\alpha_2} \tag{3.20}$$

$$= \frac{V_1 - V_2}{\tan\beta_1 + \tan\beta_2} \tag{3.21}$$

However these equations can get a zero numerator when the viewing axes of the cameras are aligned either horizontally or vertically, which can introduce a large error. For example when the two cameras both have their viewing axis in the horizontal plane, both $\tan\beta_1$ and $\tan\beta_2$ is approximately zero for both cameras. In that case equation 3.19 can be rewritten with equation 3.20 and 3.21 to have a better accuracy.

$$V = \frac{V_1 + V_2}{2} + \frac{W}{2}\left(\tan\beta_1 - \tan\beta_2\right) \tag{3.22}$$

$$= \frac{V_1 + V_2}{2} + \frac{U_1 - U_2}{2}\left(\frac{\tan\beta_1 - \tan\beta_2}{\tan\alpha_1 + \tan\alpha_2}\right) \tag{3.23}$$

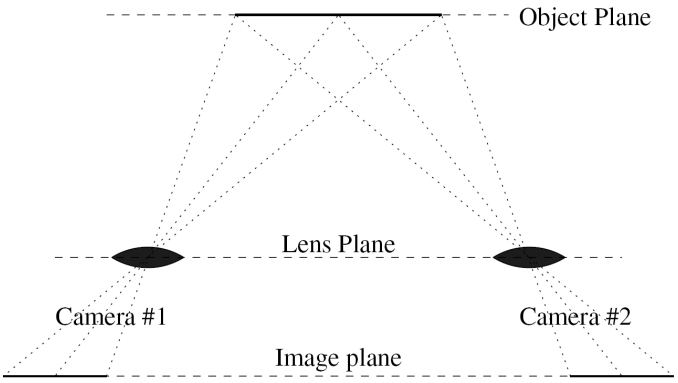

(a) translational method

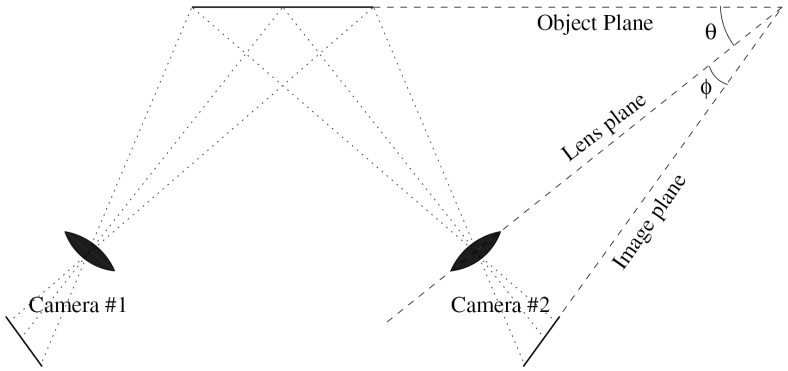

(b) angular method

Figure 3.6: Two configurations that are possible for stereoscopic imaging (from Willert [29])

3.5.2 Scheimpflug condition

Since the depth of field from the lens given by equation 3.12 is limited, and the image plane is not parallel to the object plane in the angular configuration, only part of the image would be in focus. Therefore a Scheimpflug adapter is applied which can rotate the lens plane with respect to the image plane, see figure 3.6(b). To have focus on the full image, the object plane, the lens plane and the image plane should intersect in the same line [18]. The magnification is not constant on the image because of perspective viewing, which is further increased by the Scheimpflug adapter and requires a mapping procedure.

3.5.3 Mapping procedure

The reconstruction with equations 3.18 to 3.21 are only valid under the conditions that the magnification and the viewing angle are constant over the image. With the cameras in angular stereoscopic setup this is not the case and the images have to be dewarped with a mapping procedure. This mapping is done using a third order polynomial following the algorithm of

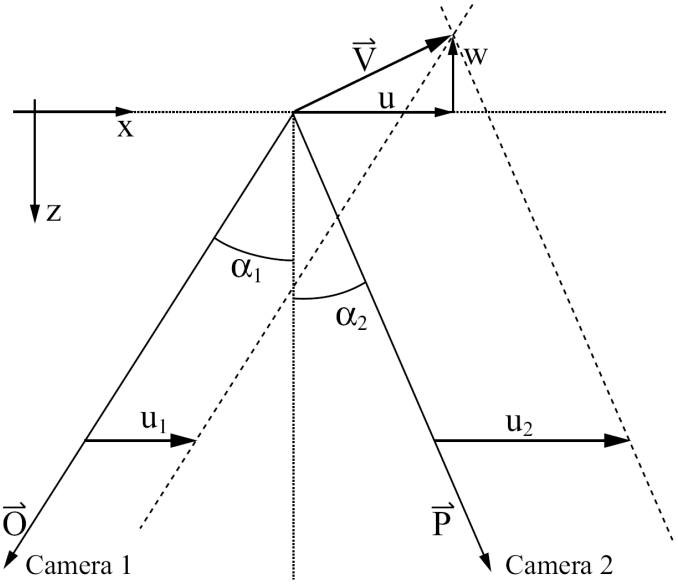

Figure 3.7: Reconstruction of the out-of-plane component using a stereoscopic configuration (from Raffel [20]).

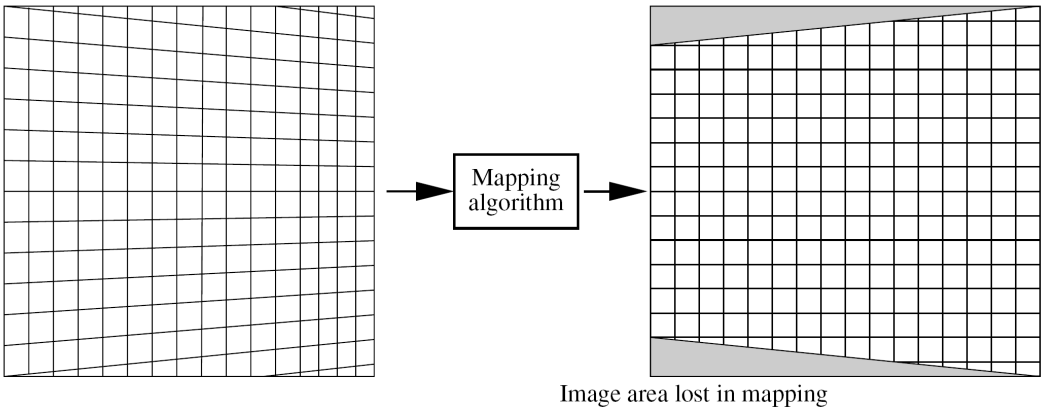

Figure 3.8: Dewarping of the images transforming the square into a trapezoid (from Raffel [20]).

Fei [9].

$$X_0 = a_1X_i^3 + a_2Y_i^3 + a_3X_i^2Y_i + a_4X_iY_i^2 + a_5X_i^2 + a_6Y_i^2 + a_7X_iY_i + a_8X_i + a_9Y_i + a_{10} \quad (3.24)$$

$$Y_0 = b_1X_1^3 + b_2Y_i^3 + b_3X_i^2Y_i + b_4X_iY_i^2 + b_5X_i^2 + b_6Y_i^2 + b_7X_iY_i + b_8X_i + b_9Y_i + b_{10} \quad (3.25)$$

The unknown parameters can easily be determined using a least squares approach. The advantage of this mapping procedure is that it is robust and the imaging parameters such

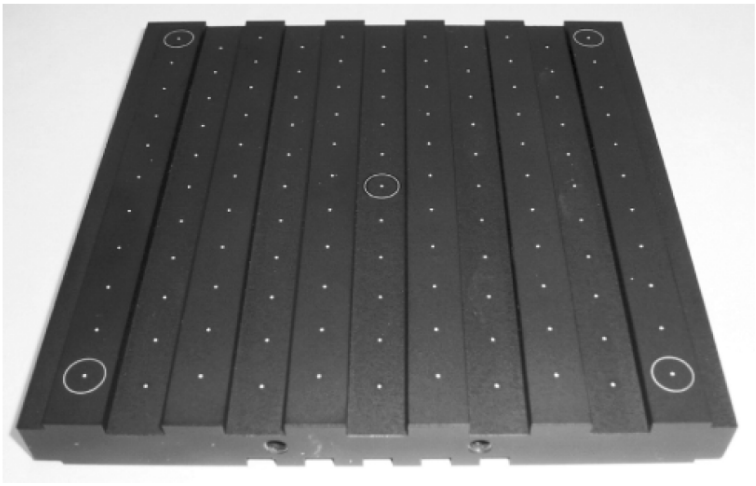

Figure 3.9: Two-level calibration plate with dots at fixed distance (from Raffel [20].

as magnification factor and focal length never need to be determined. Non-linear distortions such as from lens aberrations are also accounted for by the second and third order terms in the mapping function. To reconstruct the velocities from equation 3.18 to 3.21, the viewing angles have to be determined. This is done according to Scarano [21] in the following way:

$$\tan\alpha = \frac{\delta x_{img}}{\delta z}\frac{dx_{proj}}{dx_{img}} = \frac{D_U^+ - D_U^-}{\delta z}\cdot\left(\frac{1}{1+\partial D_U/\partial x}\right) \tag{3.26}$$

$$\tan\beta = \frac{\delta y_{img}}{\delta z}\frac{dy_{proj}}{dy_{img}} = \frac{D_V^+ - D_V^-}{\delta z}\cdot\left(\frac{1}{1+\partial D_V/\partial y}\right) \tag{3.27}$$

in which D_U^+, D_U^-, D_V^+ and D_V^- are the horizontal and vertical dewarping fields of the images for the two different levels of the calibrationplate and δz is the distance between these levels. Because of this mapping procedure the square image is transformed in a trapezoid, see figure 3.8.

3.5.4 Calibration

In order to solve the unknown parameters from equations 3.24 and 3.25 a calibration procedure is used which makes use of a calibration plate consisting of a fixed dot pattern at two different levels, see figure 3.9. Because the dot pattern and the difference in depth of the two levels is known, the dewarping field D_U^+, D_U^-, D_V^+ and D_V^- can be determined. An initial dewarping field is determined by clicking some of the dots on the calibration plate images manually. This is then evaluated using the cross-correlation technique on the dewarped image and the artifial image of the calibration plate to obtain a higher accuracy. Finally to obtain the dewarping field $\bar{D}_L^0$ and $\bar{D}_R^0$ the two dewarping fields at different depths are interpolated linearly.

3.5.5 Self-Calibration

The dewarping fields are determined accurately using the calibration method described in section 3.5.4. However, misalignment of the calibration plate with the laser sheet may introduce significant errors in the calibration. Two different misalignments can occur: an offset of

the calibration plate with the actual measurement plane and a rotational misalignment with the measurement plane, see figure 3.10. It is possible to correct this misalignment a posteriori with the recorded images.

This correction is done by the cross-correlation of two images taken at the same time instance by the two different cameras. The resulting vector is called the disparity vector and should approach zero with a correct calibration. A misalignment of the calibration plate will result in a non-zero disparity vector, which can be used to correct for the misalignment by two different methods.

One method is to improve the mapping function. This is done by updating the dewarping fields from the original calibration procedure with the disparity vector according to equations 3.28 to 3.31.

$$\vec{D}_L^{+\,corrected} = \vec{D}_L^{+\,calibration} + \left(1 + \frac{\partial \vec{D}_L}{\partial \vec{x}}\right) \cdot c_L \vec{R} \tag{3.28}$$

$$\vec{D}_L^{-\,corrected} = \vec{D}_L^{-\,calibration} + \left(1 + \frac{\partial \vec{D}_L}{\partial \vec{x}}\right) \cdot c_L \vec{R} \tag{3.29}$$

$$\vec{D}_R^{+\,corrected} = \vec{D}_R^{+\,calibration} + \left(1 + \frac{\partial \vec{D}_R}{\partial \vec{x}}\right) \cdot c_R \vec{R} \tag{3.30}$$

$$\vec{D}_R^{-\,corrected} = \vec{D}_R^{-\,calibration} + \left(1 + \frac{\partial \vec{D}_R}{\partial \vec{x}}\right) \cdot c_R \vec{R} \tag{3.31}$$

In which $\vec{R}$ is the disparity vector and the superscripts $+$ and $-$ denote the different levels of the calibration plate. The subscripts L and R denote the left and right camera respectively. The coefficients c_L and c_R are introduced to split the disparity vector in two parts with $c_L + c_R = 1$. The non-uniform magnification is taken into account by the term $1 + \partial\vec{D}/\partial\vec{x}$.

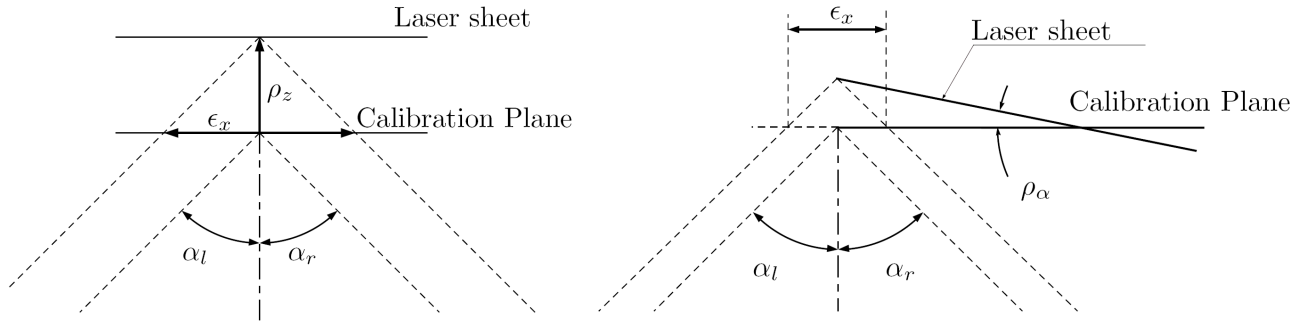

(a) Translation misalignment

(b) Rotation misalignment

Figure 3.10: Misalignment of the calibration plate w.r.t. the measurement plane (from Scarano [21].

The coefficients are defined in the following way:

$$c_L = \frac{\tan \alpha_L}{\tan \alpha_L + \tan \alpha_R} \tag{3.32}$$

$$c_R = \frac{\tan \alpha_R}{\tan \alpha_L + \tan \alpha_R} \tag{3.33}$$

With the updated values of the dewarping fields $\vec{D}_R^+$, $\vec{D}_R^-$, $\vec{D}_L^+$ and $\vec{D}_L^-$ the mapping function is recalculated. With this new mapping functions also angles α and β are recalculated. A new disparity vector is recalculated, which should be smaller than the previous one. This process is repeated until the mapping does not improve anymore.

Another method uses the original mapping function, where the angles are corrected using the disparity vectors. This is done by the following functions [21]:

$$\rho_\alpha = \frac{\partial R_U / \partial x_{dw}}{\tan(\alpha_L) - \tan(\alpha_R)} \tag{3.34}$$

$$\rho_\beta = \frac{\partial R_V / \partial y_{dw}}{\tan(\beta_L) - \tan(\beta_R)} \tag{3.35}$$

With this adapted calibration, a new disparity vector field is calculated, in which the disparity should be smaller than the previous one. This process is repeated until the disparity vectors are sufficiently small or do not improve anymore.

The exact location of the measurement plane with respect to the calibration plane is caluclated from:

$$z^{corr} = Z_0 + \frac{R_U}{\tan(\alpha_L) - \tan(\alpha_R)} \tag{3.36}$$

Chapter 4

Experimental Apparatus

This chapter describes the facilities and setup. First some details are given about the wind tunnel in section 4.1 and the model in section 4.2. Then the Schlieren setup is described in section 4.3. Specifications for oil flow visualisation are given in section 4.5. The details of the PIV setup is given in section 4.6, which is subdivided into subsections about the seeder (section 4.6.1), Illumination and imaging (section 4.6.2) and the data processing procedure (section 4.6.3).

4.1 Flow facility

The experiments have been performed in the transonic supersonic blow-down facility TST-27 at the high-speed laboratories of Delft University of Technology, see figure 4.1 and 4.2. The test section dimensions are $280mm \times 260mm$. The Mach number ranges from 0.4 - 4.2 in the test section, accurately controlled by a continuous adjustable throat section. Dry air with a relative humidity ratio of $4.1 \cdot 10^{-6}$ is supplied from a $300m^3$ pressure vessel at 40 bar. A flow control valve regulates the air into the settling chamber and maintains a constant stagnation pressure. The stagnation temperature is approximately $T_0 = 285K$. The freestream turbulence level is approximately 1% ($5m/s$ at $M_\infty = 2.0$). Fluctuations in stagnation temperature of maximum $5K$ result in differences of mean freestream velocity of $4m/s$. A Schlieren window in the test section allows for optical access to the test section.

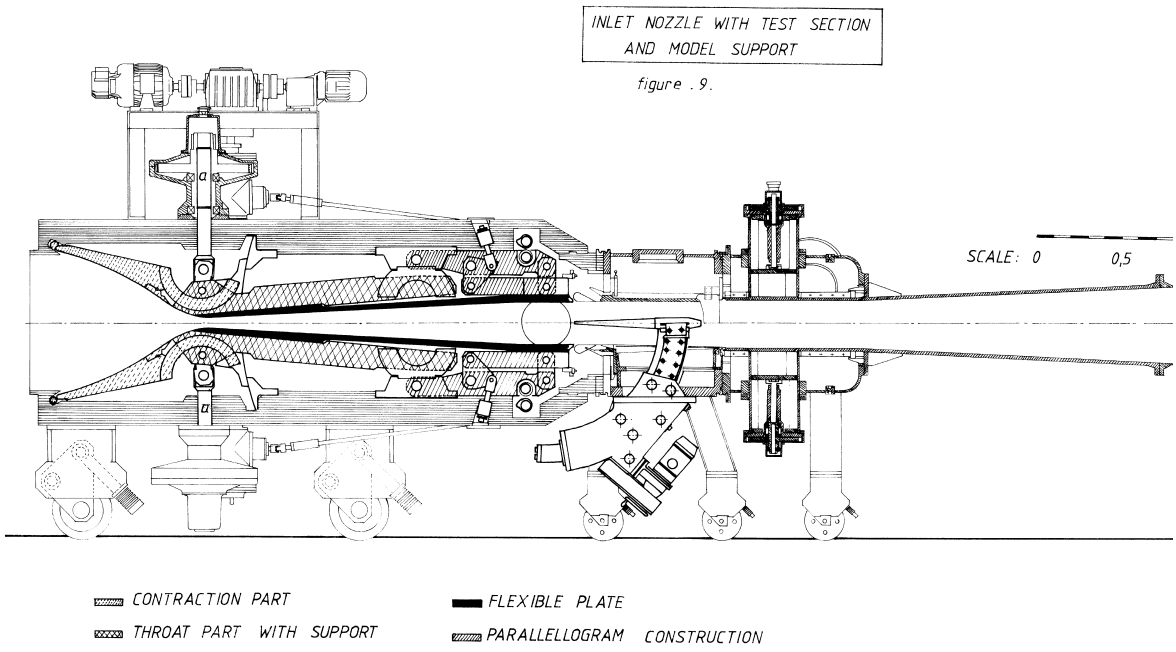

Figure 4.1: Schematic overview of the TST-27 windtunnel

Figure 4.2: The TST-27 blow-down facility

4.2 Model

A triangular $10mm$ thick delta wing having a flat upper surface and sharp leading edges with a 65° leading edge sweep is manufactured in stainless steel. The root chord is $120mm$ and the span is $112mm$ resulting in an aspect ratio of $A = 1.87$. The Reynolds number based on the chord length is approximately $Re_c = 1.6 \cdot 10^6$. The leading edge bevel angle is 30°, as presented in figure 4.3. The model is mounted on a $8mm$ thick support, see figure 4.9, starting at $50mm$ from the apex and 45° inclined. The support leading edge has a deflection angle of 11.3° which generates a weak attached shock at the windward surface. The sting allows adjustment of the angle of attack.

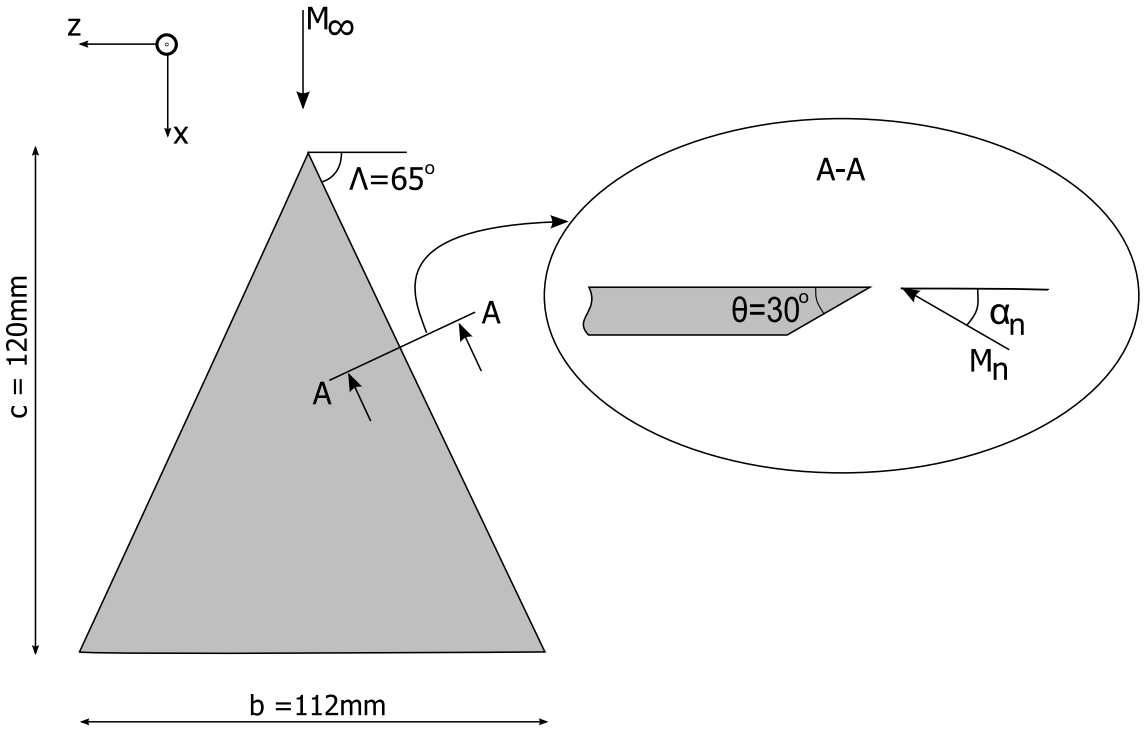

Figure 4.3: Delta wing model.

4.3 Schlieren setup

A standard side-view Schlieren setup is used consisting of two parabolic mirrors at either side of the wind tunnel, an Osram XBO 150 W/1 continuous Xenon light source and a Photron Fastcam CMOS camera ($1024x1024$ pixels, 12 bits), see figure 4.4. The light from passes a $1mm$ diameter pinhole to assure the light beam is collimated. The Schlieren-knife is oriented horizontally for obtaining the best visualisation of the vortex and shocks.

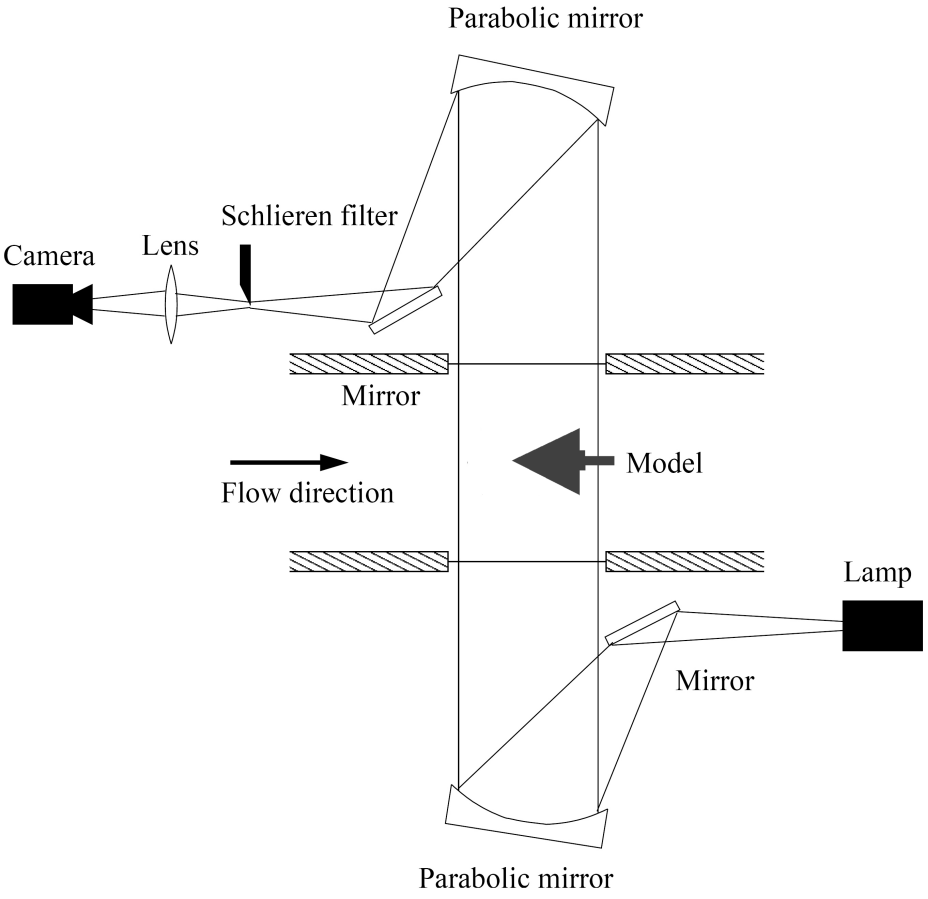

Figure 4.4: Overview of the Schlieren setup.

4.4 Shadowgraphy

For shadowgraphy illumination is provided by a Xenon filled Fisher R138 Nanolite spark light source with pulse time of approximately $20ns$. The light passes through a pinhole with an aperture of approximately $1cm$ to assure the light rays to be parallel. The same setup as for Schlieren is used, given in figure 4.4 except that the Schlieren filter is removed. The light is collected by a Nikon D80 camera (3872×2592 pixels CCD sensor) that is shifted during windtunnel operation to obtain a correct imaging plane positioning.

4.5 Oil Flow visualisation

For oil flow visualisation a mixture is applied to the complete model leeward surface consisting of Shell "Tellus 29" oil, titaniumoxide (TiO_2) and oleic acid, which is used to modify the viscosity of the oil. After the wind tunnel start, the oil dries quickly fixing it to the surface of the model. During the wind tunnel run the model is observed to see the influence the starting and stopping process on the oil pattern, which appeared to be negligible. Photographs are taken after the wind tunnel stop.

4.6 Particle Image Velocimetry

This section describes the PIV setup. Section 4.6.1 describes the generation of tracer particles. In section 4.6.2 the laser and camera setup is described. The processing of the images is elaborated in section 4.6.3.

4.6.1 Seeder

Di-Ethyl-Hexyl-Sebacat (DEHS) is used as tracer particle material. A Pivtec PivPart45 aerosol generator containing 45 Laskin nozzles produces approximately 10^8 particles per second with a median size of $1\mu m$, see figures 4.5 and 4.6. Additionally an impactor plate is installed to remove the largest particles. The seeding particles are dispersed through a seeding rake into the settling chamber creating a seeded streamtube with a cross section of approximately $10cm \times 10cm$ in the test section.

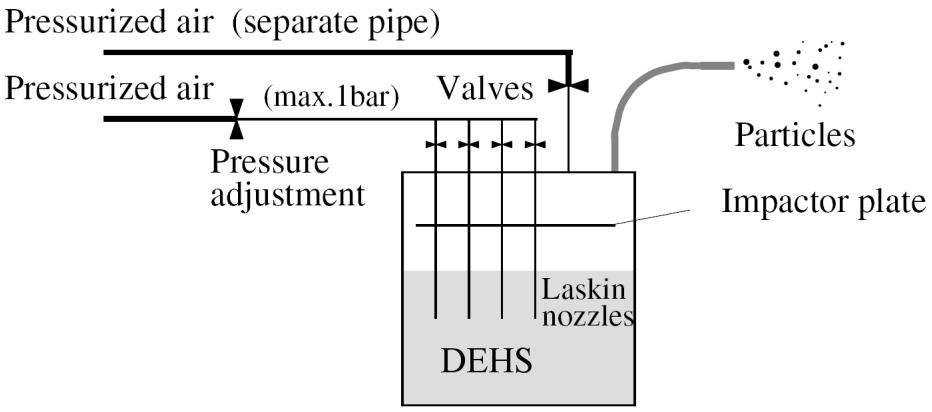

Figure 4.5: Principle of the particle generator (from PivPart45 user manual [2]).

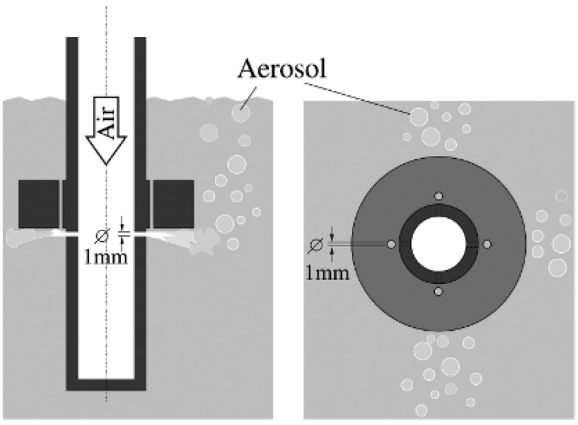

Figure 4.6: Sketch of the laskin nozzles (from PivPart45 user manual [2]).

The relaxation time of these particles inferred from a shock wave test, like the ones from

Schrijer [22], is 2.1 μs. Rewriting equation 3.3 from Melling [15] gives equation 4.1.

$$d_p = \sqrt{\frac{18\mu_f \tau_p}{\rho_p}} \tag{4.1}$$

Using this equation a particle diameter of 0.7 μm is found using a particle density of $\rho_p = 0.91 \cdot 10^3$ and a viscosity in the free stream conditions of $1.1 \cdot 10^{-5} Pa \cdot s$.

4.6.2 Illumination & imaging

A Spectra-Physics Quanta-Ray Nd:YAG double pulsed laser is used to illuminate the tracer particles. It emits laser light with a wavelength of $532nm$ with a maximum energy of $400mJ$ per pulse during $6ns$. The laser sheet is aligned in streamwise direction to minimize particle pair loss by having the largest component of the flow in the plane of measurement. The pulse delay time is set to $2\mu s$, which corresponds to a particle image travel between exposures of 16 pixels in the free stream at $M_\infty = 2.0$. The laser beam is introduced by an optical probe downstream of the test section, containing cylindrical and spherical lenses to shape the beam into a light sheet of approximately $1.5mm$ in thickness and $7cm$ in height at the model position, see figure 4.7

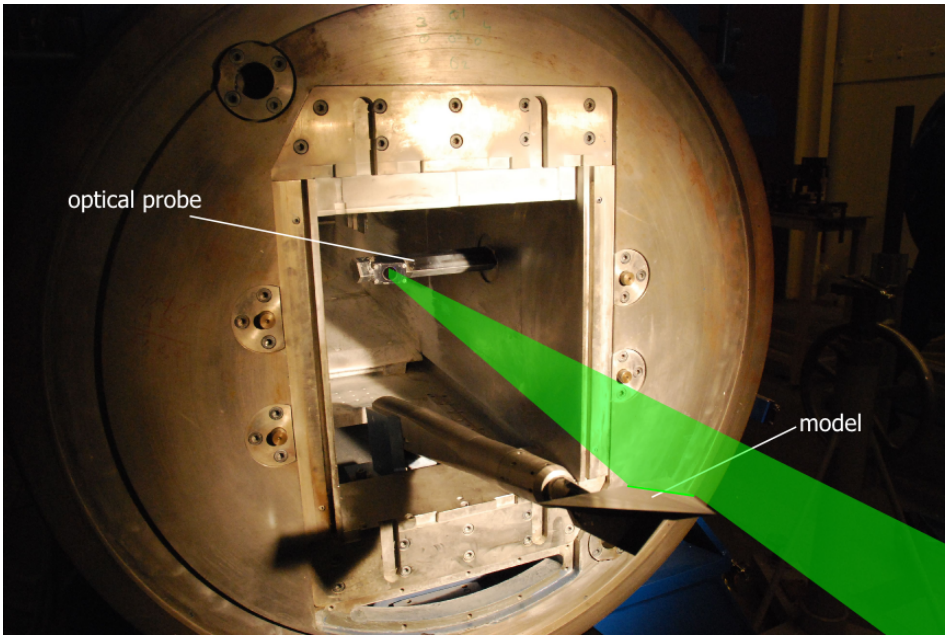

Figure 4.7: The test section showing the model on the sting and the moving optical probe inserting the light sheet.

Two PCO Sensicam QE 12-bit Peltier-cooled CCD cameras with frame-straddling architecture and a 1376×1040 pixel sized sensor are used to record the light scattered by the particles. The cameras are arranged in a stereoscopic arrangement as depicted in figure 4.8, having an angle between the cameras of approximately 30°. Although suboptimal for out-of-plane component accuracy [19], this configuration is chosen to enable at the same time a 2C analysis by the camera perpendicular to the light sheet. The camera perpendicular to the light sheet is

equipped with a Nikkor $50mm$ focal objective with a focal number of $f_{\#} = 9.6$, the other with a Nikkor $60mm$ focal objective with $f_{\#} = 11$, which also uses a Scheimpflug adapter. The $f_{\#}$ for the optimal diffraction size of 2 pixels per particle for both cameras is approximately 9.0. Translation of the light sheet along spanwise direction is made by a controlled sliding of the laser periscope. The cameras are mounted on a sliding device allowing simultaneous translation with the laser sheet, eliminating the need for refocussing. This approach results in a constant magnification for the different measurement positions. Because a symmetric flow is assumed, measurements are limited to half the model. The $83mm \times 62mm$ field of view is slided in spanwise direction with a $3mm$ pitch distance in the range of $60mm$ from the midsection, resulting in 21 measurement planes, see figure 4.9. For each slice a data ensemble of 100 image pairs per camera is acquired.

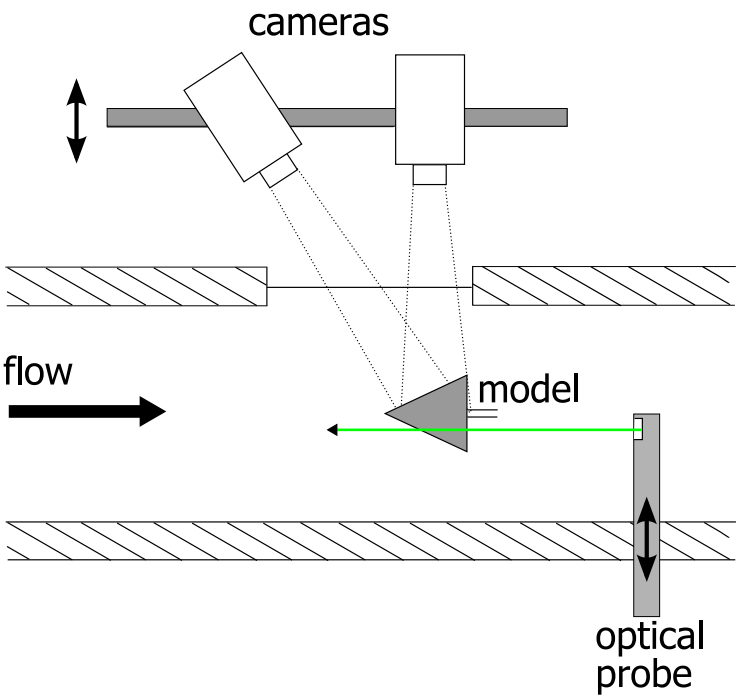

Figure 4.8: Schematic overview of the illumination and imaging configuration.

4.6.3 Data processing

Data processing is done using LaVision DaVis 7.4 software. An interrogation window size of 32×32 pixels is used, corresponding to a measurement area of $1.9mm \times 1.9mm$. An overlap factor of 50% is used resulting in an in-plane vector pitch of $0.95mm$. The misalignment between the light sheet and the measurement plane as obtained by the calibration procedure is eliminated by using the self calibration procedure that is described in section 3.5.5, which is available in the software. The images are analysed by an iterative multigrid window deformation method, presented in section 3.4.3. The small pitch distance of $3mm$ between the measurement planes and the flow repeatability allows to combine the average flow field from the individual planes to construct a full 3-dimensional representation of the flow field.

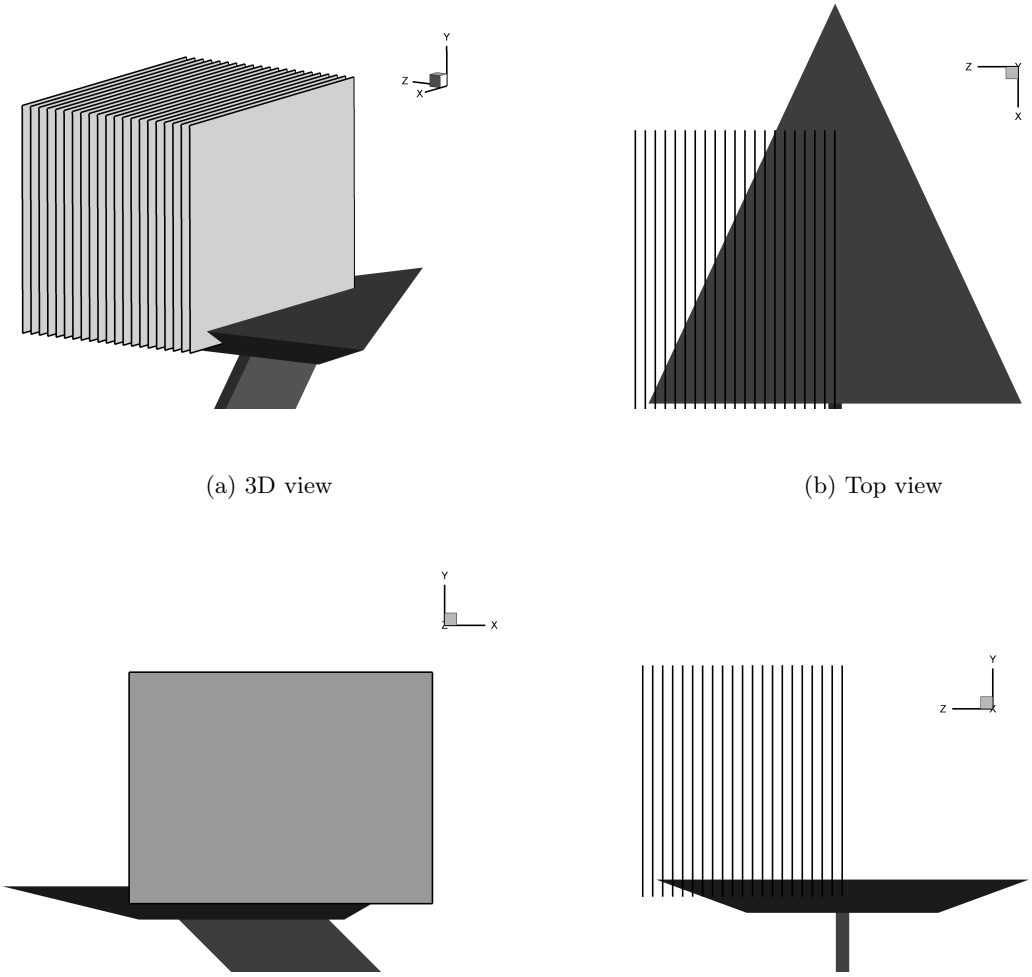

(a) 3D view

(b) Top view

(c) Side view

(d) Back view

Figure 4.9: Measurement areas on the delta wing.

4.7 Test matrix

In total 4 cases have been investigated, which are given in table 4.1, using oil flow visualisation, Schlieren visualisation, shadowgraphy and PIV. A high angle of incidence is chosen to enlarge the vortex for easy detection. On the other hand, this gives high accelerations and large particle slip, reducing the accuracy of PIV.

α	M_∞	α_N	M_N	p_0	T_0	Re_c	Measurement method
10°	2.0	22.6°	0.90	$2.7 \cdot 10^5$ Pa	285 K	$1.6 \cdot 10^6$	Schlieren, Shadowgraphy, Oil Flow, PIV
15°	2.0	32.4°	0.97	$2.7 \cdot 10^5$ Pa	285 K	$1.6 \cdot 10^6$	Schlieren, Shadowgraphy, Oil Flow, PIV
18°	1.7	37.6°	0.86	$2.3 \cdot 10^5$ Pa	285 K	$1.6 \cdot 10^6$	Schlieren, Shadowgraphy, Oil Flow, PIV
18°	2.0	37.6°	1.01	$2.7 \cdot 10^5$ Pa	285 K	$1.6 \cdot 10^6$	Schlieren, Shadowgraphy, Oil Flow, PIV

Table 4.1: The test matrix

Chapter 5

Results

5.1 Schlieren & Shadowgraphy

For all different flow cases Schlieren images have been made with the Schlieren knife oriented horizontally, see figures 5.2 to 5.5. Clearly visible on both Schlieren and shadowgraph images is a shockwave on the windward surface. A Mach wave on the leeward surface coming from the apex is visible only on the Schlieren images. The primary vortex is visualised by both methods. In the vortex core the density is lower than the surrounding density. Since Schlieren visualisation the gradient of the refractive index corresponding to $\nabla\rho$ is measured, while with shadowgraphy the measured quantity corresponds $\nabla^2\rho$, resulting in a light intensity distribution through a vortex as shown in figure 5.1. So in the Schlieren photographs, the vortex is represented by a bright and dark line, while in the shadowgraphs the vortex is visible as a darker region bounded by two brighter regions, see figures 5.6 to 5.9. The $\alpha = 18°$, $M_\infty = 1.7$ case shows multiple bright lines in the vortex region, suggesting the presence of secondary vortices. Furthermore, in the Schlieren images the boundary layer is visible by another bright line. In the area above the vortices an expansion is present, which is shown by a bright region in the Schlieren images.

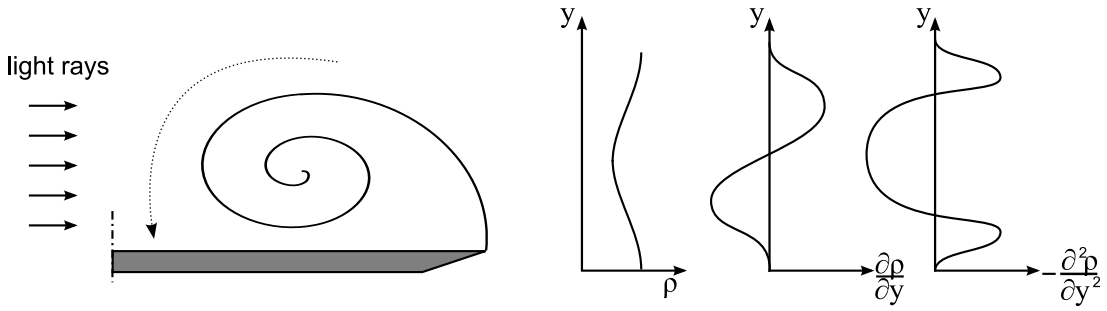

Figure 5.1: Schematic overview of density through a vortex.

The Mach wave coming from the top of the images in the Schlieren photographs is due to a pressure hole present in the top wall of wind tunnel. About halfway the wing a series of Mach waves are emerging from the wing, due to the presence of inequalities from the bolts used to attach the wing surface to the support. With increasing angle of attack these are tilted back further due to the locally inclined velocity direction and a locally higher Mach number.

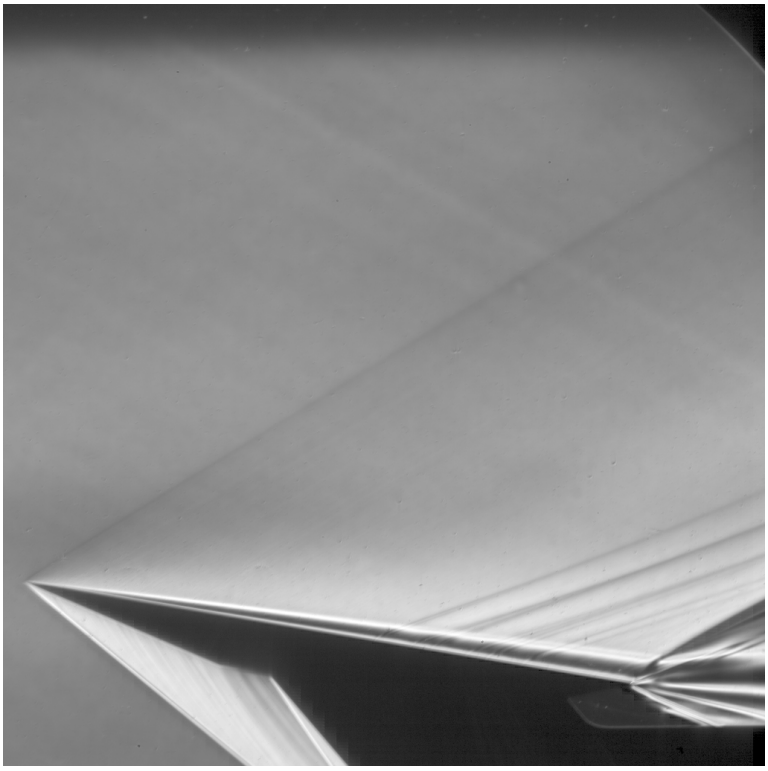

Figure 5.2: Schlieren image at $\alpha = 10°$ and $M_\infty = 2.0$.

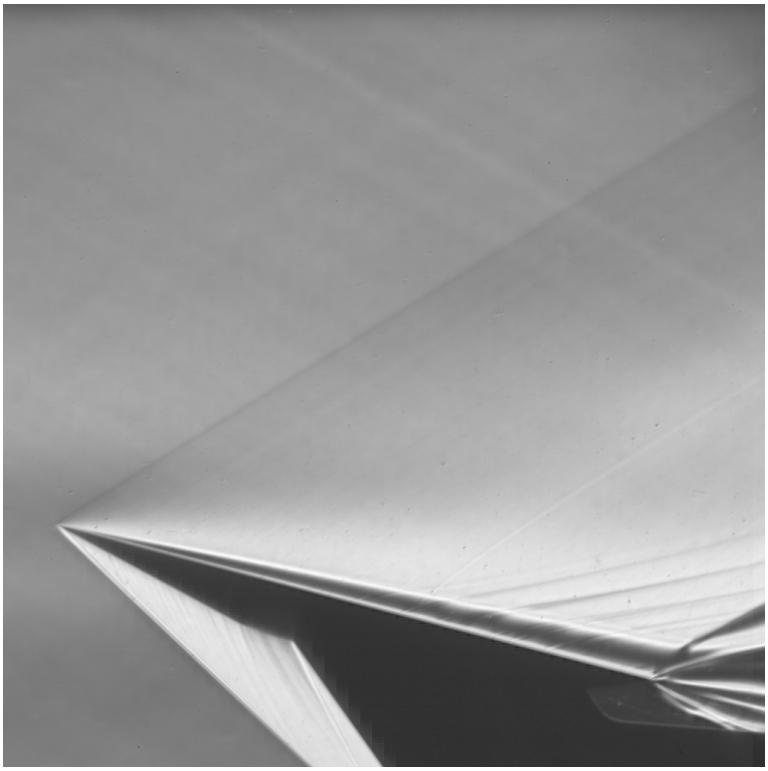

Figure 5.3: Schlieren image at $\alpha = 15°$ and $M_\infty = 2.0$.

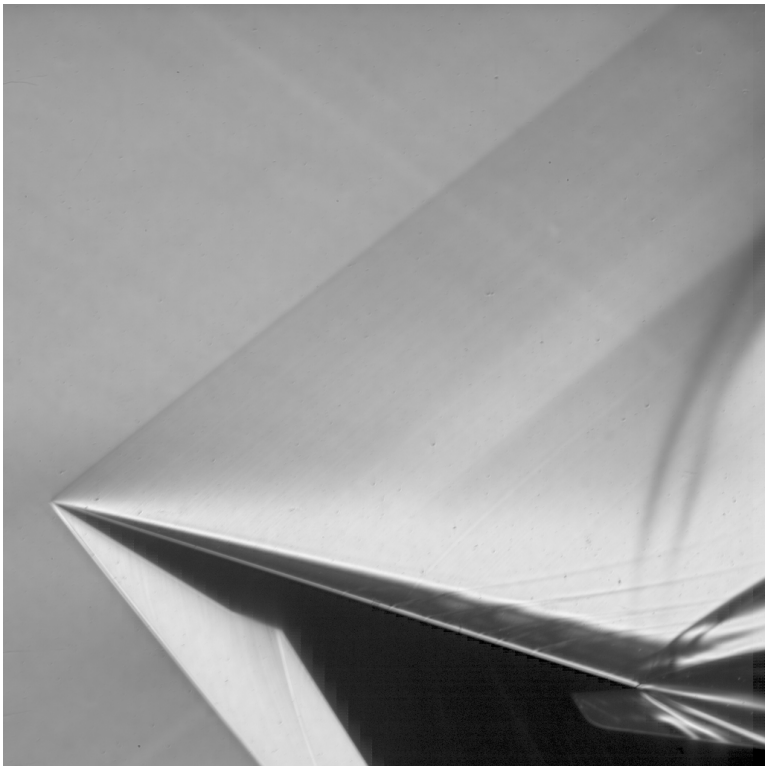

Figure 5.4: Schlieren image at $\alpha = 18^\circ$ and $M_\infty = 1.7$.

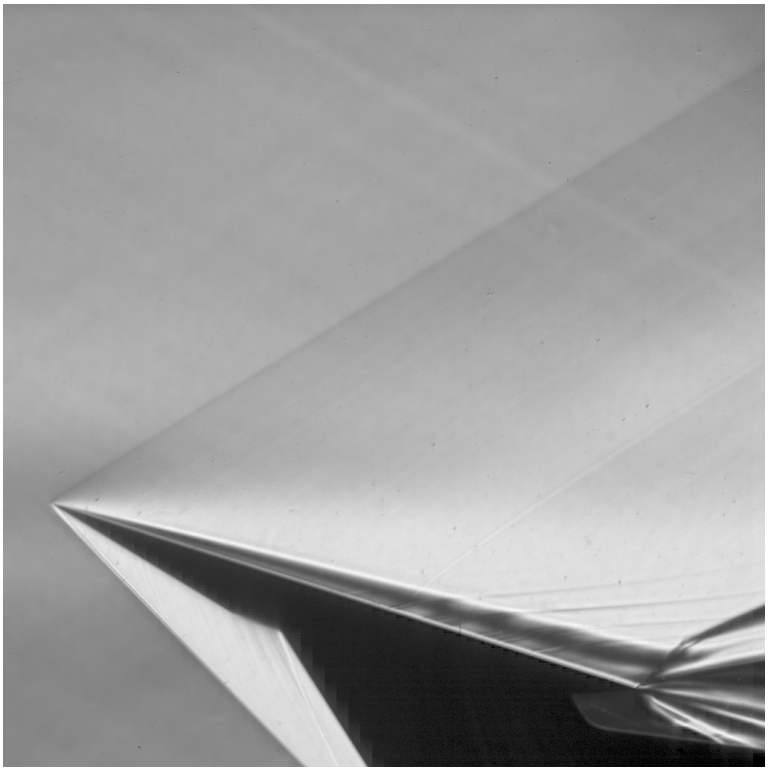

Figure 5.5: Schlieren image at $\alpha = 18^\circ$ and $M_\infty = 2.0$.

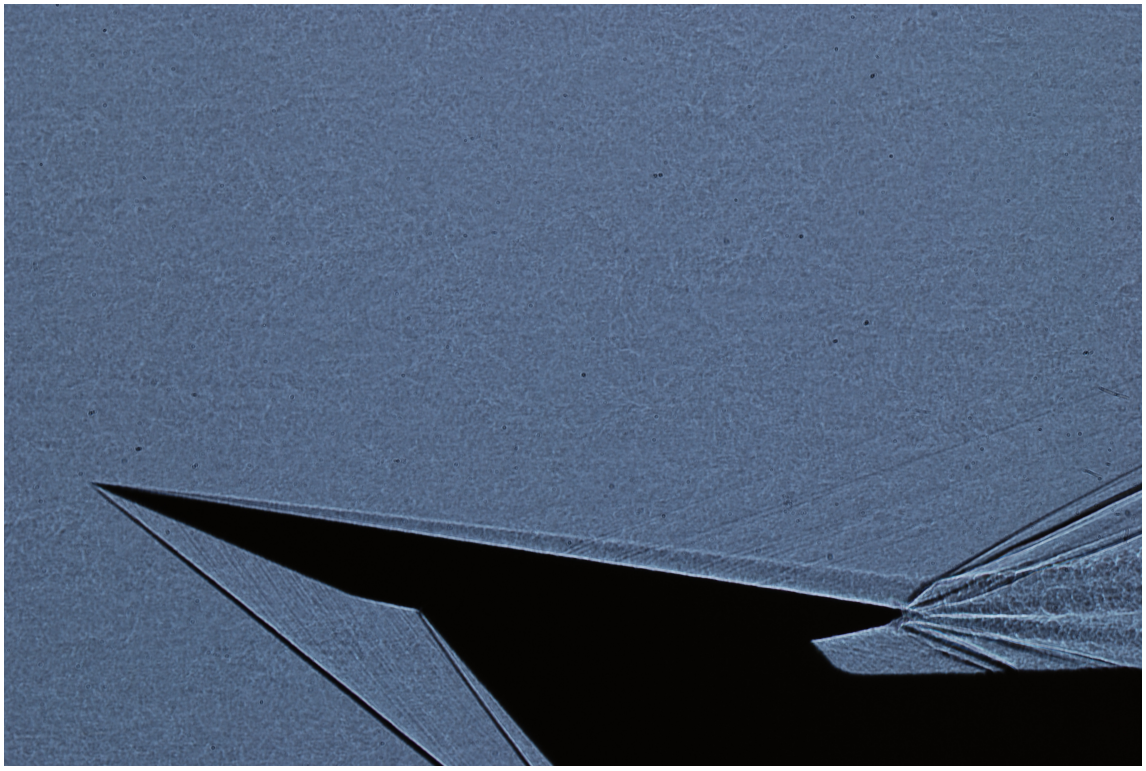

Figure 5.6: Shadowgraph at $\alpha = 10°$ and $M_\infty = 2.0$.

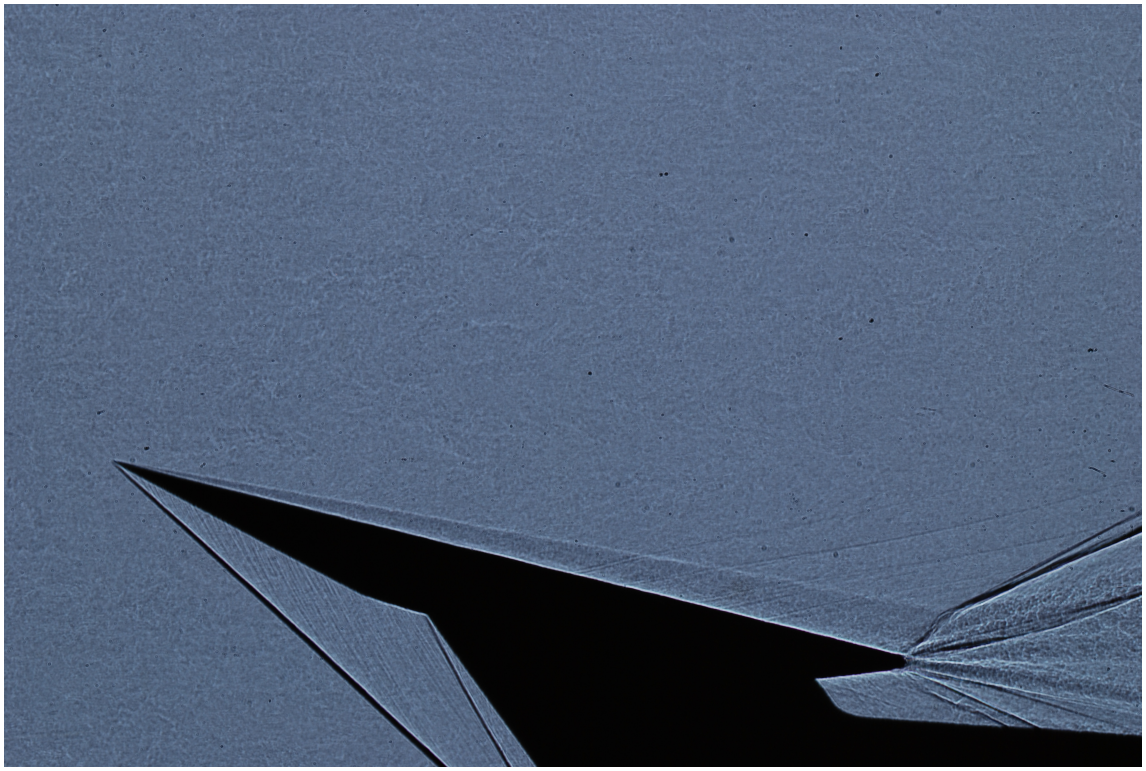

Figure 5.7: Shadowgraph at $\alpha = 15°$ and $M_\infty = 2.0$.

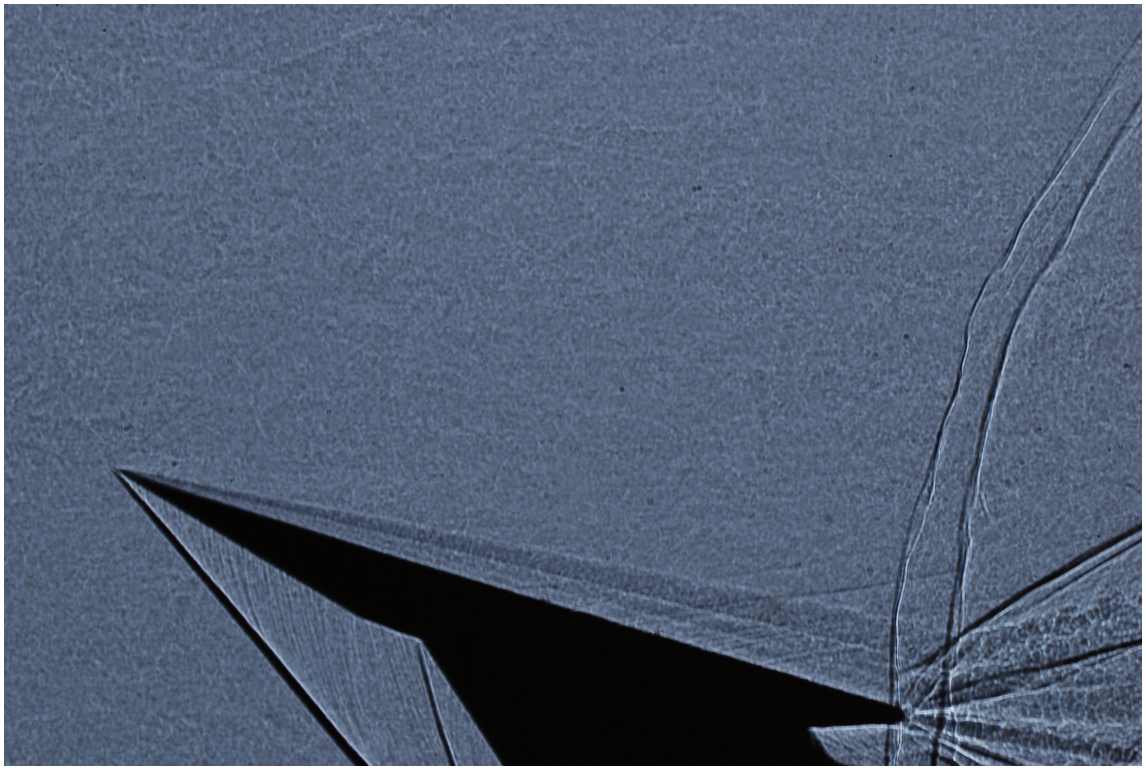

Figure 5.8: Shadowgraph at $\alpha = 18°$ and $M_\infty = 1.7$.

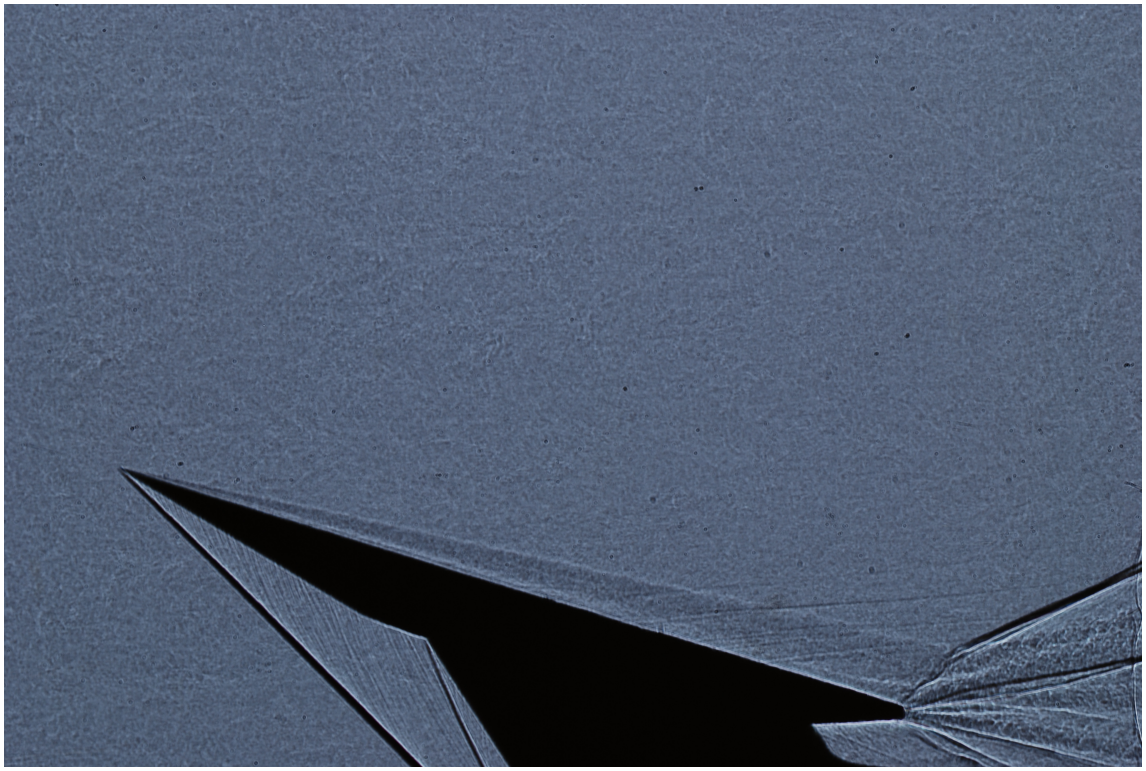

Figure 5.9: Shadowgraph at $\alpha = 18°$ and $M_\infty = 2.0$.

5.2 Oil flow visualisation

A schematic overview of the oil flow visualisation is given in figures 5.10 and 5.11. The air detaches at the leading edge and reattaches inboard on the wing which transports the oil away. This is shown as the primary reattachment line a_1. Inboard of this line the flow remains attached and the oil streaks have a linear path. Outboard of this line the oil streaks show a curved path until the secondary separation line s_2. This shows up as a thick line because accumulation of oil takes place here. This scheme can be repeated for the secondary reattachment a_2 and tertiary separation s_3.

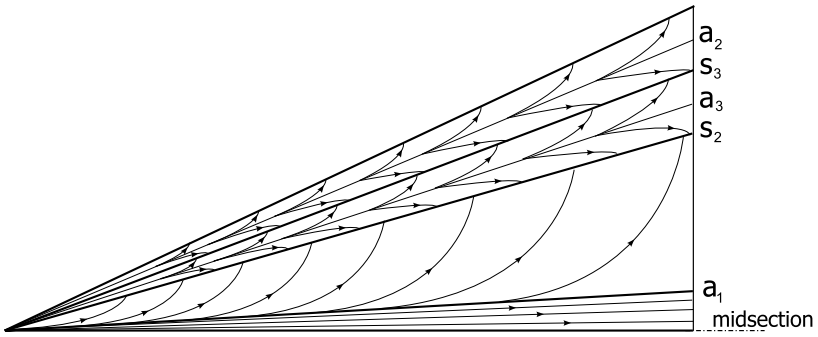

Figure 5.10: Schematic overview of the oil flow surface pattern.

The pictures of the oil streak patterns are presented in figure 5.12 to 5.15. Clearly visible in all images is the primary reattachment line and the secondary separation line. However, no secondary reattachment line is present for the $M_\infty = 2.0$ cases, but there is some accumulation of oil present between the leading edge and the secondary seperation line. For the case of $M_\infty = 1.7$ there is a clear secondary reattachment and tertiary separation line. This confirms the shadowgraph observations that suggested secondary vortices for this case. Obvious is is the decreasing area of attached flow at the midsection with increasing angle of attack. The primary vortex becomes larger bringing the primary reattachment line closer to the midsection.

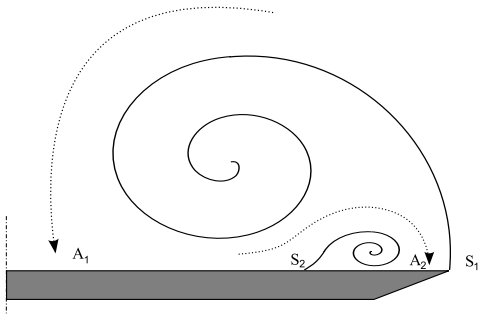

Figure 5.11: Schematic overview of a cross section of a vortex system with a primary and a secondary vortex.

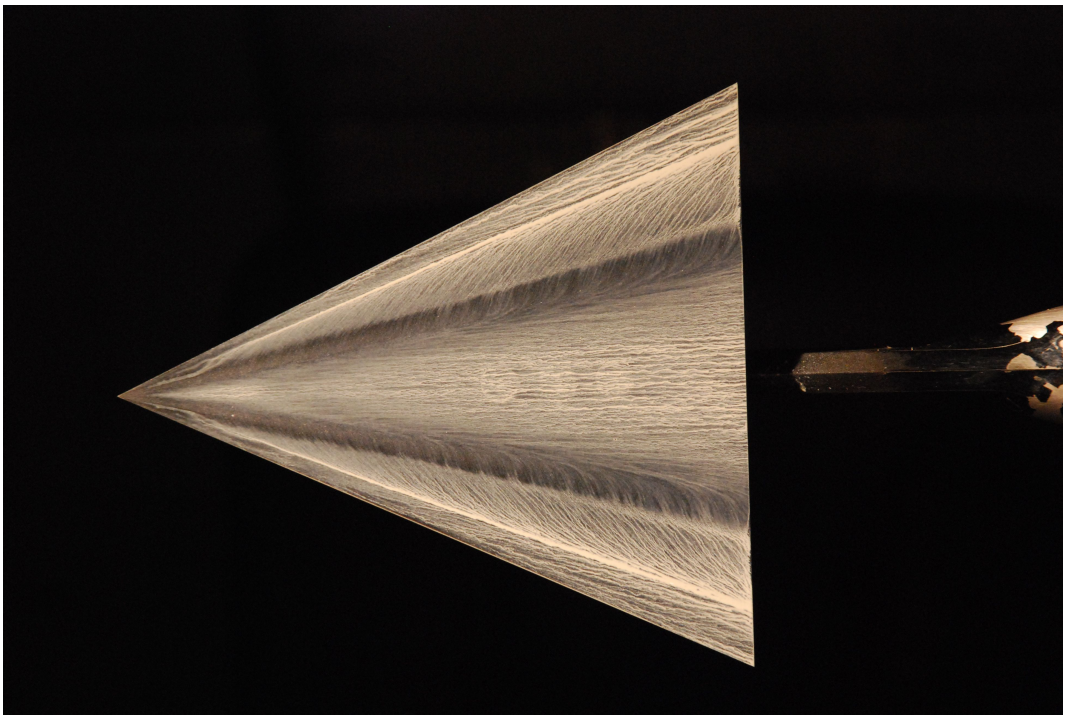

Figure 5.12: Oil flow for $\alpha = 10°$ and $M_\infty = 2.0$.

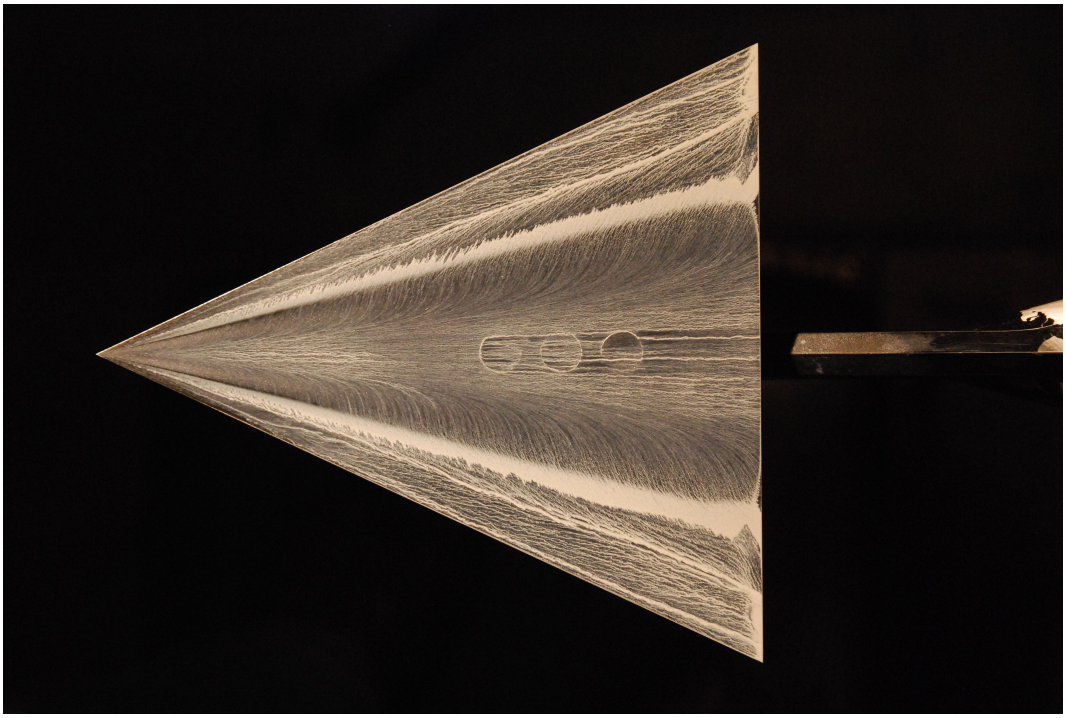

Figure 5.13: Oil flow for $\alpha = 15°$ and $M_\infty = 2.0$.

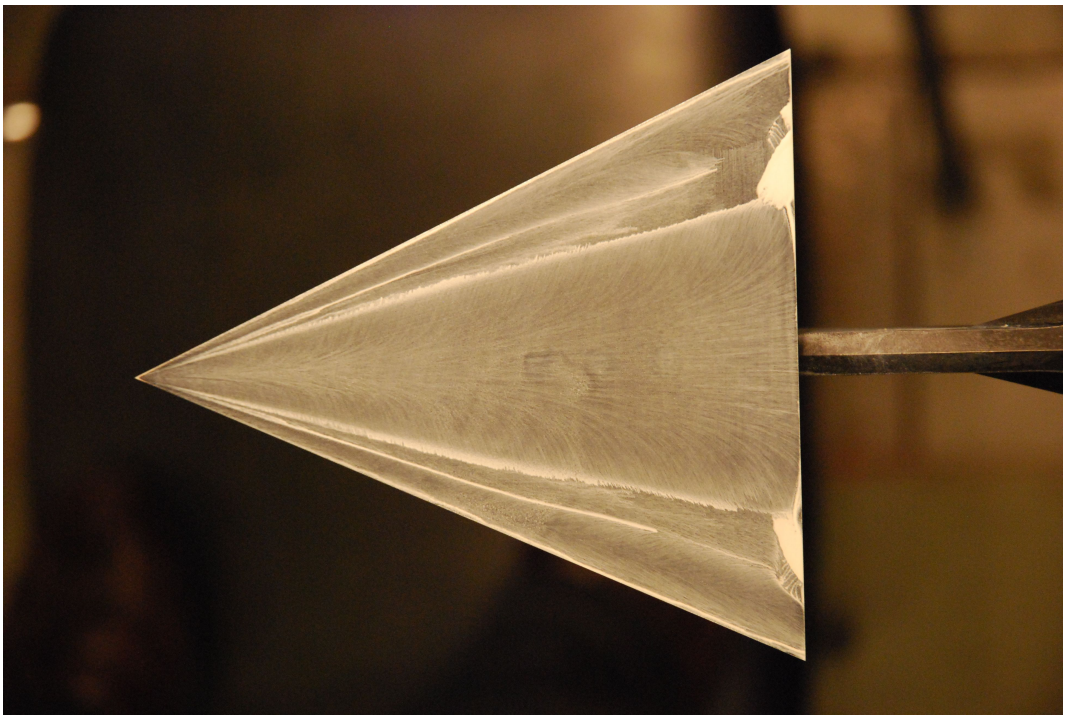

Figure 5.14: Oil flow for $\alpha = 18°$ and $M_\infty = 1.7$.

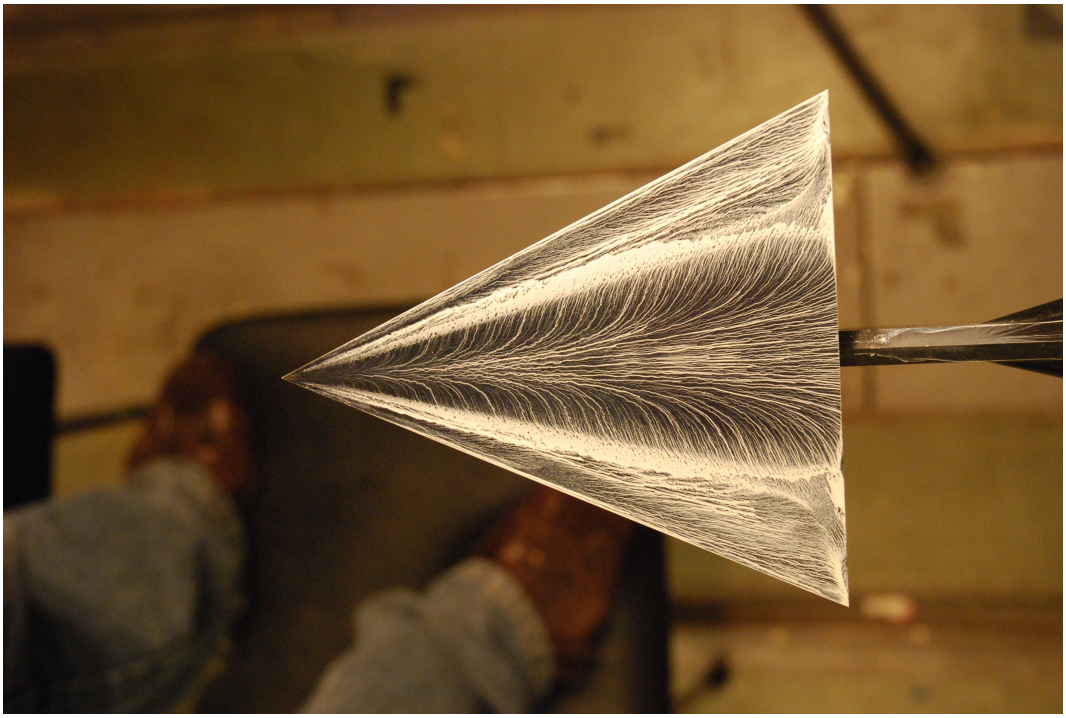

Figure 5.15: Oil flow for $\alpha = 18°$ and $M_\infty = 2.0$.

5.3 Particle tracer distribution

Since the tracer particles have a higher inertia compared to the surrounding flow, they will slip in regions of high flow accelerations. The amount of slip is determined by the particle relaxation time and depends on the particle characteristics as density and size. It manifests itself by introducing a slip velocity (the particle lags the flow field) and drift from the fluid path.

To determine the particle relaxion time, a shock test as described by Schrijer [22] is performed by measuring the response to an oblique shock from a 8° wedge, see figure 5.16(a). By plotting the measured velocity on a semilogarithmic scale and measuring the slope, a corresponding relaxation time of approximately 2.1 μs is extracted. With equation 5.1 from Melling [15]

$$d_p = \sqrt{\frac{18\mu_f \tau_p}{\rho_p}} \tag{5.1}$$

this corresponds to a particle size of 0.7 μm. The median particle size given by the specifications of the seeder [3] is approximately 1 μm. Since an additional impactor plate is installed the expected median particle size should be slightly smaller, so the particle size of 0.7 μm seems correct.

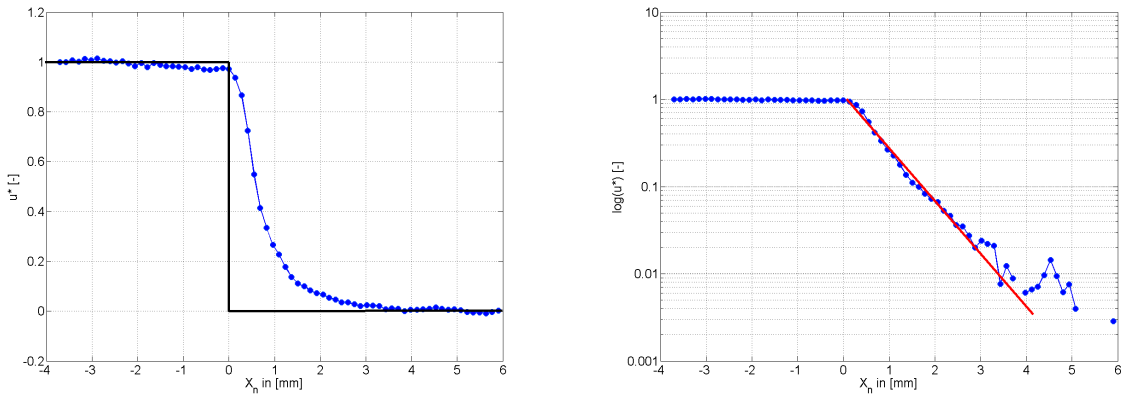

(a) Response to an oblique shock

(b) Response on a semi-logarithmic scale.

Figure 5.16: Particle response diagrams to an oblique shock (From D. Ragni).

Because of the drift, the particles are ejected out of the vortex resulting in an empty core, see figure 5.17 and 5.18. This prevents any reliable measurement in this region due to lack of seeding. The empty vortex core looks stretched because it is a cross section of the vortex in almost longitudinal direction, making circular patterns appear elliptical. For a circular vortex, the slip velocity is easily calculated by equation 5.2.

$$V_{slip} = a \cdot \tau = \frac{V_t^2}{r}\tau_p \tag{5.2}$$

The deviation from its circular path is given by integration of the slip velocity over time. From the measurements a motion of maximum 1/2 revolution around the vortex core is detected. The time it takes to perform 1/2 revolution depends on the tangential velocity and the radius, see equation 5.3, resulting in the relation given in equation 5.4.

$$\Delta t_{1/2rev} = \frac{\pi r}{V_t} \tag{5.3}$$

$$\Delta r = \int_{t_0}^{t_1} \frac{V_t^2 \tau_p}{r} dt = \left[\frac{V_t^2 \tau_p t}{r} \right]_{t=0}^{t=\frac{\pi r}{V_t}} = V_t \tau_p \pi \tag{5.4}$$

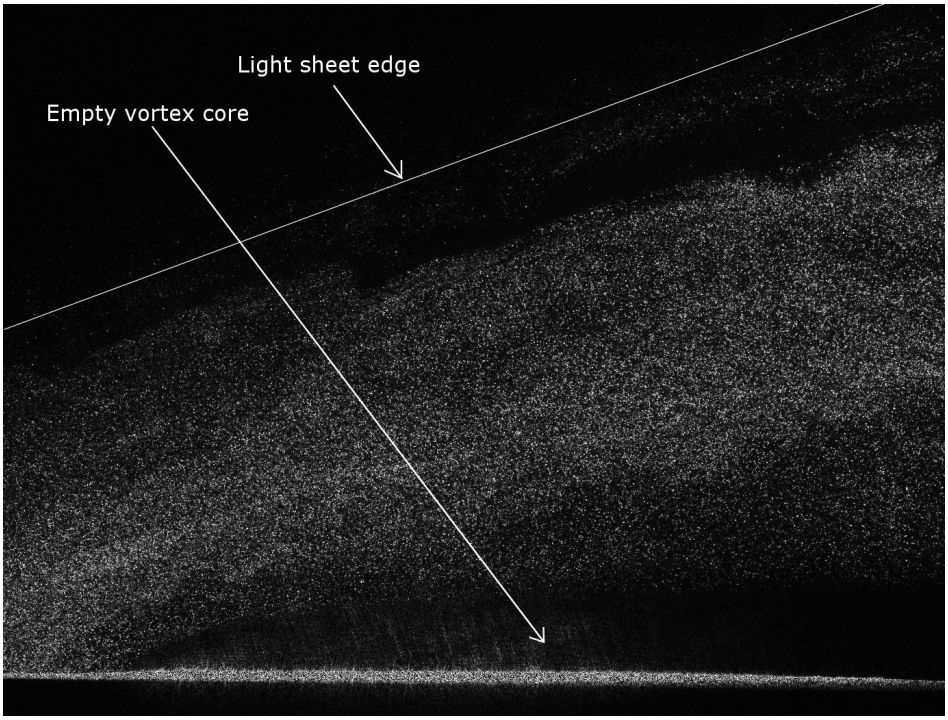

Figure 5.17: An example of a raw PIV image.

Particles are present from approximately 5mm from the vortex core, depending on the angle of attack of the delta wing. For $\alpha = 15°$ a measured tangential velocity at this distance is 230 m/s which results in a particle slip velocity of 22 m/s at 5mm from the core, but this decreases rapidly when moving away from the vortex core as can be seen in table 5.1.

vortex core distance	V_t	V_{slip}	Δr
5 mm	230 m/s	22 m/s	1.5 mm
10 mm	200 m/s	8.4 m/s	1.3 mm
20 mm	170 m/s	3.0 m/s	1.1 mm

Table 5.1: Some parameters at different distances from the vortex core. The shift in radial position is based on 1/2 revolution.

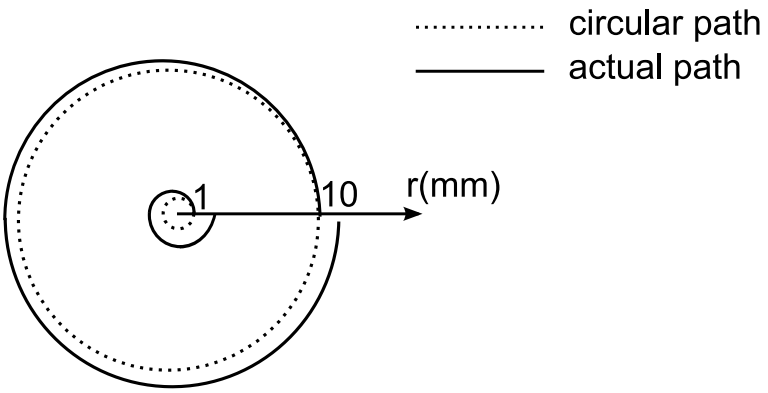

Figure 5.18: Particle deviation due to slip in a circular vortex.

5.4 Freestream flow assesment

Isentropic theory gives the theoretical free stream velocity for a given Mach number and stagnation temperature.

$$V_\infty = M_\infty \sqrt{\frac{2\gamma R T_0}{2 + (\gamma - 1) M_\infty^2}} \tag{5.5}$$

For a stagnation temperature of $285K$ and a free stream Mach number of 1.95 this corresponds to a free stream velocity of $497m/s$. Measurements of the average free stream velocity agree to within $2m/s$ of this value. The turbulence level of the tunnel in freestream direction is approximately 1% ($5m/s$ for $M_\infty = 2.0$). Figure 5.19 shows that the freestream fluctuations are limited to approximately $4m/s$ in streamwise direction. The RMS values for v-component (in wind tunnel coordinates) is approximately $3m/s$ and for the w-component approximately $10m/s$, which is largely due to measurement inaccuracy. According to Prasad [19] the error in the out-of-plane component is approximately 3.5 times as high as for the in-plane component, which is in line with to these measurements. Because of differences of the ambient temperature between runs, the mean velocity can differ up to approximately $4m/s$ per run.

The statistical convergence of the mean and root mean square of the velocity is given by the following functions

$$\bar{u} = \frac{1}{n} \sum_{i=1}^{n} u_i \tag{5.6}$$

$$RMS\,(u) = \sqrt{\frac{1}{n} \sum_{i=1}^{n} (u_i - \bar{u})^2} \tag{5.7}$$

The ensemble size n should be large enough to have at least the mean velocity sufficiently converged. The fluctuations given by the RMS converge slower at a rate of $\sqrt{n}$. The convergence of both values is given in figure 5.19. After approximately 50 samples the mean velocity does not fluctuate a lot anymore. The mean velocity decreases slightly since the stagnation temperature drops approximately 2 K during a run. With an ensemble size of 100 images, the mean velocity is sufficiently converged to avoid large errors.

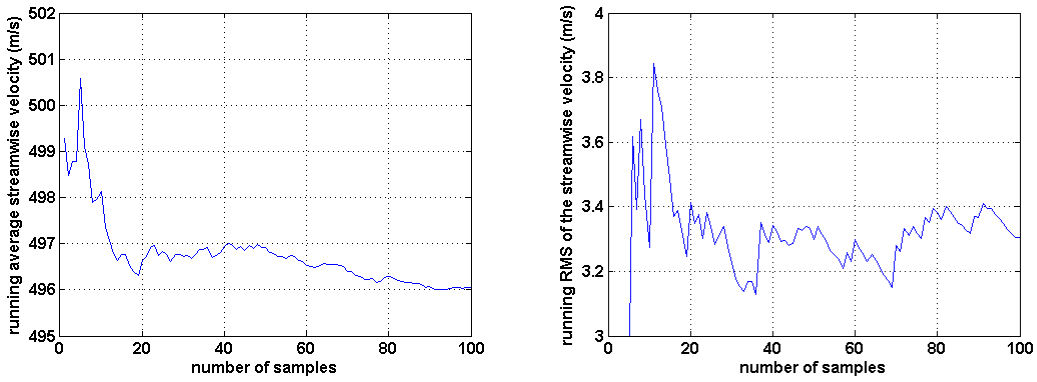

(a) Running average

(b) Running RMS

Figure 5.19: Convergence of the average velocity and RMS with number of image samples.

5.5 Vortex visualisation

A model centered cartesian reference frame is used, denoted by subscript m, with the origin at the apex of the wing, see figure 5.20. This differs from the wind tunnel aligned reference frame, denoted by subscript wt, that it is tilted in the x-y-plane with the angle of incidence α. The velocity components u, v and w are oriented in x_m, y_m and z_m direction respectively. Note that the uniform freestream flow consists of both an u-component and a v-component in this frame, instead of only a u-component in the wind tunnel aligned frame.

The primary vortex is characterised by a circular motion above the wing with a certain side slip angle and angle of incidence with respect to the wing midsection. Because the light sheet is in streamwise direction, the vortex looks elliptical. It can be visualised by plotting the w-component or the v-component. Unfortunately because of lack of seeding no reliable measurements could be taken in the region of outboard motion. Therefore it is more convenient to plot the v-component of the velocity, see figure 5.21, in which a strong upward motion is detected followed by a downward motion more downstream. After combining all the individual measurement planes into a volume, the vortex can be visualised much clearer by a plane normal to the flow direction, see figure 5.22.

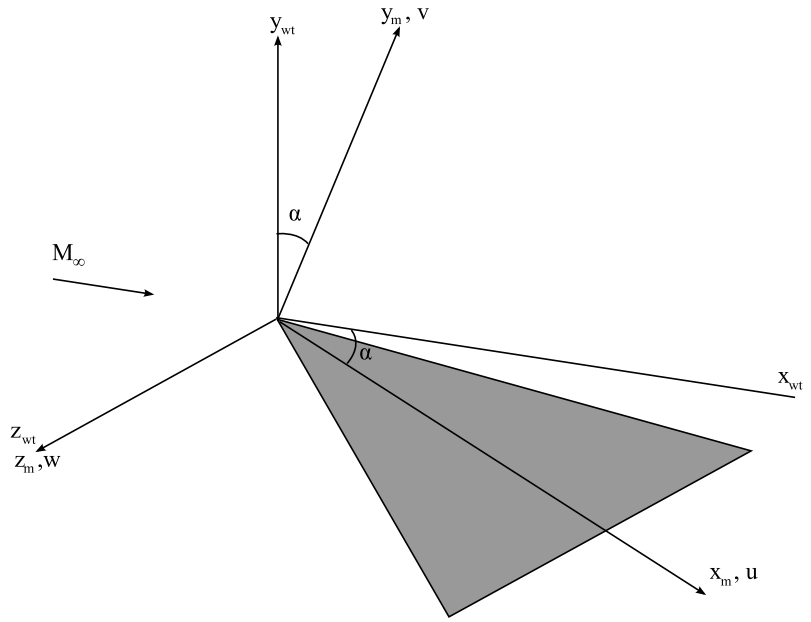

(a)

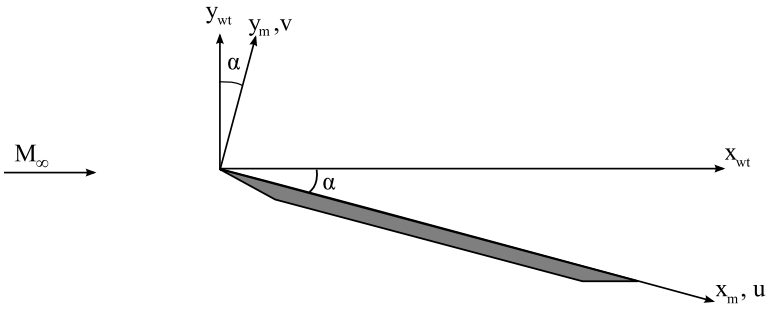

(b)

Figure 5.20: Illustration of the model fixed cartesian coordinate system m and wind tunnel coordinate system wt.

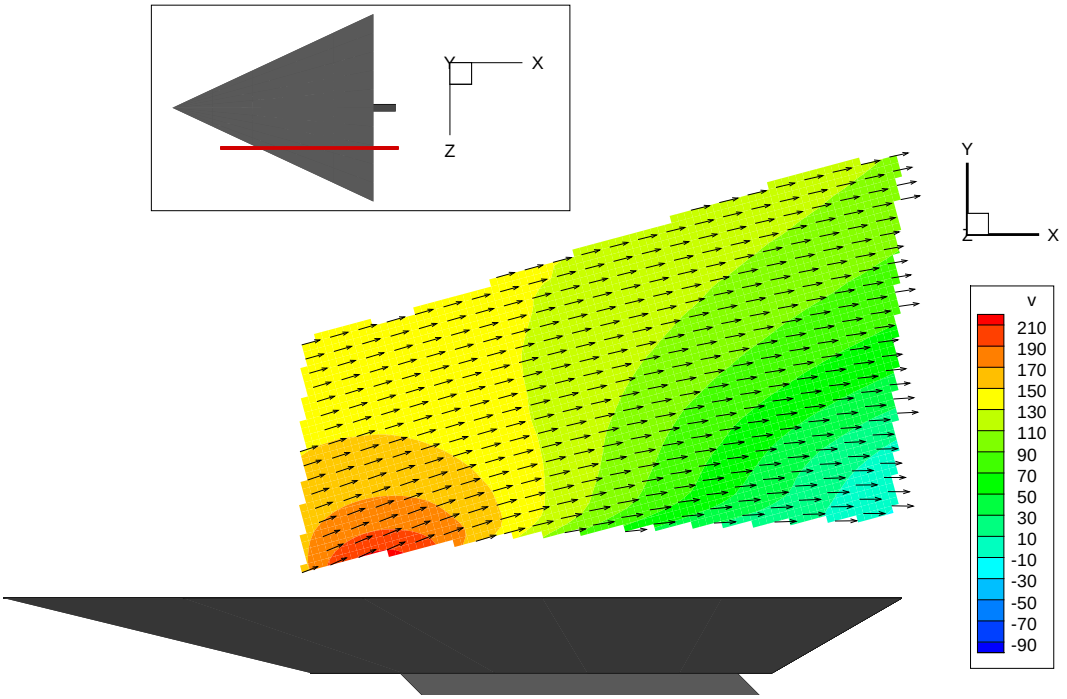

Figure 5.21: V-component of the velocity (m/s) at 24mm from the midsection for $\alpha = 15°$ at $M_\infty = 2.0$.

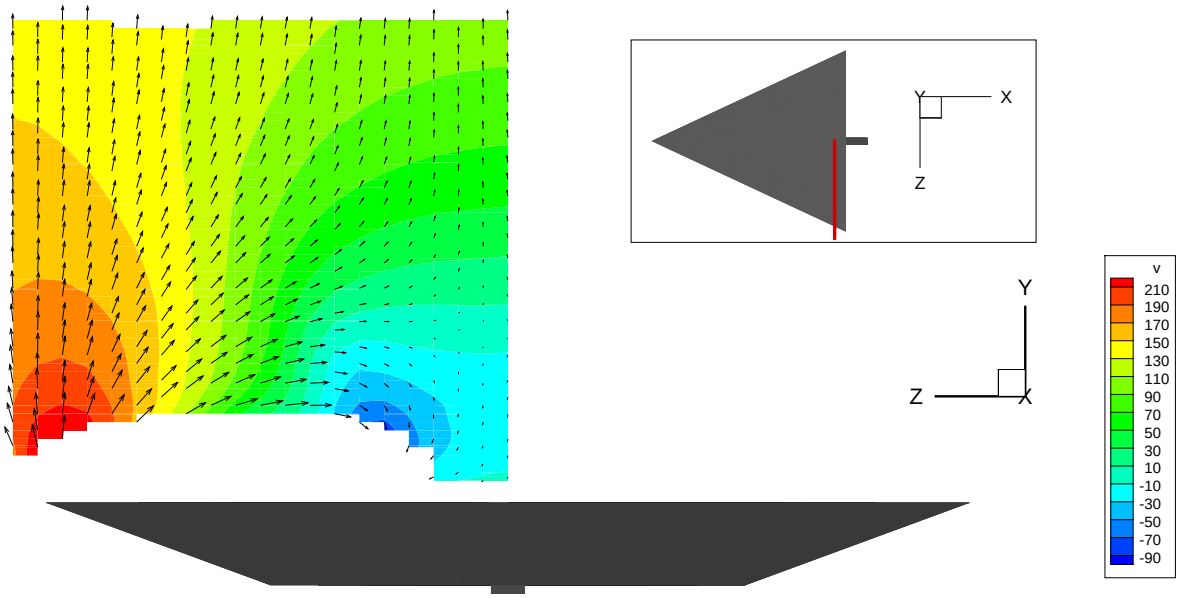

Figure 5.22: V-component of the velocity (m/s) at 113mm from the apex for $\alpha = 15°$ at $M_\infty = 2.0$.

Except for the obvious rotational velocity in the yz-plane also an increased streamwise component of the velocity is detected. This is shown in figure 5.23. The maximum u-component of the velocity measured is approximately 580 m/s.

The slip velocity depends quadratically on the tangential velocity and it the latter a good measure to see how strong the vortex is. Because the vortex core path is unknown the exact tangential velocity is impossible to calculate, but the velocity normal to the freestream gives an accurate estimate and is calculated by the following relation

$$V_t = \sqrt{v^2 + w^2} \tag{5.8}$$

which is plotted in figures 5.24 to 5.27. With increasing angle of attack, V_t increases, and correspondingly the acceleration increases making the region without particles larger. The shape of this region is similar to the vapour screen measurements from literature [12].

Although the vortex core itself is not measured, it is possible to retrieve an approximation of its side slip angle by plotting iso-contours of the vertical velocity, see figures 5.28 to 5.31.

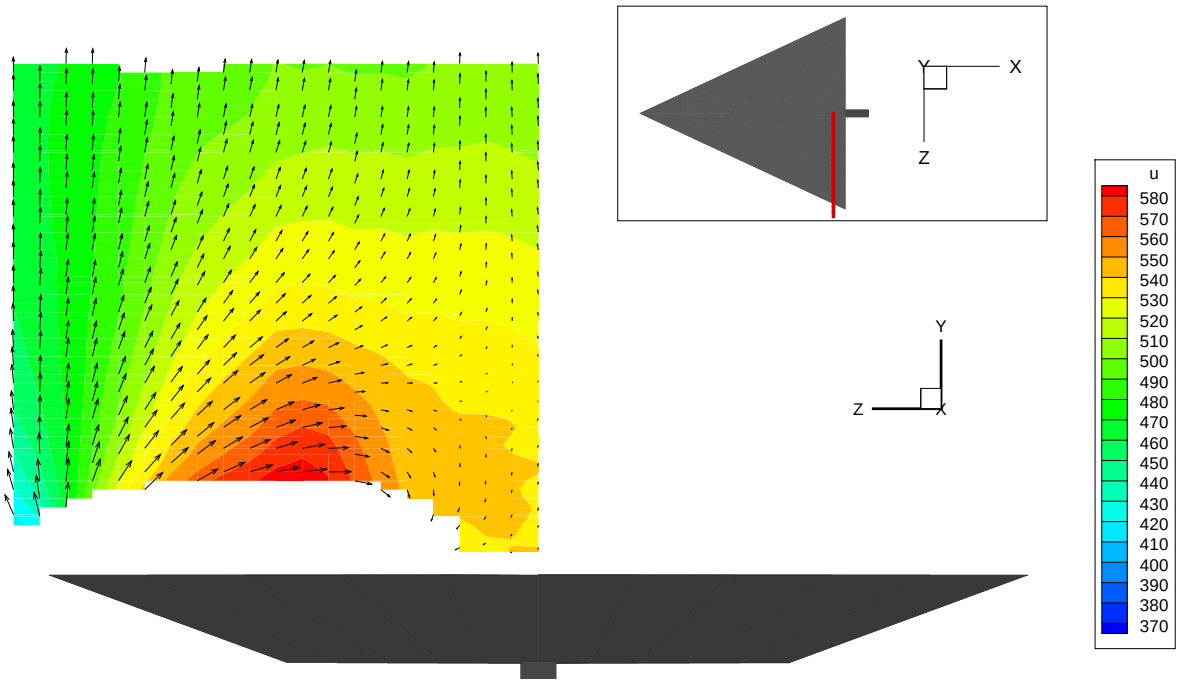

Figure 5.23: U-component of the velocity (m/s) at 113mm from the apex for $\alpha = 15°$ at $M_\infty = 2.0$.

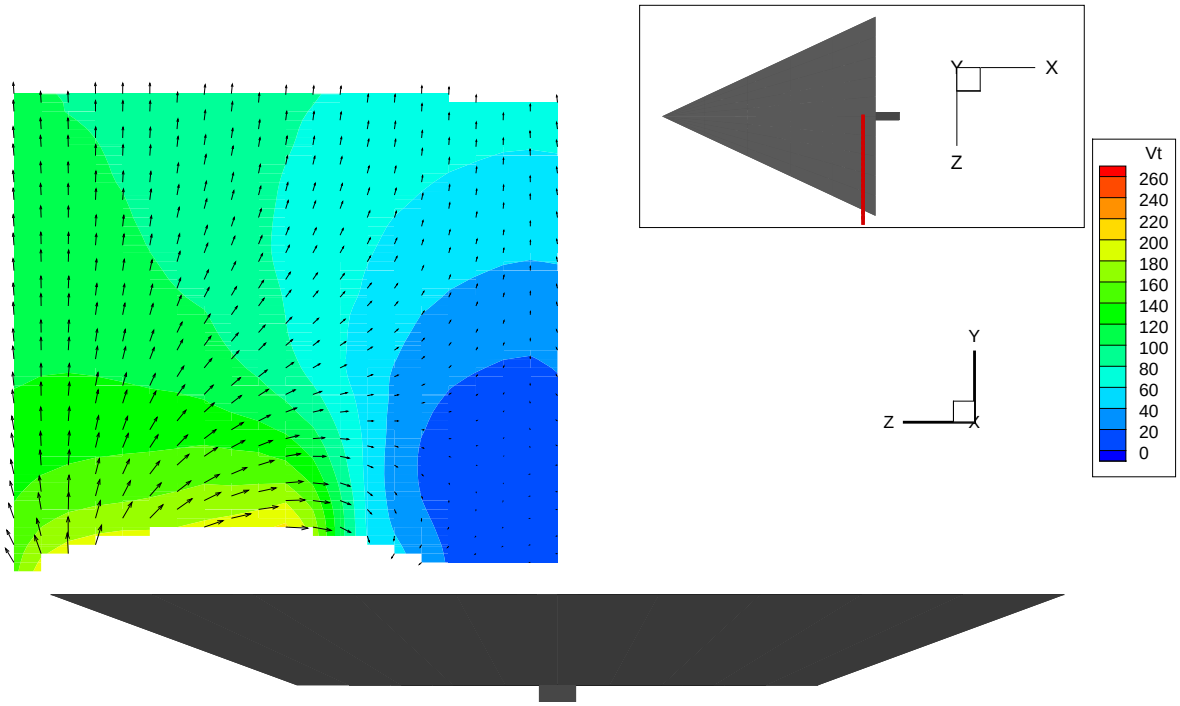

Figure 5.24: Tangential velocity (m/s) at 113mm from the apex for $\alpha = 10°$ at $M_\infty = 2.0$.

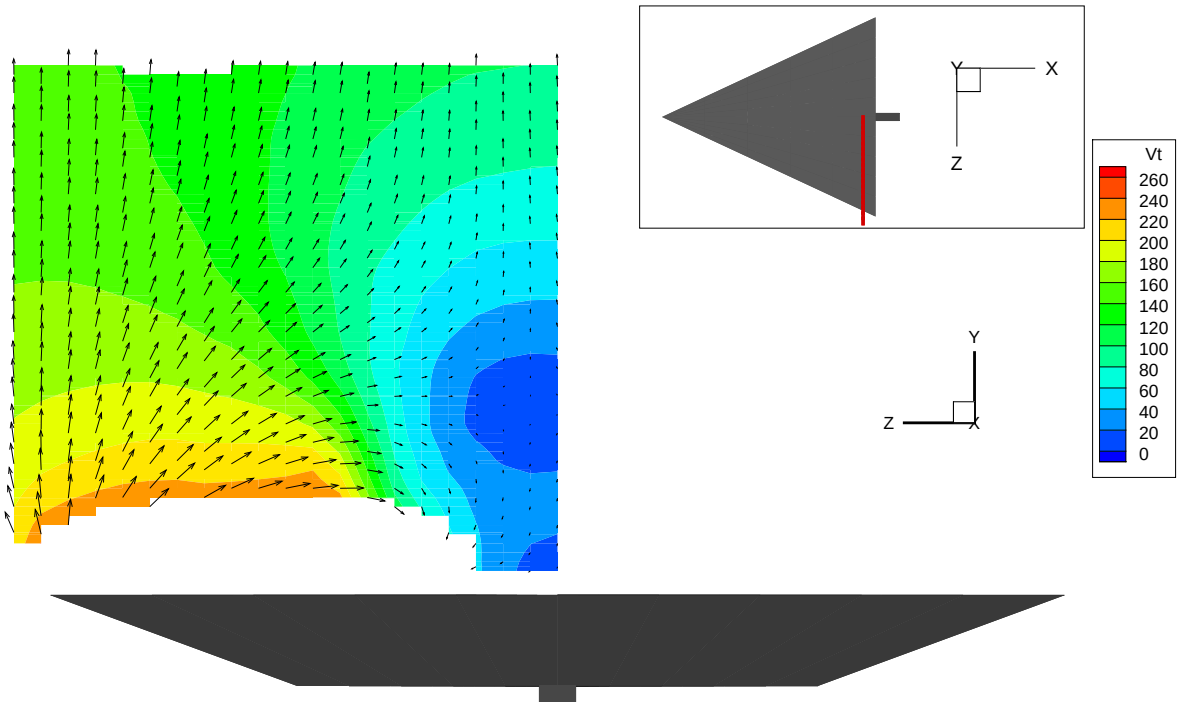

Figure 5.25: Tangential velocity (m/s) at 113mm from the apex for $\alpha = 15°$ at $M_\infty = 2.0$.

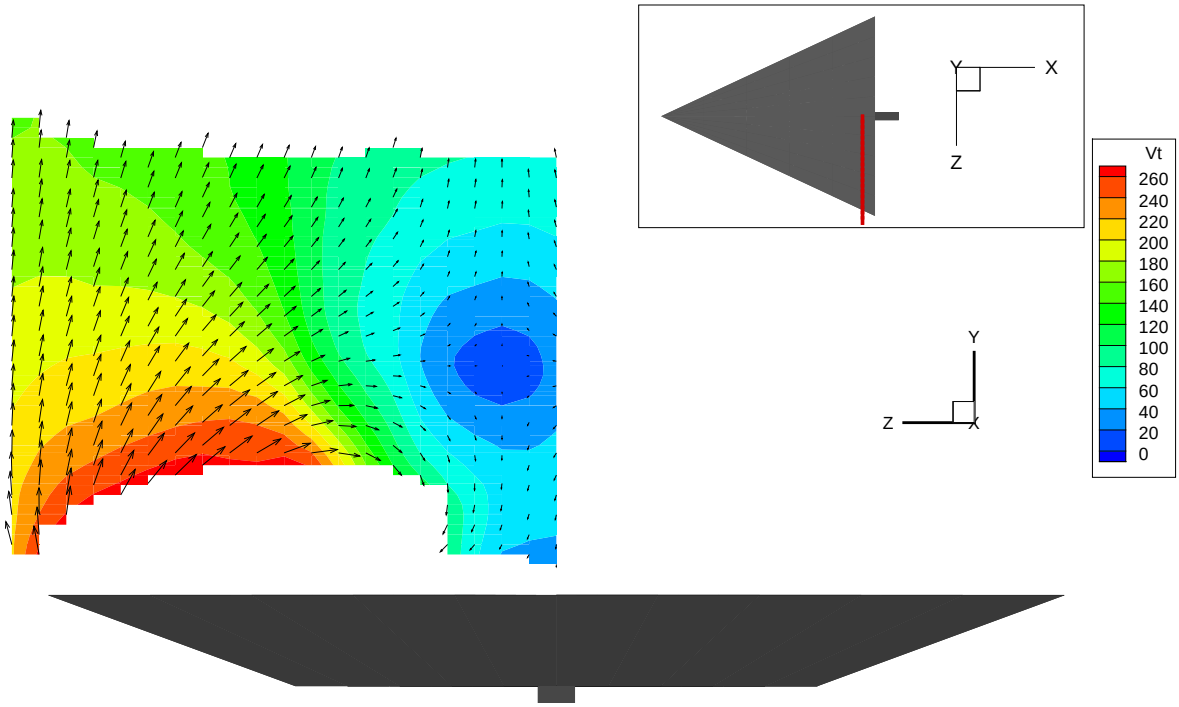

Figure 5.26: Tangential velocity (m/s) at 113mm from the apex for $\alpha = 18°$ at $M_\infty = 1.7$.

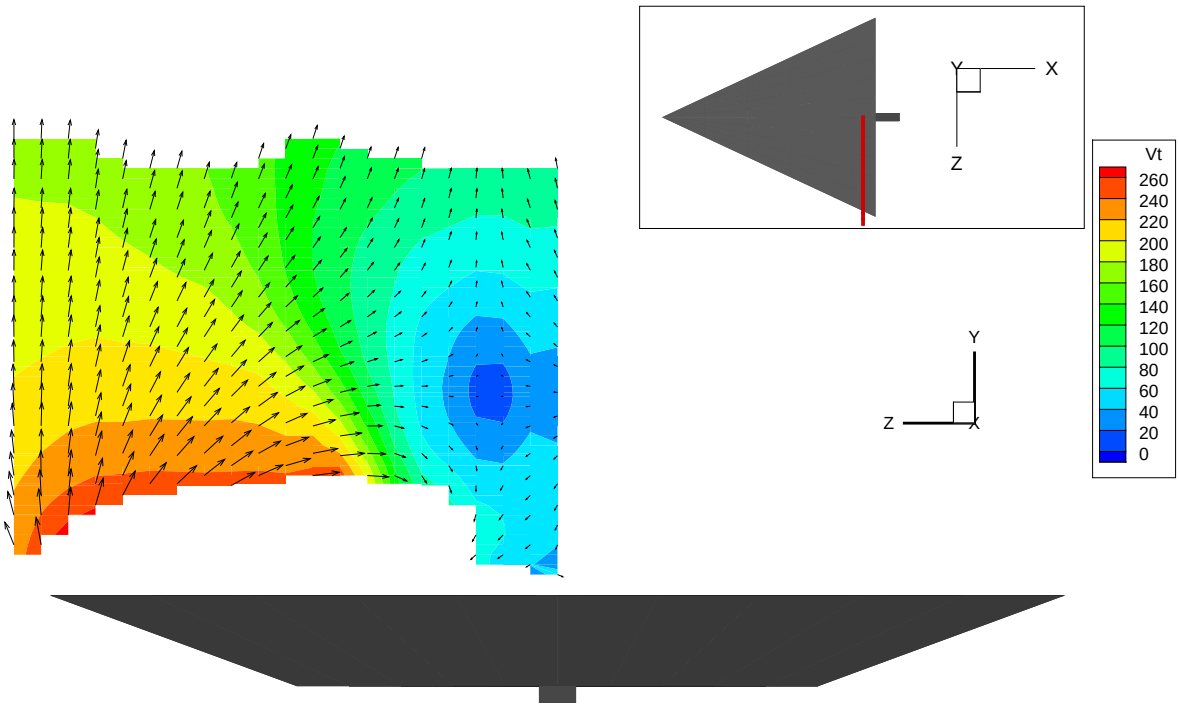

Figure 5.27: Tangential velocity (m/s) at 113mm from the apex for $\alpha = 18°$ at $M_\infty = 2.0$.

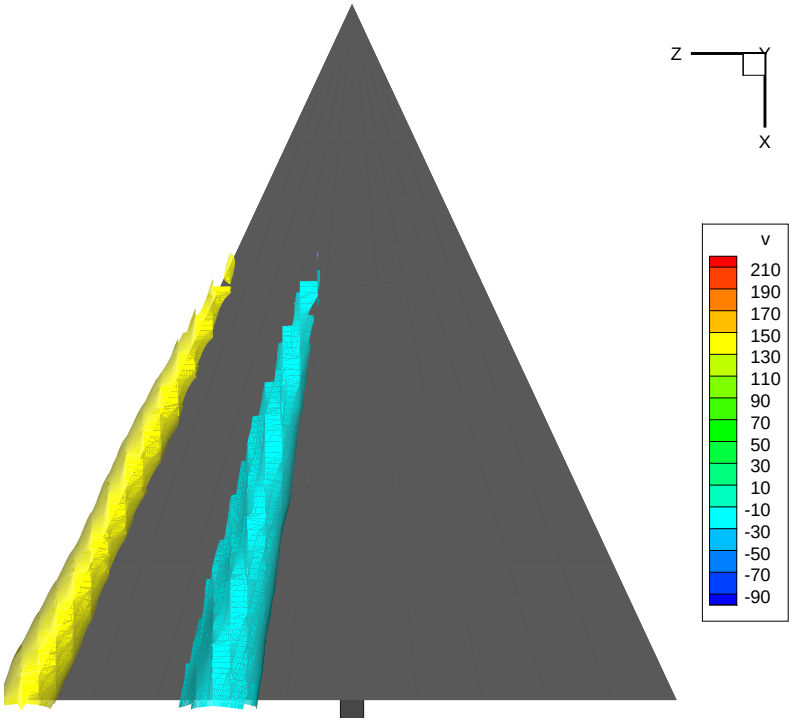

Figure 5.28: Top view of the iso-contours of v = 150 m/s and v = -25 m/s for $\alpha = 10°$ at $M_\infty = 2.0$.

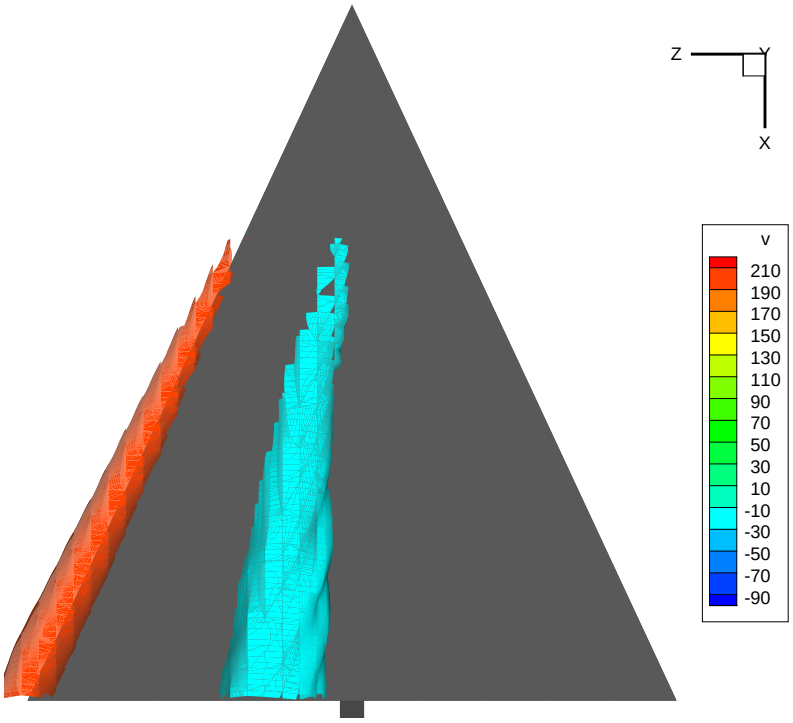

Figure 5.29: Top view of the iso-contours of v = 200 m/s and v = -25 m/s for $\alpha = 15°$ at $M_\infty = 2.0$.

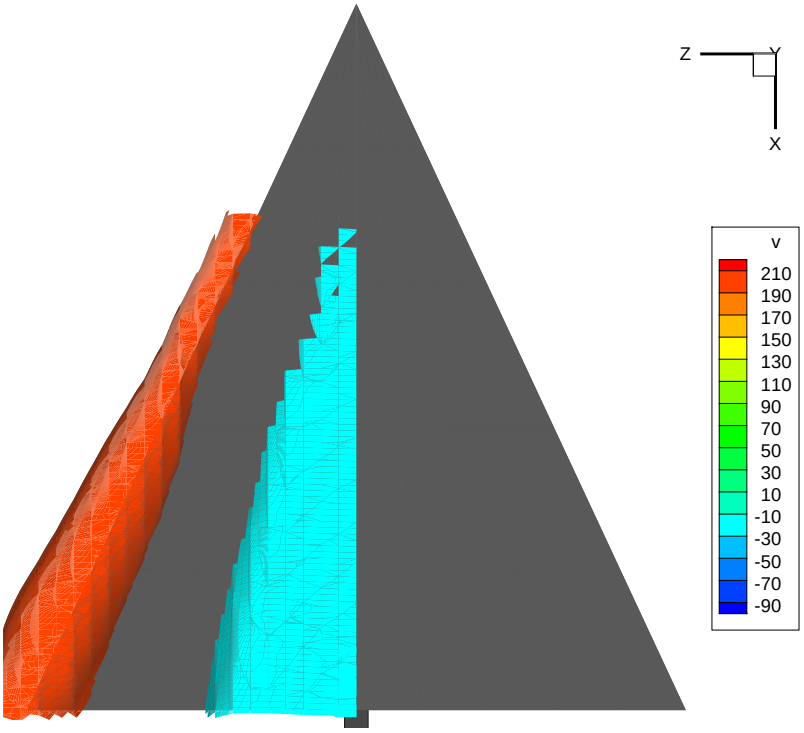

Figure 5.30: Top view of the iso-contours of v = 200 m/s and v = -25 m/s for $\alpha = 18°$ at $M_\infty = 1.7$.

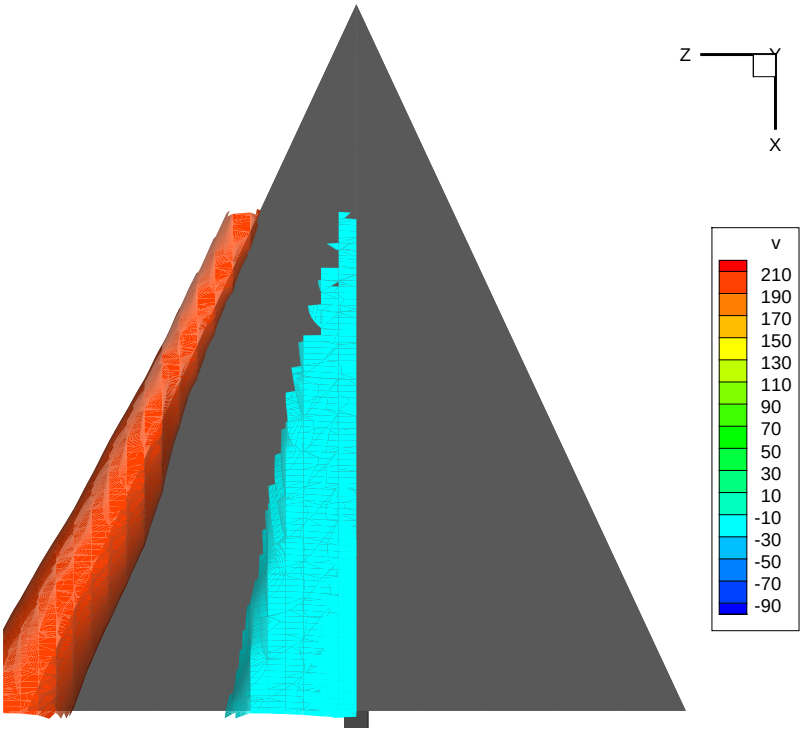

Figure 5.31: Top view of the iso-contours of v = 200 m/s and v = -25 m/s for $\alpha = 18°$ at $M_\infty = 2.0$.

5.6 Shocks

5.6.1 Leading edge shock

Looking at a plot of the w-component, except for the inboard motion of the vortex, also an outboard motion is apparent just before the leading edge, see figure 5.33. Also a slight decrease in the u-component is present in this area, see figure 5.34. This indicates that a conical shock is present just before the leading edge of the wing decelerating the flow in the direction normal to the shock. Since the flow on the windward surface has to be deflected over a large angle, consisting of the normal angle of attack in addition to the bevel angle ($\alpha_N + \theta$), this shock is always detached in this investigation, even for an infinite Mach number. For small deflection angles with a smaller bevel angle and high normal Mach numbers there is the possibility of an attached shock because the deflection angle is lower than the maximum deflection angle for cones, e.g. in the study of Bannink [5], but in practical situations of delta wings this will not be the case. The expansion on the leeward surface will weaken this shock, but an entropy gradient remains present in the flow field.

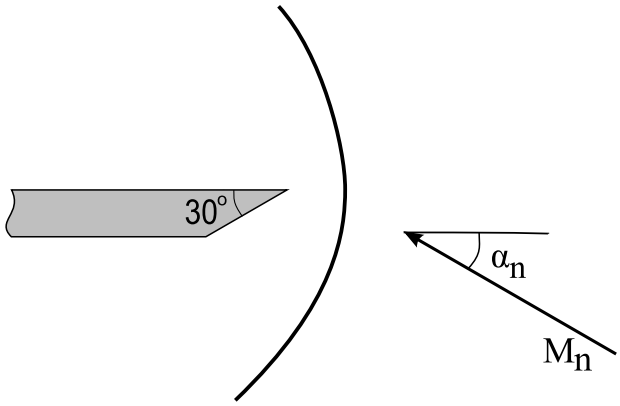

Figure 5.32: Schematic overview of the leading edge shock.

The divergence of the velocity indicates compression and expansion areas in the flowfield. From conservation of mass the relation between the divergence of the velocity and the density gradient is given by

$$\nabla \cdot \vec{V} = -\vec{V} \cdot \frac{\nabla \rho}{\rho} \tag{5.9}$$

So in areas of compression the divergence is negative and in expansions the divergence is positive. As can be seen from figures 5.35 to 5.38 indeed a region of negative divergence is present before the leading edge, indicating the shock. The shock strength increases with increasing angle of attack. For the run at $\alpha = 18°$ and $M_\infty = 1.7$ the shock angle from the apex is higher, resulting in a shock position further away from the wing.

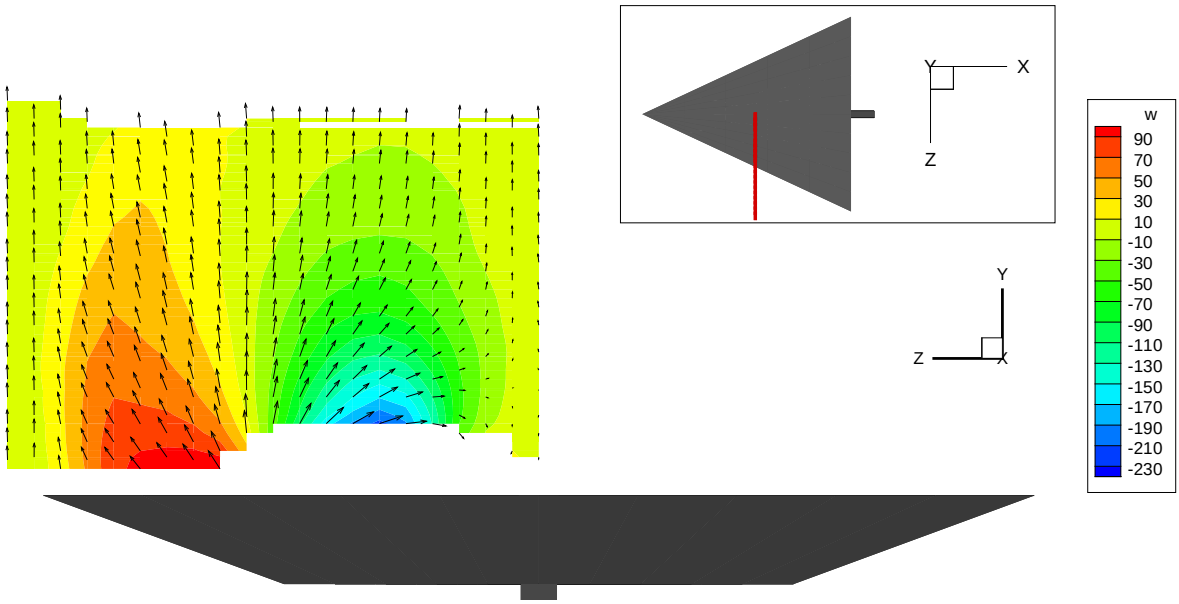

Figure 5.33: W-component of the velocity (m/s) at 65mm from the apex for $\alpha = 15°$ at $M_\infty = 2.0$.

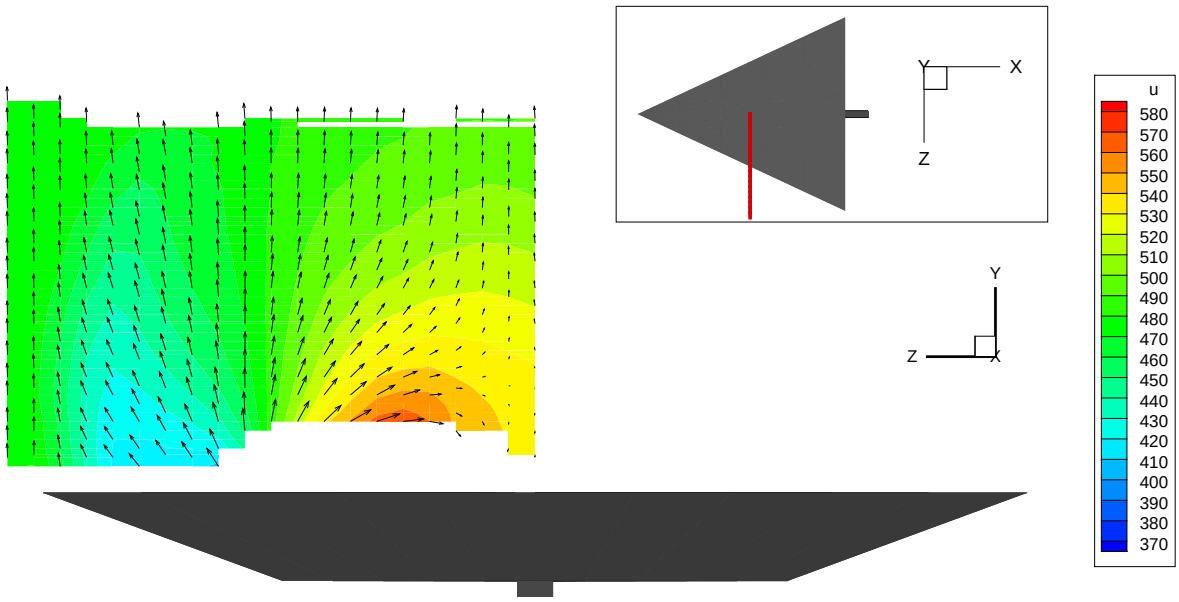

Figure 5.34: U-component of the velocity (m/s) at 65mm from the apex for $\alpha = 15°$ at $M_\infty = 2.0$.

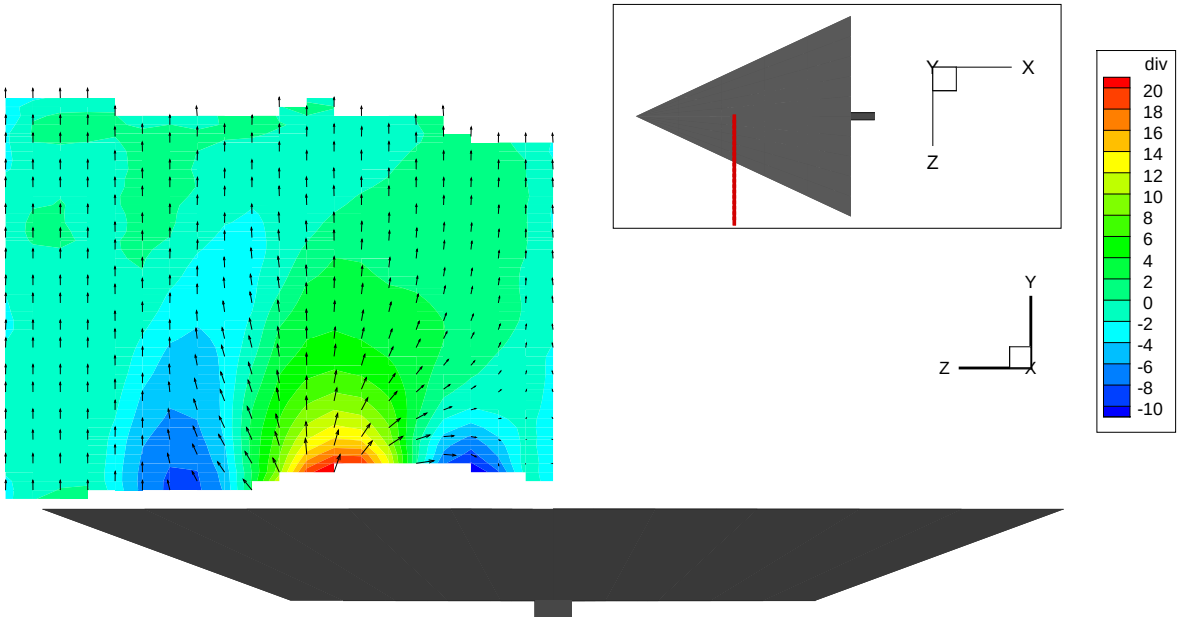

Figure 5.35: Divergence of the velocity (1/s) at 55mm from the apex for $\alpha = 10°$ at $M_\infty = 2.0$.

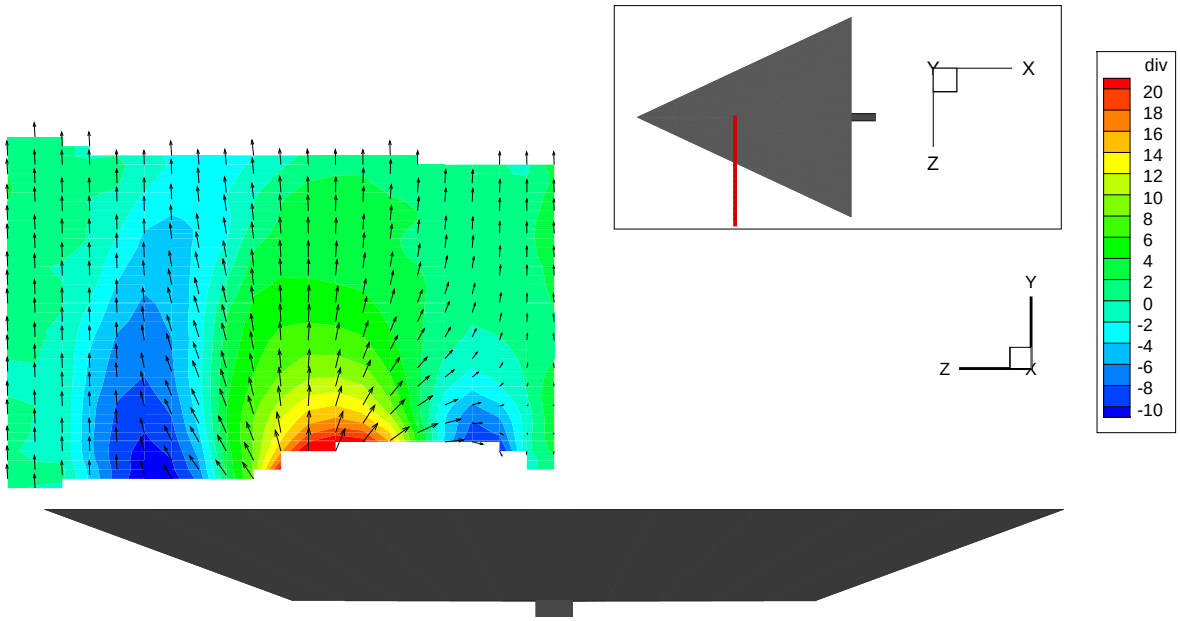

Figure 5.36: Divergence of the velocity (1/s) at 55mm from the apex for $\alpha = 15°$ at $M_\infty = 2.0$.

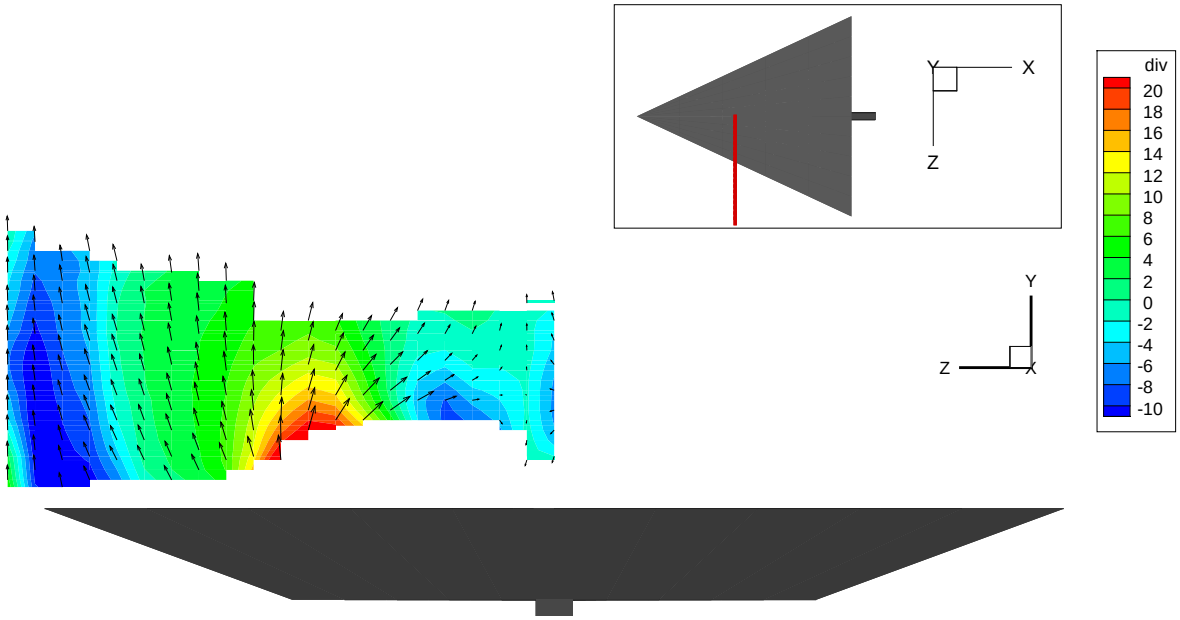

Figure 5.37: Divergence of the velocity (1/s) at 55mm from the apex for $\alpha = 18°$ at $M_\infty = 1.7$.

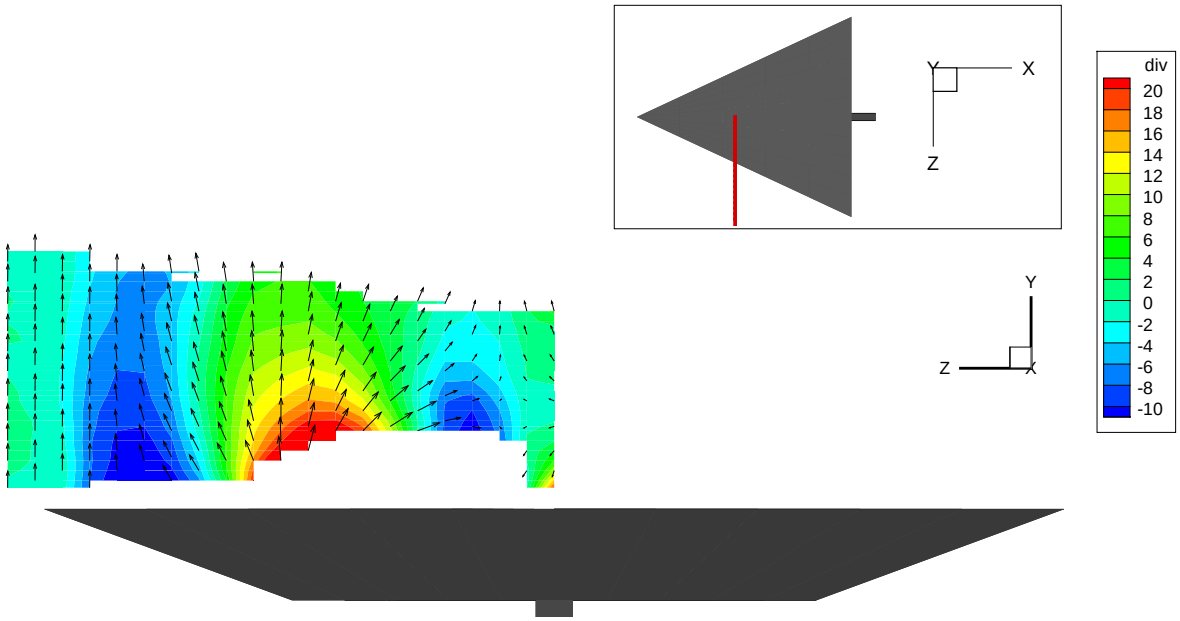

Figure 5.38: Divergence of the velocity (1/s) at 55mm from the apex for $\alpha = 18°$ at $M_\infty = 2.0$.

5.6.2 Inboard shockwave

Apart from the leading edge shock, also an inboard compression region is visible, as was expected from the diagram from Miller and Wood (figure 2.12). The shock is attached to the vortex, as depicted in figure 5.39. For $\alpha = 10°$ the compression area is more or less circular, see figure 5.35. Increasing the angle of attack shapes the shock in the characteristic curved shape, determined by vapour screen visualisation [16], and it also becomes stronger. The position of the shock remains approximately constant.

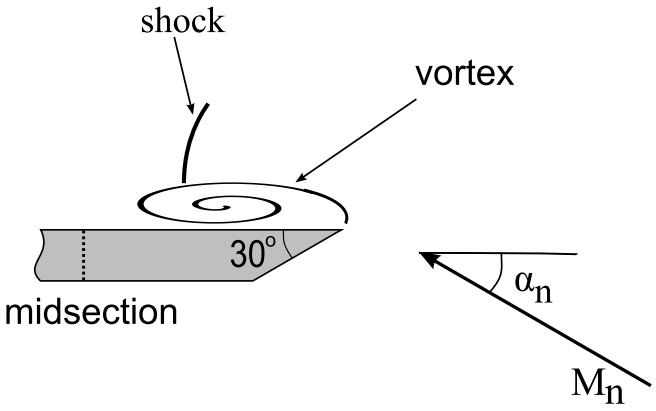

Figure 5.39: Schematic overview of the inboard shock attached to the primary vortex.

When looking at the top view of the iso-contour, the path the expansion and both shocks follow is clearly visible and appears to be conical, see figures 5.40 to 5.43.

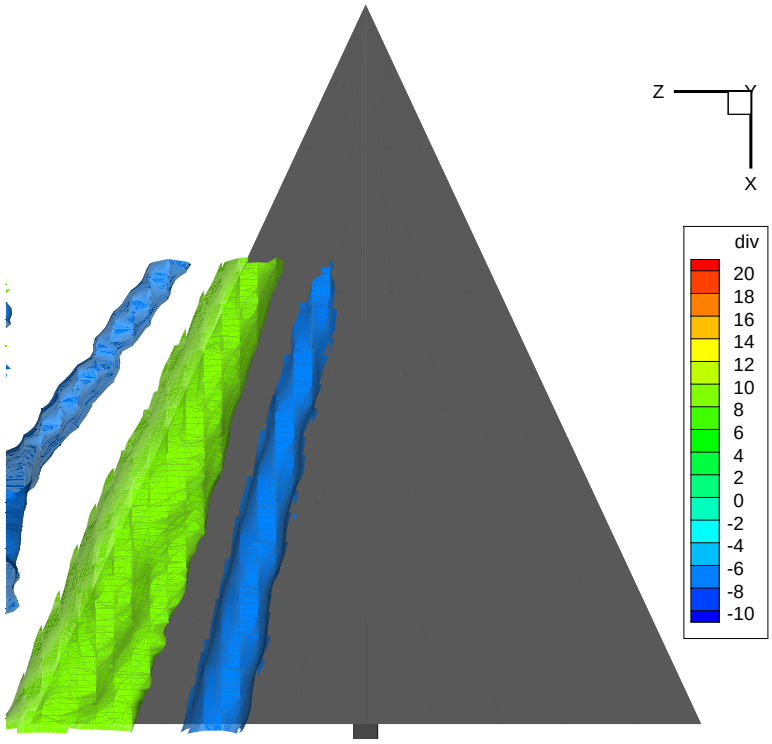

Figure 5.40: Top view of the iso-contours of $(\nabla \cdot V) = -5s^{-1}$ and $(\nabla \cdot V) = 10s^{-1}$ at $\alpha = 10°$ and $M_\infty = 2.0$.

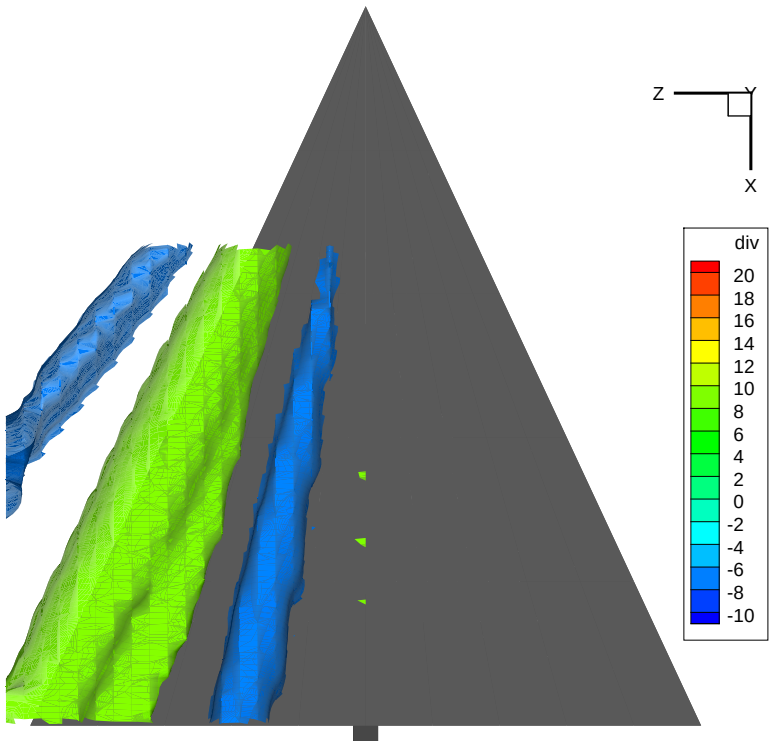

Figure 5.41: Top view of the iso-contours of $(\nabla \cdot V) = -5s^{-1}$ and $(\nabla \cdot V) = 10s^{-1}$ at $\alpha = 15°$ and $M_\infty = 2.0$.

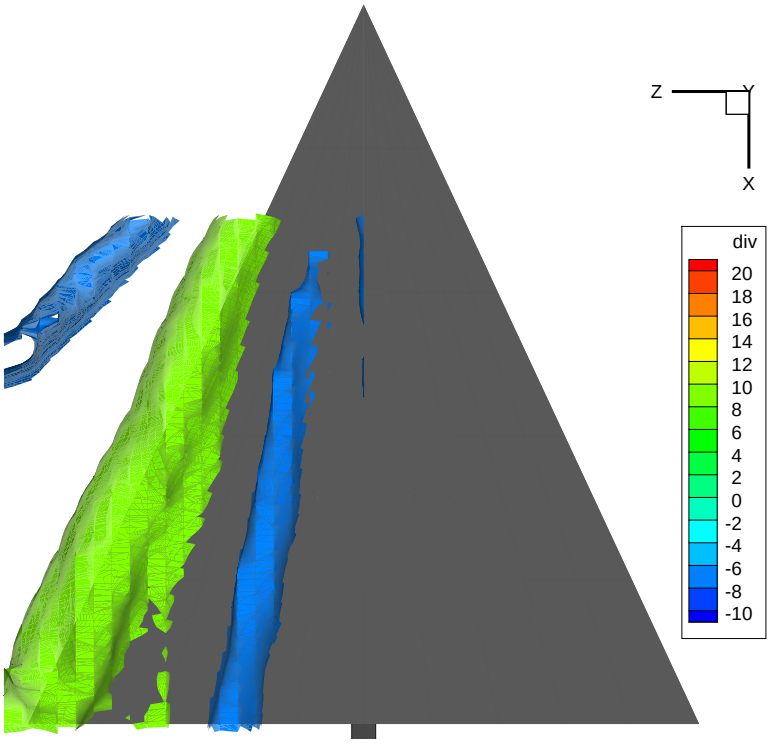

Figure 5.42: Top view of the iso-contours of $(\nabla \cdot V) = -5s^{-1}$ and $(\nabla \cdot V) = 10s^{-1}$ at $\alpha = 18°$ and $M_\infty = 1.7$.

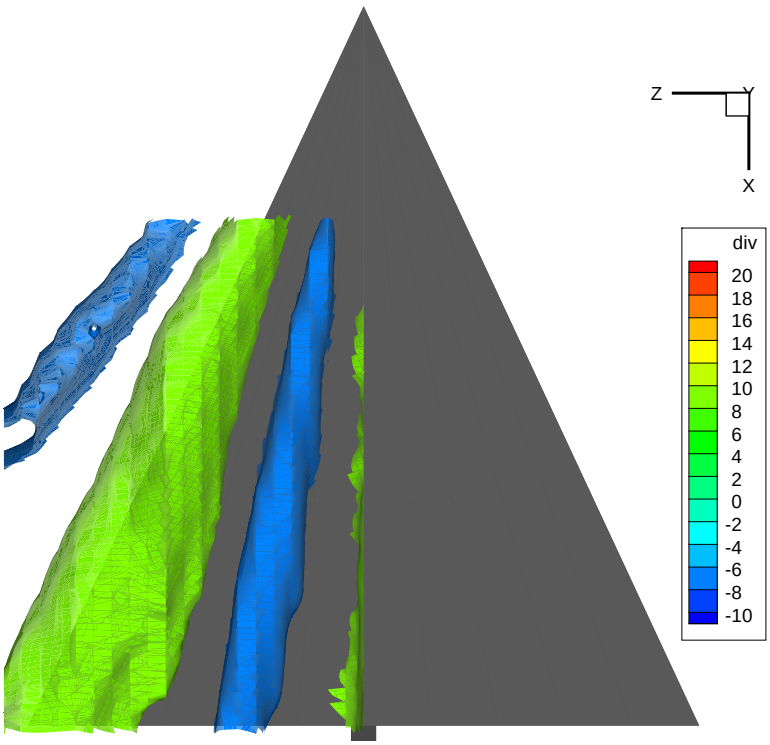

Figure 5.43: Top view of the iso-contours of $(\nabla \cdot V) = -5s^{-1}$ and $(\nabla \cdot V) = 10s^{-1}$ at $\alpha = 18°$ and $M_\infty = 2.0$.

5.7 Conical flow

From the results of the measurements, the flow field appears to be conical, i.e. the flow quantities are constant along rays emerging from the apex, and a transformation from Cartesian coordinates into conical coordinates is useful. The coordinates are shown in figure 5.44 and the transformation is done by applying the following equations

$$x = r\cos\theta \tag{5.10}$$
$$y = r\sin\theta\cos\phi \tag{5.11}$$
$$z = r\sin\theta\sin\phi \tag{5.12}$$

and the velocity components are consequently rewritten by

$$u = V_r\cos\theta - V_\theta\sin\theta \tag{5.13}$$
$$v = V_r\sin\theta\cos\phi + V_\theta\cos\theta\cos\phi - V_\phi\sin\phi \tag{5.14}$$
$$w = V_r\sin\theta\sin\phi + V_\theta\cos\theta\sin\phi + V_\phi\cos\phi \tag{5.15}$$

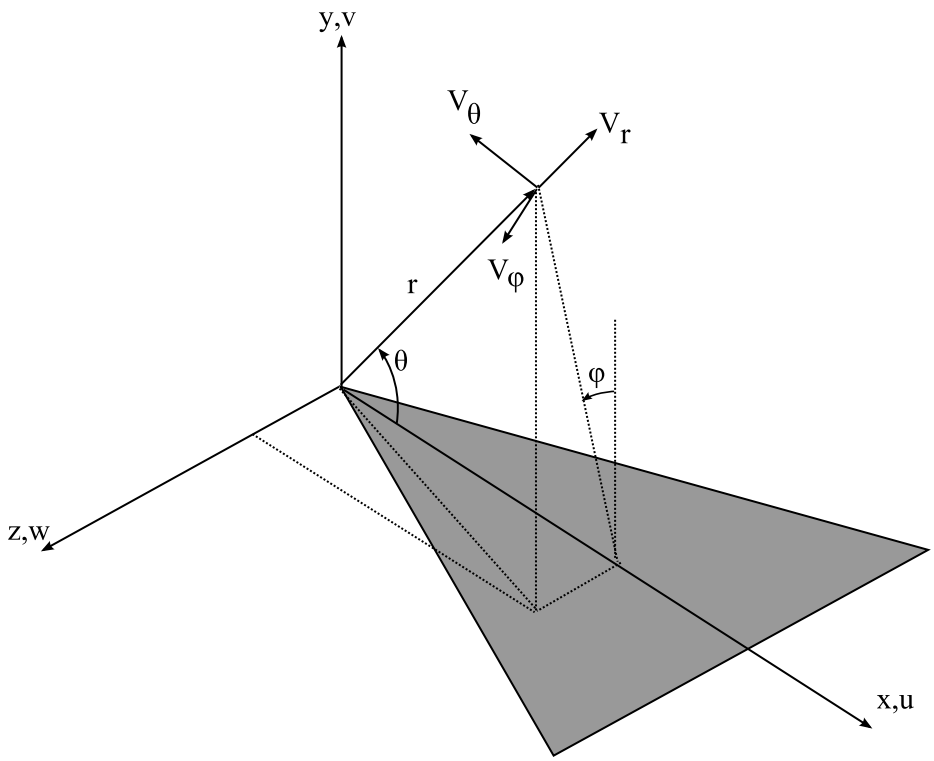

Figure 5.44: Transformation from Cartesian to conical coordinates.

It is the conical Mach number that determines the character of the conical flow equations. The conical velocity is the velocity normal to a ray emerging from the apex and is calculated by the following relation

$$V_c = \sqrt{V_\phi^2 + V_\theta^2} \tag{5.16}$$

It can also be done directly from the cartesian velocity components u, v and w and subsequently applying the following relation

$$V_c = \frac{\sqrt{(vz - wy)^2 + (wx - uz)^2 + (uy - vx)^2}}{\sqrt{x^2 + y^2 + z^2}} \tag{5.17}$$

which gives the same results as using the previous equations.
To calculate the Mach number the local speed of sound is necessary. This can be determined by using the energy equation in the following form

$$a = \sqrt{a_0^2 - \frac{\gamma - 1}{2} V_{tot}^2} \tag{5.18}$$

from which the local Mach number is calculated.

Conical streamlines are defined as lines on the unit sphere in which every point has the same direction as the conical velocity vector in this point. The slope of the streamlines is given by the angle ψ, which is the angle with the positive ϕ-axis. This is calculated according to

$$\tan\psi = \frac{(uy - vx)}{(uz - wx)} \tag{5.19}$$

Since the flow field only depends on ϕ and θ, the measurements can be averaged over multiple r-stations. For a better physical interpretation the results are plotted in projections of the conical flow on normalised coordinates $\frac{y}{x}$ and $\frac{z}{x}$, shown in figure 5.45 to 5.48. The leading edge of the wing has a sweep angle of 65° corresponding to $\frac{z}{x} = 0.46$. The plots clearly show the presence of a vortex above the wing, raising the local conical Mach number significantly up to supersonic values. A strong gradient in Mach number is present around $\frac{z}{x} = 0.8$ for $M_\infty = 2.0$ and at $\frac{z}{x} = 1$ for $M_\infty = 1.7$, corresponding to the leading edge shock wave. Another gradient is present at approximately $\frac{z}{x} = 0.2$, varying slightly between the different conditions, corresponding to the inboard shockwave that is attached to the vortex. A trend of increasing conical Mach number in the vortex is detected with increasing angle of attack, which makes the local supersonic area larger and generates a stronger inboard shock.

A spanwise conical Mach number distribution at $\frac{y}{x} = 0.16$ gives a clear picture of the flow features, see figure 5.50. Outside the leading edge shock the flow is uniform which is seen as a slightly curved line with supersonic conical Mach number. Moving more inboard, the leading edge shock decreases the conical Mach number to subsonic values. Close to the leading edge at $\frac{z}{x} = 0.46$, the flow is accelerated strongly to a supersonic conical Mach number again by the vortex. At around $\frac{z}{x} = 0.2$ the inboard shock decelerates the flow again.

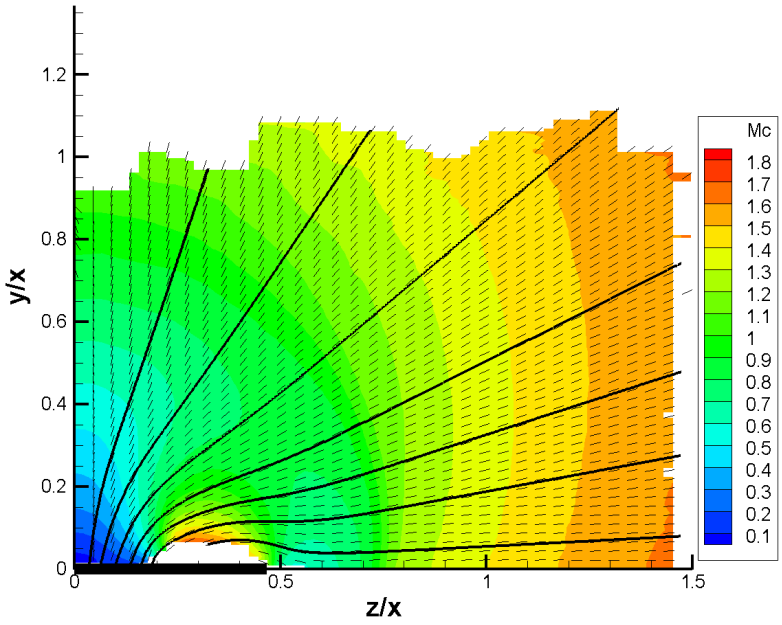

Figure 5.45: Conical Mach number distribution for $\alpha = 10°$ and $M_\infty = 2.0$.

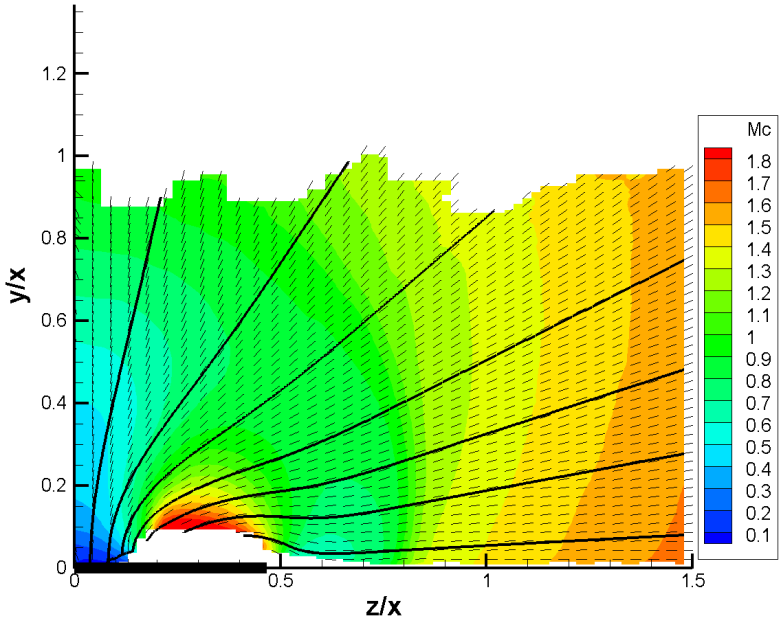

Figure 5.46: Conical Mach number distribution for $\alpha = 15°$ and $M_\infty = 2.0$.

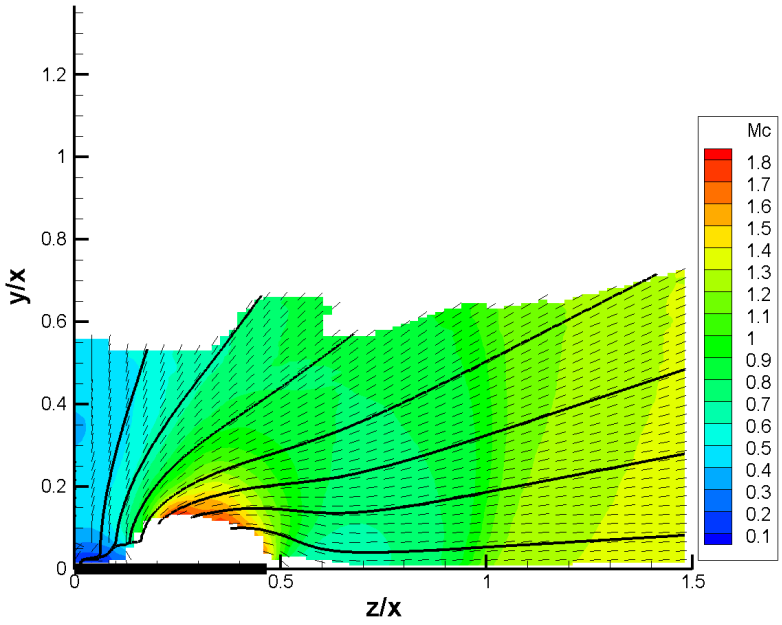

Figure 5.47: Conical Mach number distribution for $\alpha = 18°$ and $M_\infty = 1.7$.

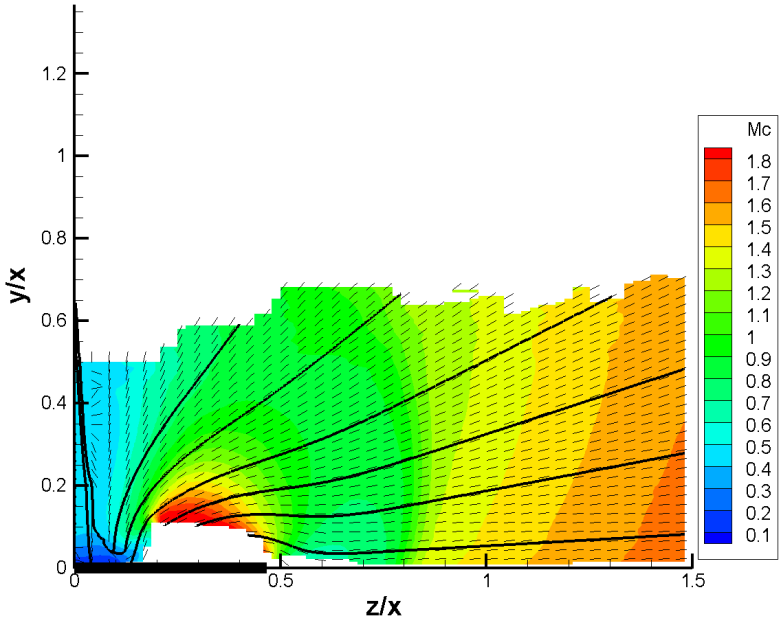

Figure 5.48: Conical Mach number distribution for $\alpha = 18°$ and $M_\infty = 2.0$.

When the contour plots are compared to the Mach number distribution of Bannink [5], which is shown in figure 5.49, many similarities can be found, although the flow conditions are quite different. Bannink measured on a 45.3° delta wing at $\alpha = 12°$ with a freestream Mach number of $M_\infty = 2.94$, which corresponds to $\alpha_N = 16.6°$ and $M_N = 2.1$, in region 4 from the diagram of Miller and Wood (figure 2.12). The conical streamlines show more or less the same direction, except for the fact that no vortex is present anymore. Since at these conditions the shock from the windward surface is attached, it is not present at the leeward side. The inboard shock is attached to the surface at around $\frac{y}{x} = 0.23$, which corresponds to the position found in the current study.

The spanwise distribution of the conical Mach number, shown in figure 5.51, looks rather different than in the current investigation. The normal Mach number is much higher in the study from Bannink. There is no leading edge shock present, since the windward shock is attached. Furthermore there is no vortex present that increases the local conical Mach number. The only agreement is the presence of an inboard shock.

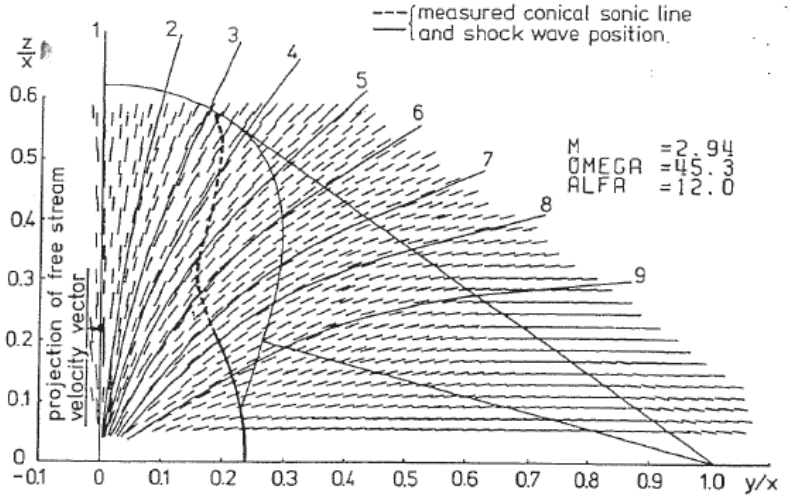

Figure 5.49: Conical Mach number distribution from Bannink [] for $\alpha_N = 16.6°$ and $M_N = 2.1$.

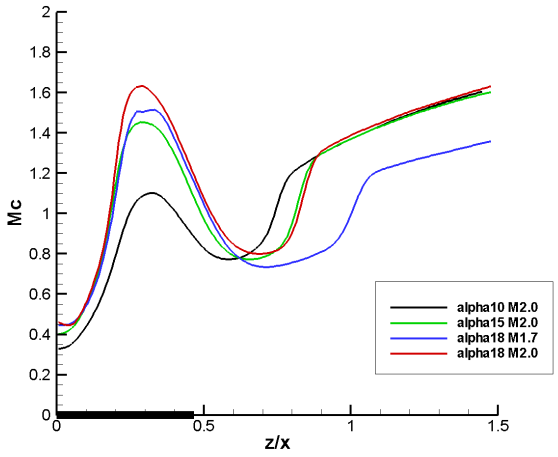

Figure 5.50: Spanwise conical Mach number distribution at $\frac{y}{x} = 0.16$.

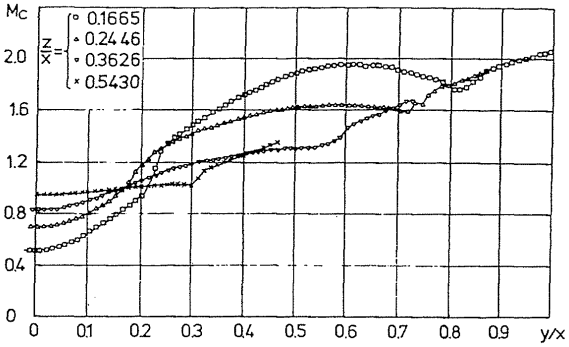

Figure 5.51: Spanwise conical Mach number distribution from Bannink.

5.8 Conclusion

The supersonic flow around a delta wing has been investigated using several different complementary measurement methods. A standard side view Schlieren and shadowgraphy setup was made which was able to show the presence of the primary vortex on the delta wing leeward surface. However it was not able to capture the presence of a shock in the flowfield. This is due to the fact that it is a 2-dimensional technique, and the shocks present on the delta wing are almost perpendicular to the viewing direction. Probably a surface reflective Schlieren setup would have been able to visualise the shocks.

Oil flow visualisation showed the presence of primary and secondary vortices on the leading edge with great precision. Only this technique and shadowgraphy were able to capture the secondary vortex for $M_\infty = 1.7$. However oil flow visualisation was completely unable to find shock waves, since they are not attached to the surface.

Stereoscopic PIV has been the only quantitative method used in this investigation. Because of the high accelerations in the flow field, the tracer particles slip with respect to the flow due to their inertia, resulting in a slip velocity and a deviation from the fluid path.

A shock test is performed to measure the response of the tracer particles to a step input, resulting in a tracer particle relaxation time of 2.1 μs. With this value, the path deviation of the particle and the slip velocity in a circular vortex are calculated. The path deviation, which is linear proportional to the tangential velocity, manifests itself by an empty vortex core, because all particles are ejected preventing reliable measurements in this area. The slip velocity is quadratic proportional to the tangential velocity, introducing errors close to the vortex core.

The freestream velocity is measured correctly and the tunnel produces repeatable flow conditions, allowing a combination of the individual measurement planes into a full 3-dimensional flow field. These results produce a clear visualisation of the top of the primary vortex. Also two different shock waves are found in the flow field. One of them is in front of the leading edge, which is a detached shock wave due to the large deflection of the flow on the windward surface. The other is an inboard shock wave which was expected because the measurements are performed in region 3 of the Miller and Wood classification. A schematic overview of a cross-section of the flow field is given in figure 5.52.

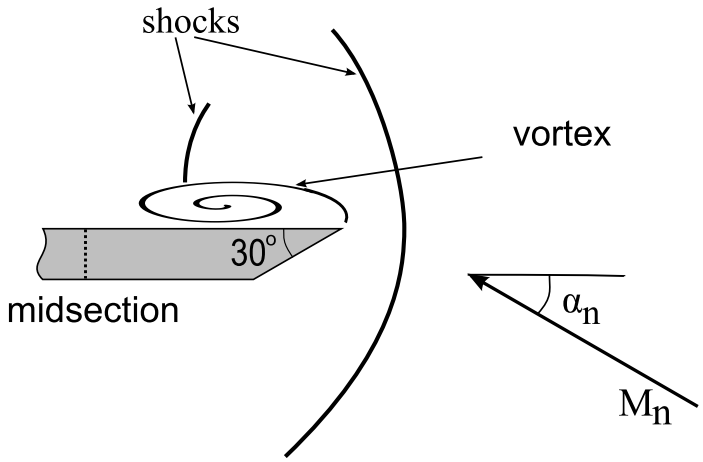

Figure 5.52: Schematic overview of the flow features in a cross-section of the flow field.

The flow field is found to be conical, making it possible to transform from Cartesian coordinates into conical coordinates. Because the flow is depending only on ϕ and θ, this allowed averaging over the different r-stations. In principle from one well-chosen measurement plane, the complete flowfield could be extracted because of this property. The results are compared to results of Bannink [5], and despite the different classification in the diagram from Miller and Wood, some agreements are found in the conical streamline distribution.

Chapter 6

DNW-SST

6.1 Introduction

With the successful application of stereo-PIV on delta wings in the research facility TST-27, an extension is made to the supersonic industrial facility of DNW-SST. PIV is being applied regularly in the large low speed facility LLF and a previous experiment is performed in DNW-SST, which showed the feasibility of PIV in this facility although improvements were possible in the area of optical access and flow seeding procedure [27].

In this experimental campaign three main objectives are pursued:
1. application of stereo-PIV for the characterization of the flow over the delta wings of the EUROSUP model.
2. Utilization of a kilo-hertz repetition rate system for high-data density.
3. 3D multi-planar analysis by on-line lateral sliding of the model.

The experimental test matrix can be found in appendix A.

6.2 Experimental setup

6.2.1 Flow facility

The supersonic facility DNW-SST in Amsterdam, The Netherlands, is a windtunnel of the blow-down type, similar to the TST-27 but larger. The air comes from a storage vessel containing $600m^2$ at a maximum pressure of about 40 bar and is dried to prevent condensation. The air is fed through the main valve and a pressure regulator valve in order to set the pressure in the settling chamber. A total of six mesh screens in the settling chamber reduce the turbulence and guarentee flow uniformity. The air is then accelerated through a laval nozzle into the test section. Downstream of the test section is a variable and a fixed diffuser and finally after passing a silencer the air flows into the exhaust building.

The test section has a rectangular cross section with a width of $1.2m$ and a maximum height of $1.2m$ (depending on the Mach number). The flow regime of this facility ranges from $M = 1.3$ to $M = 4.0$. The maximum stagnation pressure is 14.7 bar (depending on the Mach number). The stagnation temperature is equal to the ambient temperature. Heat generators

in the pressure vessel limit the temperature drop during a run to a few degrees Kelvin. More information can be found in the SST user guide [1].

6.2.2 Model

The EUROSUP model is stainless steel sting-mounted 1/80 scale model of the European supersonic commercial transport aircraft (ESCT), consisting of a cylindrical fuselage with a twisted, delta wing platform of variable sweep, see figure 6.1. The model parameters can be found in table 6.1. The shape of the model wing is modified such that the design geometry is recovered during wind tunnel operation. Additionally during one run a wedge has been attached to the model to perform a simple shock test in order to investigate the tracer particle response time.

6.2.3 Seeding system

A 120 Laskin nozzle device operating at approximately $3.5bar$ is used to produce a seeded flow containing DEHS particles. The seeded flow is dispersed in the settling chamber through a seeding rake (see figure 6.2) of approximately $60cm$ in width and $80cm$ in height and it is provided with 6 seeding ducts with a length of about $75cm$. The exit orifices are 2 mm in diameter. A bypass has been installed on the seeder to enlarge the mass flow into the settling chamber, while retaining the original amount of tracer particle production. The seeded streamtube expands through the converging-diverging section and has an area of approximately $12 \times 15cm^2$ in the test section. From a feasability study [27] an estimate of the particle relaxation time of $\tau = 0.5\ \mu m$ has been made corresponding to a particle diameter $d_p = 0.3\mu m$.

6.2.4 Particle Illumination

The seeding particles are illuminated by a Quantronix Darwin-Duo dual-head Nd:YLF high repetition laser with a wavelength of $527nm$. A repetition rate of $500Hz$ is used to maximize the pulse energy, which is estimated to be $30mJ/pulse$ at this specific repetition rate. The

Model Dimensions		
Model Scale	1:80	
Length	936.2 mm	
Span	525.0 mm	
Fuselage diameter	51.06 mm	
Balance centre with respect to fuselage	x	700 mm
	y	0.0 mm
	z	-1.95 mm
Reference Dimensions		
S_{ref}	137090 mm^2	
L_{ref} (=c)	344.1 mm	
Base area	2048 mm^2	

Table 6.1: Model parameters.

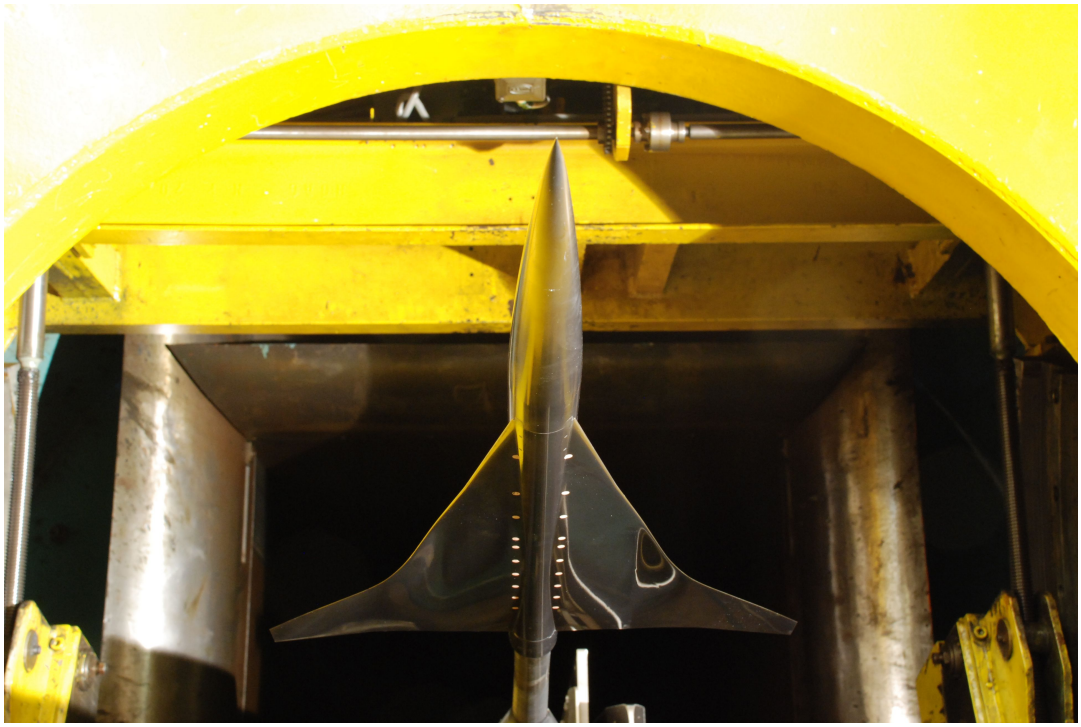

Figure 6.1: The EUROSUP model.

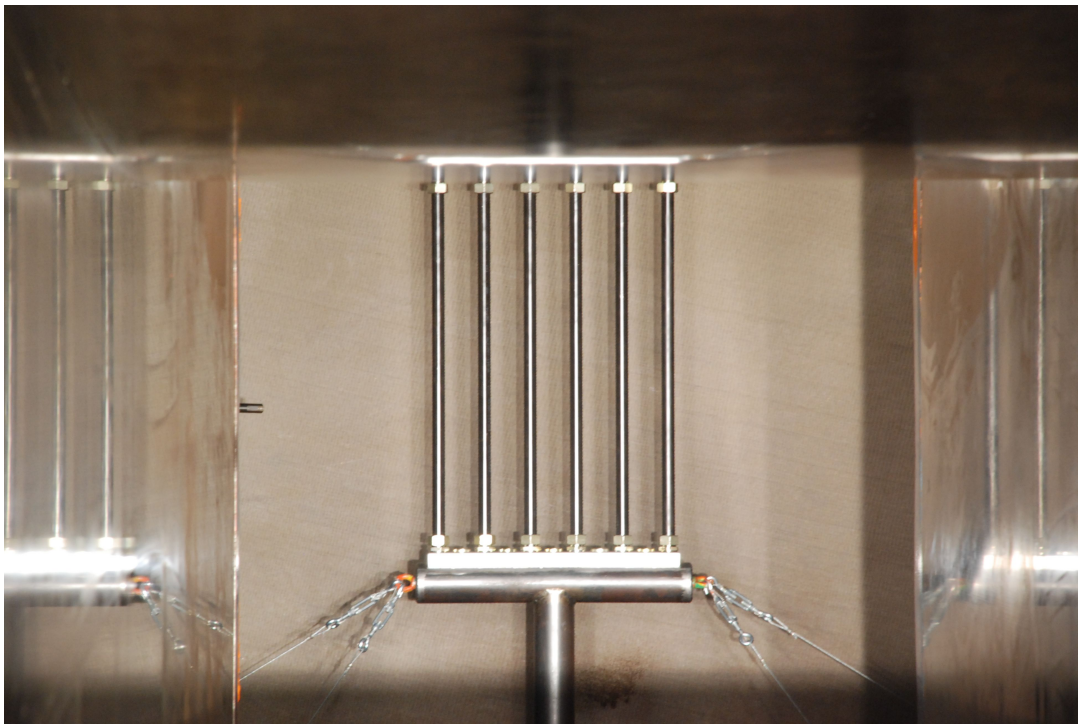

Figure 6.2: The seeding rake where the seeded air enter the settling chamber.

laser beam is deflected by a mirror after which it goes through the Schlieren window to an optical probe on the wind tunnel top wall, see figures 6.3 and 6.4. The probe is placed such that it is not directly exposed to the flow. It contains a mirror, a cylindrical and a spherical lens that form a light sheet of about $2.5mm$ in thickness at the measurement location. A LaVision High Speed Controller triggers the laser pulses and the cameras. A pulse separation time of 3 μs is used, corresponding to a particle image travel of 10 pixel between exposures.

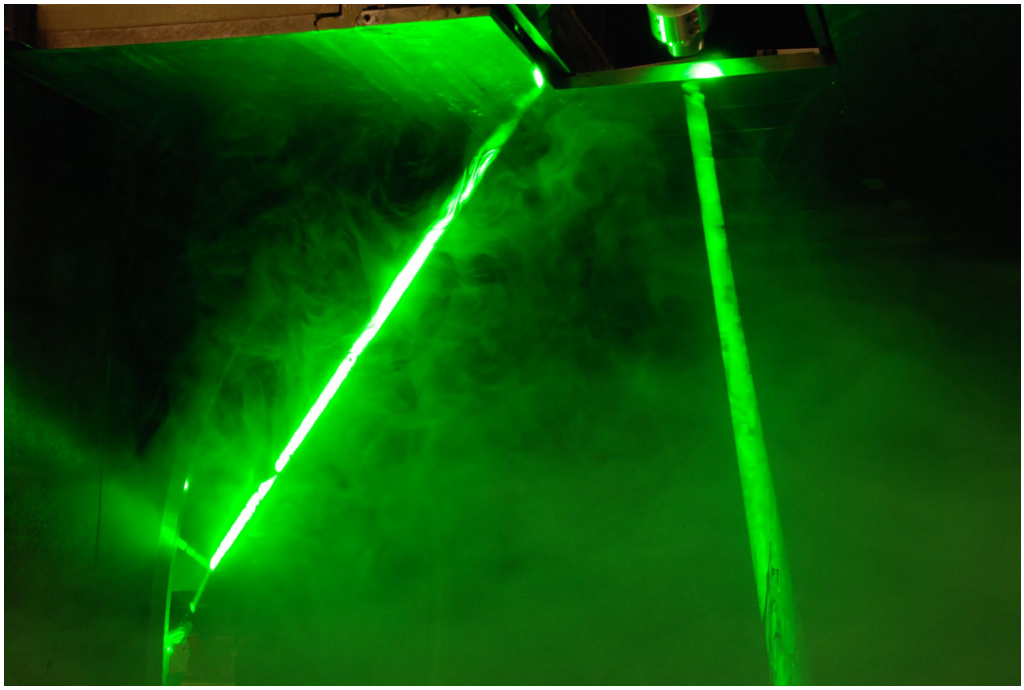

Figure 6.3: The path of the laser light from the cavity to the measurement field.

6.2.5 Image Recording

Two Photron CMOS cameras (1024×1024 pixels at $5,400Hz$, 12 bits) arranged in stereoscopic configuration are used to record the particle images. One camera is perpendicular to the field of view, while the other is placed at an angle of approximately 30 degrees with respect to the normal, see figure 6.5. Both cameras are equipped with a $105mm$ focal objective resulting in a field of view of $15 \times 15cm^2$. To keep the full field of view in focus a Scheimpflug adapter is used for the latter. Both cameras and the laser were mounted on X-beams which in turn were attached to the windtunnel to avoid misalignment of the cameras due to windtunnel vibrations, see figure 6.6. Ensembles of 1000 images are taken at each run in $2s$.

The optimum diffraction spot diameter corresponds to $f_\# = 16$. However, since the collection of scattered light decreases with an increasing $f_\#$, to ensure image contrast an $f_\# = 4.0$ is chosen, at the cost of peaklocking of the data.

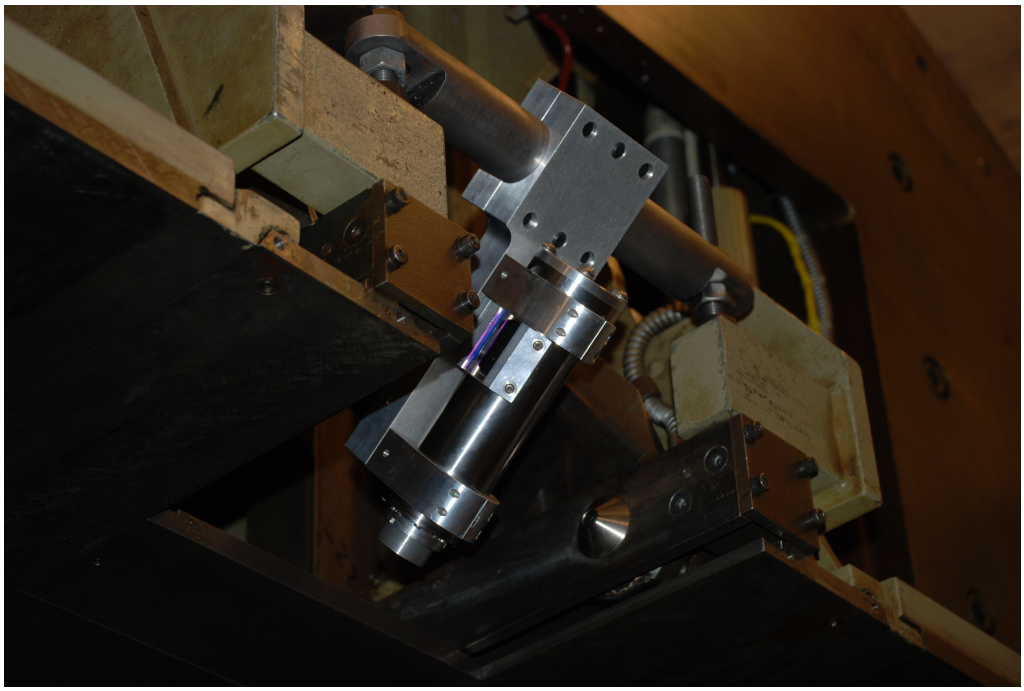

Figure 6.4: Detailed view of the optical probe that holds the lenses.

6.2.6 Model traversing system

To change the measurement location on the wing, the model is traversed, while the cameras and laser sheet remain unchanged, i.e. the cameras stay in focus, the magnification remains constant etc. Since the total acquisition time of the cameras is very short ($2s$), the most time consuming factor of each windtunnel run consists of tunnel start-up and stop. A stepper motor has been installed to slide the model laterally during windtunnel operation, dramatically increasing the data production per run. The limitation on the data acquisition would then become the RAM storage capability of the cameras. This approach causes a total reduction in required runs with a factor 3.

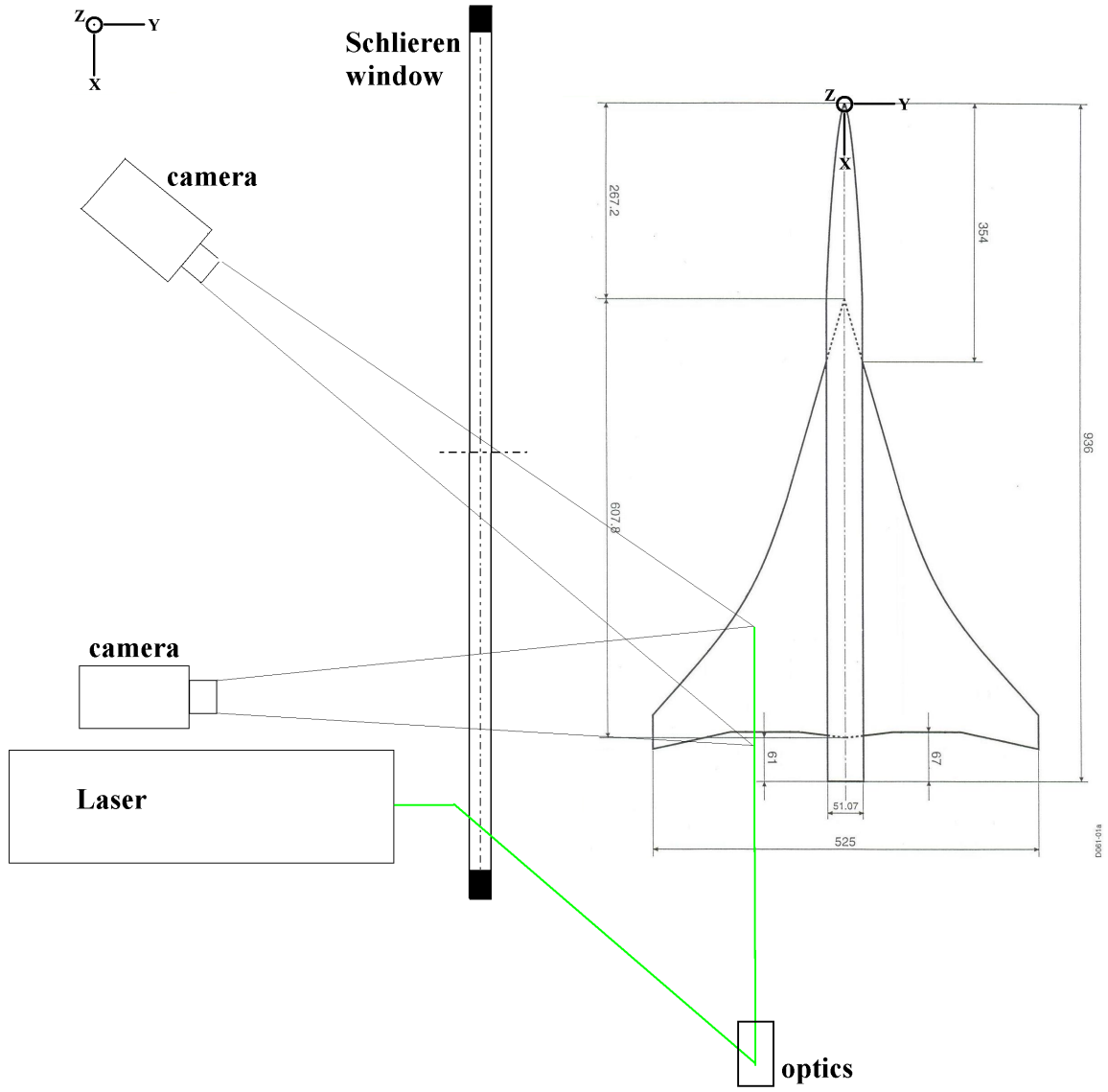

Figure 6.5: Measurement regions.

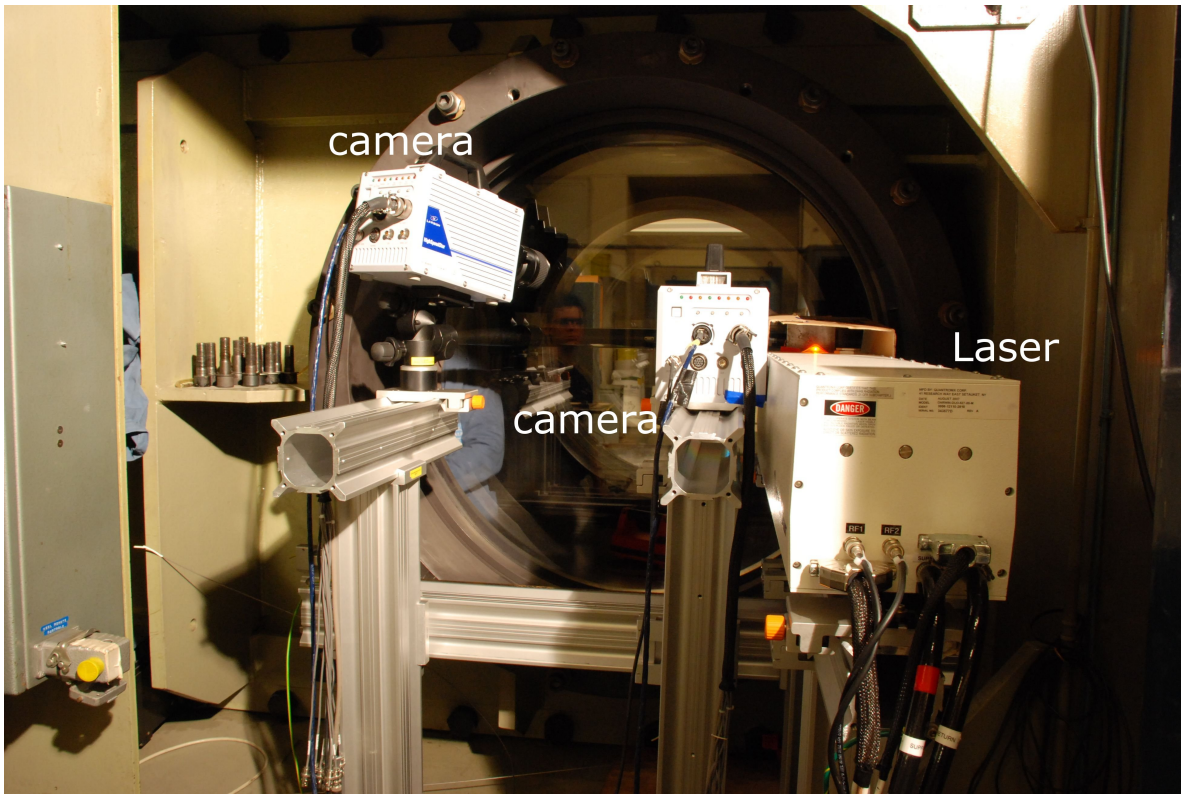

Figure 6.6: The setup of the laser and cameras.

6.3 Results

In total 7 planes with a plane pitch of $40mm$ have been measured at a angle of attack of 6°. Assuming steady flow, the individual measurement planes can be combined forming a 3-dimensional representation of the flow, although sampling in z-direction is poor.

6.3.1 Tracer particles

The feasability study showed that the amount of tracer particles would be a problem. In the design of the experiment improvements have been made by applying a by-pass line in the seeder in order to increase the amount of seeded mass flow while retaining an equal amount of generated particles. During the experiments it became evident that the amount of seeding should be improved and that large particles were present in the flowfield. The amount of seeding significantly improved after rotating the particle ejection direction of the seeding rack 90° from lateral into the up- and downstream direction, see figure 6.7. The size of the particles posed a real problem because of their large particle response time.

A method of removing large particles from the raw images has been used in order to enhance the data. Since the largest particles scatter most light, these particles appear the brightest on the images. By removing the most light-intense particles from the images, you also take out the large particles. Although this decreased the signal-to-noise ratio, the results are more reliable since the large particles that do not follow the flow are taken out.

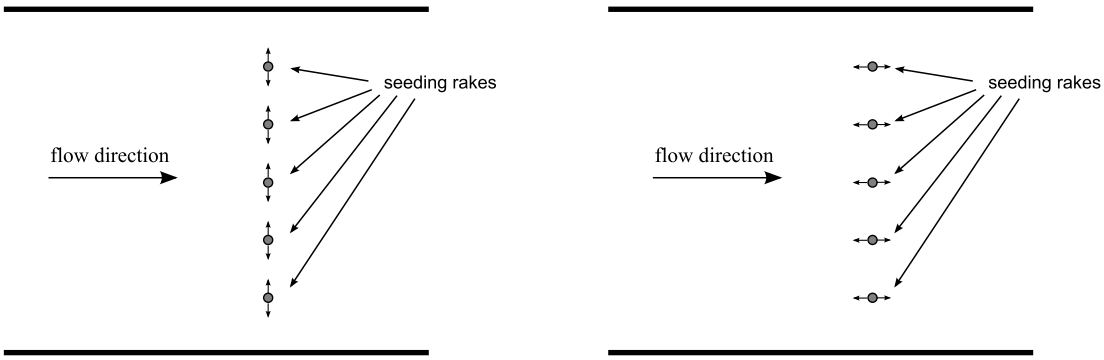

(a) perpendicular to the flow direction

(b) in up- and downstream direction

Figure 6.7: Difference in orientation of seeding rack orifices

To determine the particle response time, a wedge has been attached to the model. The shock generated from this wedge induces a velocity jump normal to the shock. From this velocity data, the particle response length and time can be determined [22]. Since the measurements have not been optimised for an investigation of tracer particle response, the accuracy of the test only allows for an order of magnitude estimation. The position where the velocity profile is taken is shown in figure 6.8 and the velocity profile is displayed in figure 6.9. A least-squares approach is used to determine the best exponential fit though this data and a relaxation length of approximately $19mm$ is determined, which corresponds to a relaxation time of 100 μs. This means that frequencies of the order of $1/10^{-4} = 10000Hz$ or higher are not measured accurately. With a mean flow velocity of $500m/s$ this corresponds to flow structures of $5cm$ in size. The largest structure present would be the primary vortex above the wing which has the same order of magnitude in frequency as the particle response. Typically an order of magnitude safety margin would be applicable to be able to say that the flow structure is reliably solved, so small scale structures are not followed by the particles and even the tracing of the primary vortex is questionable.

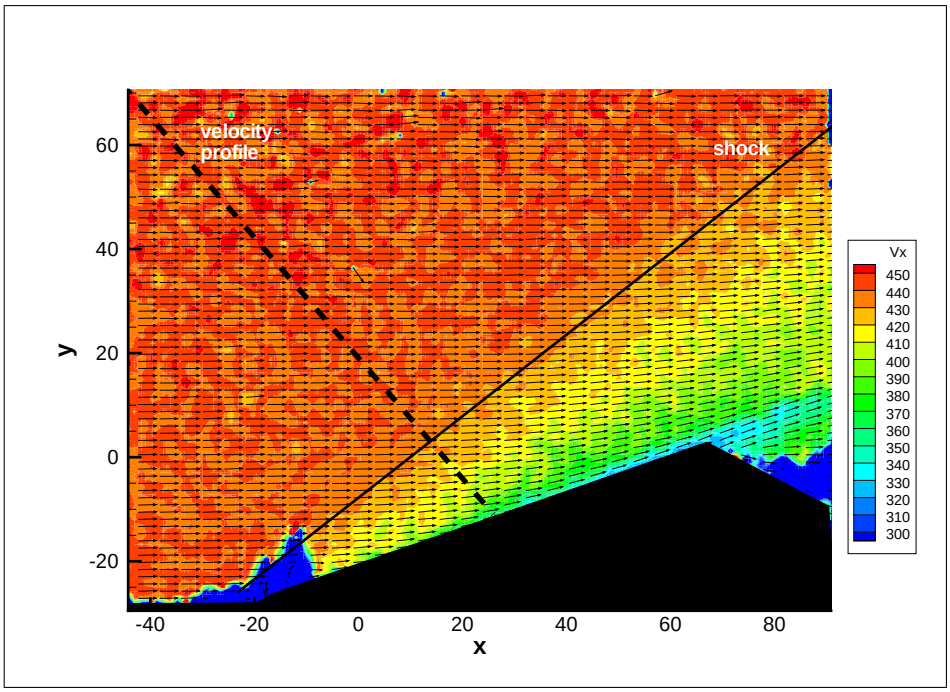

Figure 6.8: Location of the velocity profile

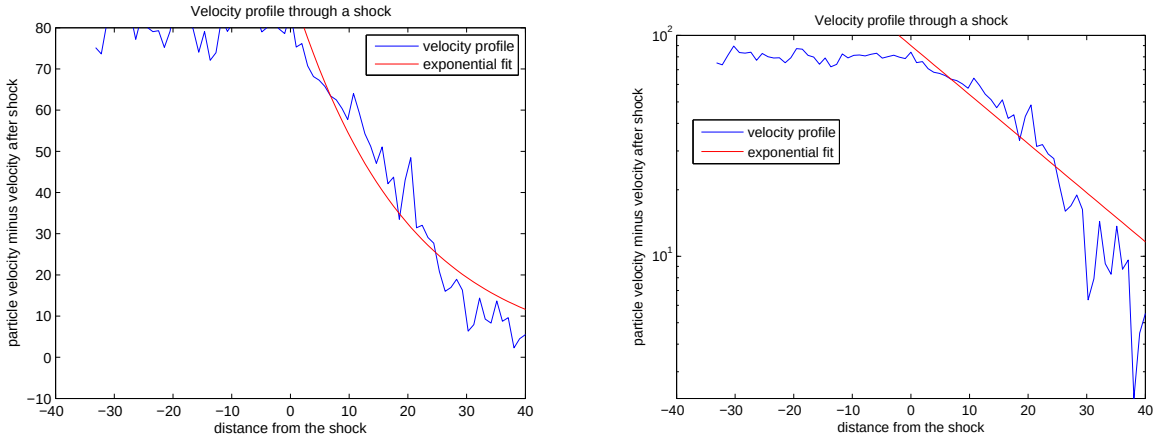

(a) Velocity profile on a normal scale.

(b) Velocity profile on a logarithmic scale.

Figure 6.9: Velocity profile through the shock with an exponential fit

6.3.2 Reflections

Another problem encountered were reflections of laser light from the fuselage. For the camera placed in side scatter the reflections were acceptable, but for the camera in forward scatter mode, these were more severe, significantly reducing the signal-to-noise ratio, see figure 6.10, especially when the light sheet was close to the fuselage. Covering the fuselage with Rhodamin B was not enough to prevent these reflections.

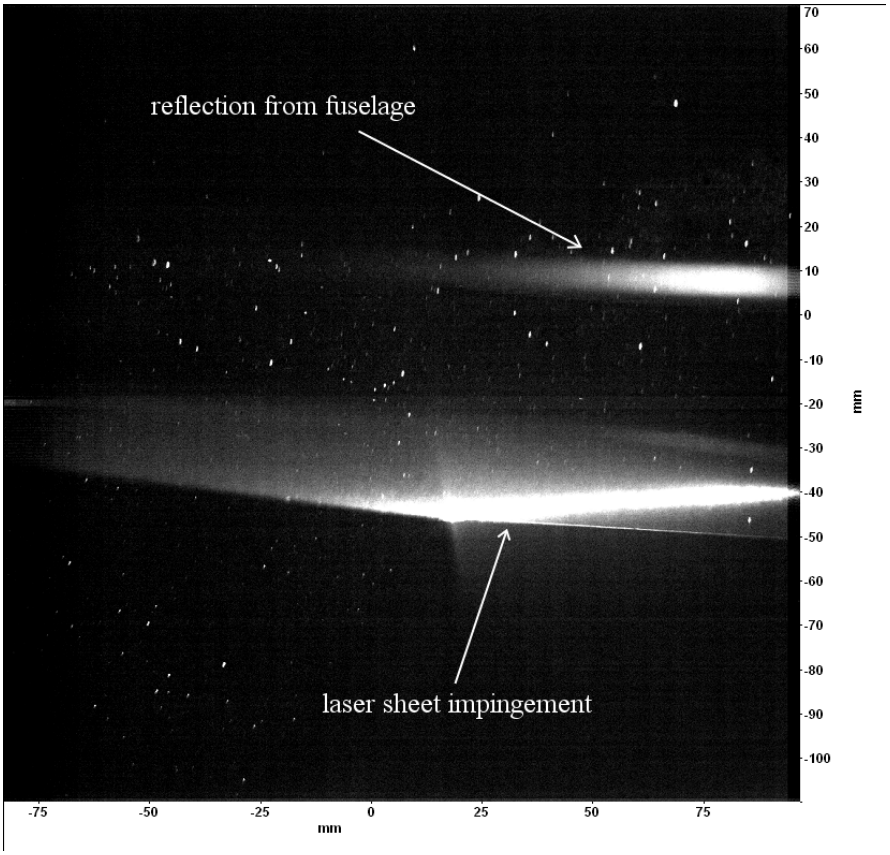

Figure 6.10: Reflection on the image of the camera in forward scatter.

6.3.3 Model sliding mechanism

A stepper motor was installed on the model sliding mechanism that automated the lateral movement of the model. Although it functioned correctly at wind-off conditions, during wind tunnel operation the mechanism failed because the stepper motor appeared to lack power. With a more powerful stepper motor the automated sliding mechanism will probably work, increasing data output dramatically.

6.3.4 Velocity data

Some results are displayed in figure 6.11. A general trend of a vortex can be detected by the upward motion of the particles just before the leading edge, and a downward motion further downstream above the wing. Also the inboard motion is detected. However, whether this

is the position of the vortex above the wing can be put in doubt due to the large particle relaxation time.

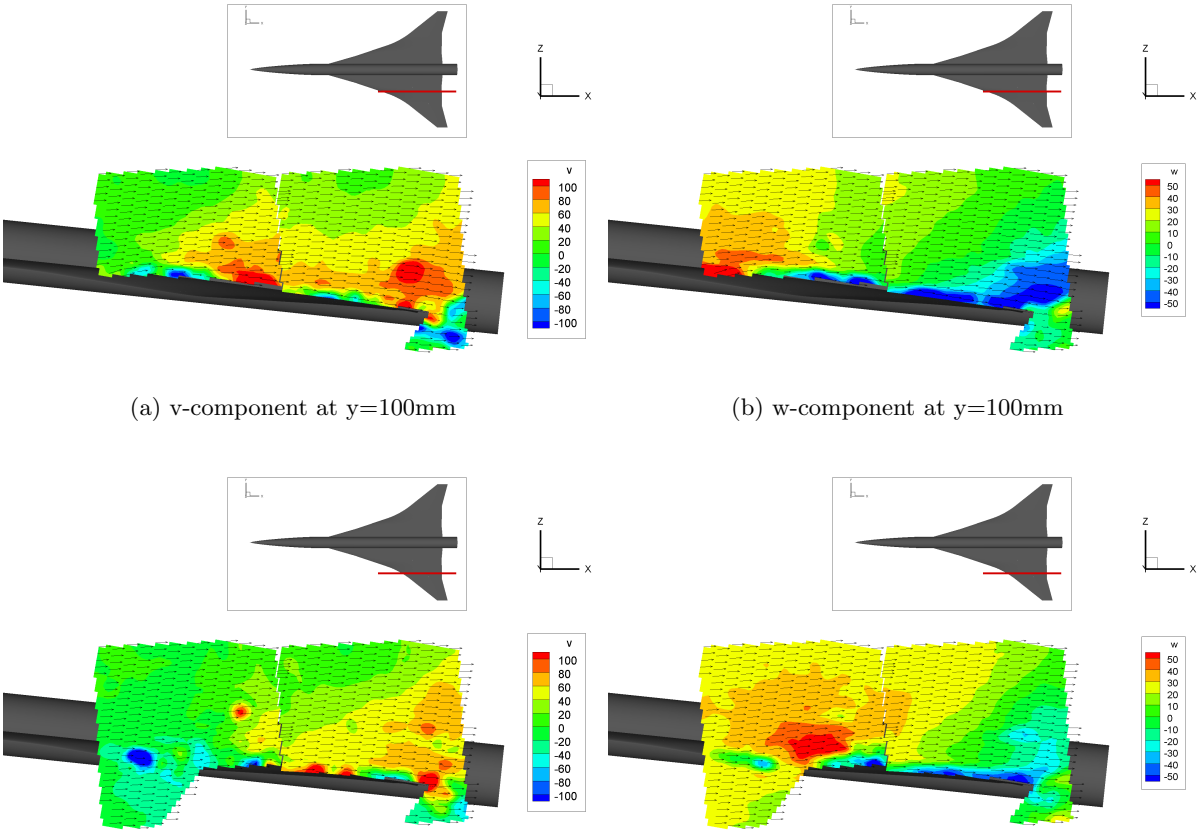

(a) v-component at y=100mm

(b) w-component at y=100mm

(c) v-component at y=140mm

(d) w-component at y=140mm

Figure 6.11: some velocity contours on the EUROSUP model

6.4 Conclusion

Stereoscopic PIV measurements have been performed in the industrial supersonic DNW-SST facility. Because of the large particle relaxation time the accuracy of the measurements is limited. It has been possible to create a laser sheet of approximately $2.5mm$, which was thin enough to perform PIV measurements. The laser beam was inserted through the Schlieren window without damaging the glass. The beam was deflected by a mirror to the optical device to transform the beam into a thin light sheet at the measurement section. It appeared to generate enough light to be able to collect scattered light from the particles at wind-off and wind-on conditions, while the laser was not yet at maximum power. Reflections are suppressed by using a black coating on the model and additionally covering them with black tape covered with Rhodamin B. Despite these measures reflections still influenced the calculated velocity data.

The generation of sufficiently small particles appeared to be problematic. The seeding particles at wind-on conditions were too large to follow the flow accurately. A lot of seeding generator conditions have been tested, but none of them gave adequate results. This has detrimental influence on the reliability of the results. A thorough investigation on the seeding generation is needed to solve this problem, especially because good seeding conditions have been achieved with this seeder in similar conditions with the feasability study in the same wind tunnel [27]. Furthermore the rotation of the seeding rake pipes by 90° resulted in a significant increase in seeding density. In conclusion when problems with the seeder are solved, reliable PIV measurements at supersonic conditions on real models in the DNW-SST facility are feasable.

The model traversing system functioned correctly except at wind-on conditions. A more powerful stepper motor would be capable of traversing the model during a run, increasing the data generation dramatically in combination with the high repetition system used in this campaign, thus decreasing the amount of required runs by a factor of about 3.

Chapter 7

Conclusions & recommendations

7.1 Supersonic delta wing flow

The supersonic flow around a delta wing has been investigated using several different complementary measurement methods. A standard side view Schlieren and shadowgraphy setup was made which was able to show the presence of the primary vortex on the delta wing leeward surface. However it was not able to capture the presence of a shock in the flowfield. This is due to the fact that it is a 2-dimensional technique, and the shocks present on the delta wing are almost perpendicular to the viewing direction. Probably a surface reflective Schlieren setup would have been able to visualise the shocks.

Oil flow visualisation showed the presence of primary and secondary vortices on the leading edge with great precision. Only this technique and shadowgraphy were able to capture the secondary vortex for $M_\infty = 1.7$. However oil flow visualisation was completely unable to find shock waves, since they are not attached to the surface.

Stereoscopic PIV has been the only quantitative method used in this investigation. Because of the high accelerations in the flow field, the tracer particles slip with respect to the flow due to their inertia, resulting in a slip velocity and a deviation from the fluid path.

A shock test is performed to measure the response of the tracer particles to a step input, resulting in a tracer particle relaxation time of 2.1 μs. With this value, the path deviation of the particle and the slip velocity in a circular vortex are calculated. The path deviation, which is linear proportional to the tangential velocity, manifests itself by an empty vortex core, because all particles are ejected preventing reliable measurements in this area. The slip velocity is quadratic proportional to the tangential velocity, introducing errors close to the vortex core.

The freestream velocity is measured correctly and the tunnel produces repeatable flow conditions, allowing a combination of the individual measurement planes into a full 3-dimensional flow field. These results produce a clear visualisation of the top of the primary vortex. Also two different shock waves are found in the flow field. One of them is in front of the leading edge, which is a detached shock wave due to the large deflection of the flow on the windward surface. The other is an inboard shock wave which was expected because the measurements are performed in region 3 of the Miller and Wood classification. A schematic overview of a cross-section of the flow field is given in figure 7.1.

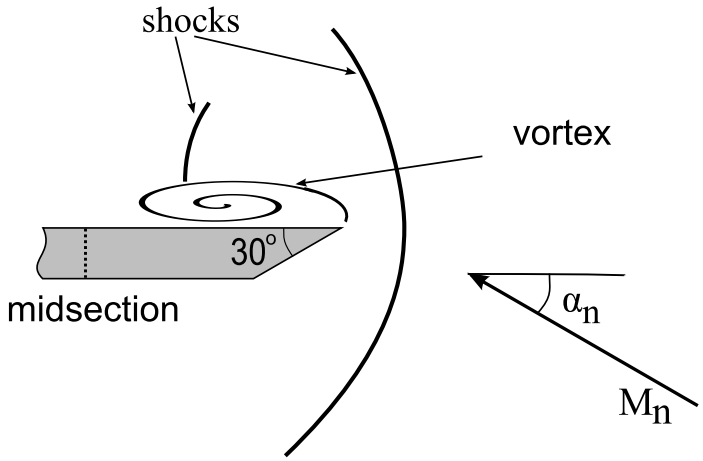

Figure 7.1: Schematic overview of the flow features in a cross-section of the flow field.

The flow field is found to be conical, making it possible to transform from Cartesian coordinates into conical coordinates. Because the flow is depending only on ϕ and θ, this allowed averaging over the different r-stations. In principle from one well-chosen measurement plane, the complete flowfield could be extracted because of this property. The results are compared to results of Bannink [5], and despite the different classification in the diagram from Miller and Wood, some agreements are found in the conical streamline distribution.

7.2 Extension to industrial facility DNW-SST

Stereoscopic PIV measurements have been performed in the industrial supersonic DNW-SST facility. Because of the large particle relaxation time the accuracy of the measurements is limited. It has been possible to create a laser sheet of approximately $2.5mm$, which was thin enough to perform PIV measurements. The laser beam was inserted through the Schlieren window without damaging the glass. The beam was deflected by a mirror to the optical device to transform the beam into a thin light sheet at the measurement section. It appeared to generate enough light to be able to collect scattered light from the particles at wind-off and wind-on conditions, while the laser was not yet at maximum power. Reflections are suppressed by using a black coating on the model and additionally covering them with black tape covered with Rhodamin B. Despite these measures reflections still influenced the calculated velocity data.

The generation of sufficiently small particles appeared to be problematic. The seeding particles at wind-on conditions were too large to follow the flow accurately. A lot of seeding generator conditions have been tested, but none of them gave adequate results. This has detrimental influence on the reliability of the results. A thorough investigation on the seeding generation is needed to solve this problem, especially because good seeding conditions have been achieved with this seeder in similar conditions with the feasability study in the same wind tunnel [27]. Furthermore the rotation of the seeding rake pipes by 90° resulted in a significant increase in seeding density. In conclusion when problems with the seeder are

solved, reliable PIV measurements at supersonic conditions on real models in the DNW-SST facility are feasable.

The model traversing system functioned correctly except at wind-on conditions. A more powerful stepper motor would be capable of traversing the model during a run, increasing the data generation dramatically in combination with the high repetition system used in this campaign, thus decreasing the amount of required runs by a factor of about 3.

7.3 Recommendations

In order to be able to perform more reliable measurements around delta wings using PIV, further development on the tracer particles is necessary. High accelerations are present in the flow field due to vortices and shocks, and tracer particles are not able to follow the flow accurately. This resulted in an empty vortex preventing reliable measurements in this region and a slip velocity that introduces an error in the measurement. To overcome these problems the tracer particles should be improved by decreasing the particle relaxation time. This is not easy to accomplish because this generally means smaller particles which also scatter less light. Light intensity can be increased, but reflections will become more severe. Another solution to measure more accurately on a delta wing model is by scaling up. A larger geometry with the same velocities results in lower accelerations, leading to a smaller slip velocity and less particle drift. However, measurements in the DNW-SST facility showed that this is not easy to perform.

A thorough study into the seeding generator of DNW is necessary to be able to perform PIV measurements in the SST-facility. The measurements showed that the particles are too large to follow the flow, but the reason why the particles are so large remained unclear.

Bibliography

[1] *SST user guide.*

[2] *User manual aerosol generator PivPart45 series*, 2007.

[3] *User Manual Aerosol Generator PivPart45 series*, 2007.

[4] John D. Anderson. *Modern compressible flow.* McGraw-Hill, 3 edition, 2003.

[5] W.J. Bannink and C. Nebbeling. Investigation of the expansion side of a delta wing at supersonic speed. *AIAA journal*, 11(8):1151–1156, 1973.

[6] Sharon R. Donohoe. *Vortex flow and vortex breakdown above a delta wing in high subsonic flow: an experimental investigation.* PhD thesis, Delft University of Technology, 1996.

[7] M. Elsayed, F. Scarano, and N.G. Verhaagen. Particle image velocimetry study of the flow over a slender delta wing. In *Proceedings of the 25th AIAA Applied Aerodynamics Conference*, Miami, Florida, 2007.

[8] G.E. Elsinga, F. Scarano, B. Wieneke, and B.W. van Oudheusden. Tomographic particle image velocimetry. *Experiments in Fluids*, 41:933947, 2006.

[9] R. Fei, R. Lindken, W. Merzkirch, and F. Peters. A method of reconstruction of three-dimensional velocity in an angular stereoscopic piv system. In *proceedings of the EUROMECH 411 colloquium*, Rouen, France, 2000.

[10] N.C. Lambourne and D.W Bryer. The bursting of leading-edge vortices - some observations and discussion of the phenomenon. Technical Report 3282, Aeronautics Research Council, London, 1961.

[11] N. Lang. Investigation of the supersonic flow field around a delta wing using particle-image-velocimetry. In *proceedings of the 10th International Symposium on Applications of Laser Techniques to Fluid Mechanics*, Lisbon, Portugal, 2000.

[12] I. McGregor. The vapour-screen method of flow visualisation. *Journal of Fluid Mechanics*, 11:481–511, 1961.

[13] S.N. McMillin, J.L. Thomas, and E.M.Murman. Euler and navier-stokes leeside flows over supersonic delta wings. *journal of aircraft*, 26(5):452–458, 1989.

[14] A. Melling. Seeding gas flows for laser anemometry. In *Conference on Advanced Instrumentation for Aero Engine Components*, 1986.

[15] A. Melling. Tracer particles and seeding for particle image velocimetry. *Meas. Sci. Technol.*, 8:1406–1426, 1997.

[16] David S. Miller and Richard M. Wood. Leeside flows over delta wings at supersonic speeds. *Journal of Aircraft*, 21(9):680–686, 1984.

[17] van Muijden, J. Improvement and verification of low-speed aerodynamic characteristics of a supersonic civil transport aircraft. Technical Report 514, NLR, 2005.

[18] A.J. Prasad and K. Jensen. Scheimpflug stereocamera for particle image velocimetry in liquid flows. *Applied optics*, 34(30):7092–7099, 1995.

[19] A.K. Prasad. Stereoscopic particle image velocimetry. *Experiments in Fluids*, 29:103–116, 2000.

[20] M. Raffel, C. Willert, S. Wereley, and J. Kompenhans. *Particle Image Velocimetry: a practical guide*. Springer, second edition, 2007.

[21] F. Scarano, L. David, M. Bsibsi, and D.Calluaud. S-piv comparative assessment: image dewarping+misalignment correction and pinhole+geometric back projection. *Experiments in Fluids*, 2005.

[22] F.F.J. Schrijer and F. Scarano. Particle slip compensation in steady compressible flows. In *7th International Symposium on Particle Image Velocimetry*, Rome, Italy, 2007.

[23] F.F.J. Schrijer, F. Scarano, and B.W. van Oudheusden. Application of piv in a mach 7 double-ramp flow. *Experiments in fluids*, 41:353363, 2006.

[24] A. Schröder, J. Agocs, H. Frahnert, D. Otter, H. Mattner, J. Kompenhans, and R. Konrath. Application of stereo piv to the vfe-2 65° delta wing configuration at sub- and transonic speeds. In *Proceedings of the 24th aerodynamics conference*, San Francisco, California, June 2006.

[25] L.C. Squire. Flow regimes over delta wings at supersonic and hypersonic speeds. *Aeronautical Quarterly*, 25:1–14, 1964.

[26] A. Stanbrook and L.C. Squire. Possible types of flow at swept leading edges. *Aeronautical Quarterly*, 15:72–82, 1964.

[27] R.K. van der Draai, R.van Schinkel, A. Telesca, F. Scarano, G.E.Elsinga, and G.J. Feenstra. Application of piv in (local) supersonic flows in dnw wind tunnels. In *41st AIAA/ASME/SAE/ASEE Joint Propulsion Conference and Exhibit*, number AIAA-2005-4082, Tucson Arizona, 10-13 July 2005. AIAA.

[28] N.G. Verhaagen and C.E. Jobe. Wind tunnel study on a 65-deg delta wing at sideslip. *journal of aircraft*, 40(2):290–296, 2003.

[29] C. Willert. Stereoscopic digital particle image velocimetry for application in wind tunnel flows. *Meas. Sci. Technol.*, 8:742–753, 1997.

Appendix A

test matrix DNW

Run	Date	Time	M_∞	p0 [kPa]	α [°]	X [mm]	Y [mm]	Z [mm]	Seeding pressure		Comment
									primary line	secondary line	
1	25/3/08	15:20	2.0	220	9.5	800	0	80	500	510	Incl. Schlieren; excl. PIV measurement There is seeding produced but not fully understood. Three seeding pot valves open.
2	25/3/08	16:10	2.0	220	9.5	800	0	80	500	510	No seeding visible in PIV images. At these pressures you expect sonic conditions at the seeding rack but no sonic conditions at the Laskin Nozzles. Three seeding pot valves open.
3	25/3/08	16.55	2.0	226	9.5	800	-30	80	500	-	By-pass removed. We produce seeds but intermittently. Model and tunnel wall are covered with liquid (grease). We doubt whether we have sonic conditions at the Laskin nozzles. Three seeding pot valves open.
4	26/3/08	13.50	2.0	226	9.5	800	-30	80	500	?	By-pass connected again. Two valves in primary line closed (valves 3). Additional manometer mounted at outgoing line of seeder pot. Valves appeared not to be opened. Run discarded. Three seeding pot valves open.
5	26/3/08	14.15	2.0	226	9.5	800	-30	80	500	300	On the additional manometer 300. Number of seeds seem to be increased. Three seeding pot valves open.
6	26/3/08	15.45	2.0	226	9.5	800	-30	80	700	400	On the additional manometer 400. Number of seeds seem to be somewhat better than run 5. Three seeding pot valves open.
7	26/3/08	16.00	2.0	226	9.5	800	-30	80	700	300	On the additional manometer 300. Number of seeds seem to be somewhat better than run 6. PIV system not started correctly. Three seeding pot valves open.
8	27/3/08	11.30	2.0	226	9.5	800	-30	80	700 700	300 400	One seeding pot valve (out of 3) open. Two seeding valves (out of 3) open; no PIV measurement.
9	27/3/08	12.30	2.0	226	9.5	800	-30	80	700	300	One seeding pot valve (out of 3) open; reasonable seeding
10	27/3/08	13.45	2.0	226	2	800	-30	80	700	300	One seeding valve (out of 3) open; Model angle 2 deg
-	27/3/08	15.00	2.0	226	2	800	-30	80	-	-	Blowing the channel clean for turning the seeder rack pipes 90 deg; No PIV measurement
11	27/3/08	16.30	2.0	226	2	800	-30	80	700	300	Seeding rack pipes turned 90 deg; One seeding pot valve (out of 3) open
-	27/3/08	16.45	2.0	226	0	800	-30	80	-	-	Just cleaning the channel.

Run	Date	Time	M_∞	p_0 [kPa]	α [°]	X [mm]	Y [mm]	Z [mm]	Seeding pressure		Comment
									primary line	secondary line	
12	28/3/08	12.15	2.0	226	9.5	800	-60	0	700	300	Seeding rack pipes turned 90 deg. Model on centerline. Y-traverse over 40 mm. Afterwards it appears that y-traverse did not work. One seeding pot valve (out of 3) open
-	27/3/08	16.45	2.0	226	0	800	-30	80	-	-	Just cleaning the channel.
13	28/3/08	14.10	2.0	226	9.5	800	-100	0	600	-	Seeding rack pipes turned 90 deg. Model on centerline. Y-traverse over 40 mm. Afterwards it appears that y-traverse did not work. No by-pass mounted. In outside line of seeder pot 300 kPa. Droplets in seeding far too big.
14	28/3/08	14.45	2.0	226	9.5	800	-100	0	800	-	Seeding rack pipes turned 90 deg. Model on centerline. No by-pass mounted. In outside line of seeder pot 350 kPa. Droplets in seeding far too big. One seeding pot valve (out of 3) open
15	28/3/08	15.30	2.0	226	9.5	800	-100	0	700	350	Seeding rack pipes turned 90 deg. Model on centerline. By-pass mounted again. One seeding pot valve (out of 3) open. Still big droplets but it is much better than without bypass.
-	27/3/08	15.40	2.0	226	0	800	-30	80	-	-	Just cleaning the channel. Model not fixed properly to the sting anymore.
16	28/3/08	16.45	2.0	226	9.5	800	-100	0	450	300	Seeding rack pipes turned 90 deg. Model on centerline. One seeding pot valve (out of 3) open. Seeding results comparable to setting 700/300. Anyhow, we decide to start production runs with 700/300. Big droplets might be taken out with a cyclone. In NOP we use a cyclone but is not available now for this test.
17	31/3/08	9.20	2.0	226	6	800	-60	0	700	300	One seeding pot valve (out of 3) open. Tape on fuselage damaged. Big droplets in seeding remain.
18	31/3/08	10.10	2.0	226	6	800	-100	0	700	300	One seeding pot valve (out of 3) open.
19	31/3/08	10.30	2.0	226	6	800	-140	0	700	300	One seeding pot valve (out of 3) open. After the run, cleaning windows. Model appears to be moving with respect to the sting. Fixation with loctite.
20	31/3/08	11.40	2.0	226	6	800	-180	0	700	300	One seeding pot valve (out of 3) open. Model fixation checked and improved again.
21	31/3/08	12.15	2.0	226	6	650	-60	0	700	300	One seeding pot valve (out of 3) open.
22	31/3/08	12.25	2.0	226	6	650	-100	0	700	300	One seeding pot valve (out of 3) open.
23	31/3/08	13.50	2.0	226	6	650	-140	0	700	300	One seeding pot valve (out of 3) open.
24	31/3/08	18.30	2.0	270	0	500	0	0	700	300	Dedicated 20 deg wedge on top of the model; One seeding pot valve (out of 3) open. Wedge is not two dimensional!